ABSTRACT

Title of dissertation: ROBUST MULTI-OBJECTIVE OPTIMIZATION
OF HYPERSONIC VEHICLES UNDER
ASYMMETRIC ROUGHNESS-INDUCED
BOUNDARY-LAYER TRANSITION

Kevin Michael Ryan,
Doctor of Philosophy, 2014

Dissertation directed by: Professor Mark J. Lewis
Department of Aerospace Engineering

The effects of aerodynamic asymmetries on hypersonic vehicle controllability
and performance were investigated for a wide range of geometries. Asymmetric
conditions were introduced by an isolated surface roughness that forces boundary-
layer transition resulting in a turbulence wedge downstream of the disturbance. The
disturbance simulates the effects of physical deformations that may exist on a vehicle
surface or leading edge, such as protruding edges of thermal protection system tiles
or non-uniform surface roughness.

Both multi-objective and robust multi-objective optimization studies were per-
formed. Traditional multi-objective optimization methods were used to identify
vehicle designs that are best suited to withstand spanwise asymmetric boundary-
layer transition while retaining its performance and payload requirements. Trade-
offs between vehicle controllability and performance were analyzed. A novel multi-
objective based robust optimization method to solve single-objective optimization

problems with environmental parameter uncertainty was proposed and tested. Unlike commonly used robust optimization methods, the multi-objective method formulates an optimization problem such that post-optimality data handling techniques can identify multiple robust designs from a single solution set. This allows for comparisons to be made between different types of robust designs, thus providing more information about the design space. Comparisons were made between the robust multi-objective optimization formulation and conventional robust regularization- and aggregation-based methods. The results, performance, and philosophies of each method are discussed.

Design trends were identified for classifying the optimum and robust optimum designs of hypersonic vehicle shapes under boundary-layer transition uncertainties. Traditional multi-objective optimization results show that two types of vehicle shapes bound the set of Pareto-optimal solutions: wedge-like and cone-like. The L^2-norm optimum design, representing a compromise between the competing shapes, was a hybrid wedge-cone shape. The robust optimization results show that a flat wedge-like vehicle design is best for a worst-case scenario, while a pyramidal shaped vehicle design minimizes the expected detrimental effects on vehicle controllability. The analyses prove that the novel robust optimization method can provide a range of robust optimum results, while also capturing trade-offs within the design space, providing capabilities not available in state-of-the-art robust optimization methods.

ROBUST MULTI-OBJECTIVE OPTIMIZATION OF HYPERSONIC VEHICLES UNDER ASYMMETRIC ROUGHNESS-INDUCED BOUNDARY-LAYER TRANSITION

by

Kevin Michael Ryan

Dissertation submitted to the Faculty of the Graduate School of the
University of Maryland, College Park in partial fulfillment
of the requirements for the degree of
Doctor of Philosophy
2014

Advisory Committee:
Professor Mark J. Lewis, Co-Chairman/Advisor
Associate Professor Kenneth H. Yu, Co-Chairman/Advisor
Associate Professor Christopher P. Cadou
Professor Roberto Celi
Professor Ashwani K. Gupta

Dedication

To my girlfriend, Suzanne. Thank you for all your love and support.

Acknowledgments

I would like to thank my advisors Dr. Mark Lewis and Dr. Kenneth Yu for giving me the opportunity to conduct this research. Dr. Lewis, your knowledge and passion for the field of aerospace has inspired me throughout the completion of this dissertation and continues to do so. Dr. Yu, your support, patience, and advice enabled me to push forward through meetings, conferences, and on to the completion of my Ph.D. I would also like to thank my committee members Dr. Cadou, Dr. Celi, and Dr. Gupta whose insight and help guided me through my research. Their time and effort is much appreciated.

I would like to acknowledge the Air Force Office of Scientific Research funding that supported this work through the UMD/AEDC Hypersonic Workforce Revitalization Program. Their excitement and encouraging words at our technical reviews would always *revitalize* my motivation towards my research.

I would also like to thank my family for their constant support through my nine year academic adventure at the University of Maryland. Finally, I would like to thank my fellow co-workers in the Hypersonics Research Group and Advanced Propulsion Research Lab whose help and support I could not have done without. A special thanks goes out to Neal Smith, Vijay Ramasubramanian, and Jeremy Knittel for their insightful discussions about my work, help with editing my papers, and their intellectual interrogations to help me prepare for my Comprehensive Exam.

Table of Contents

List of Tables

List of Figures

List of Symbols and Abbreviations

A	planform power law scaling parameter
a	uncertainty neighborhood lower bound
B	base upper surface power law scaling parameter
b	uncertainty neighborhood upper bound
C	base lower surface power law scaling parameter
C_M	moment coefficient
Ch	Chapman-Rubesin parameter
$Drag$	total vehicle drag
d	upper and lower surface separation distance
dA	panel area
E	conditional expected value
F	robust counterpart objective function
f	(original) objective function
g	constraint function
g_w	wall-to-inviscid stagnation temperature ratio
H	stagnation enthalpy parameter (transformed plane)
h	all generations from 1 to t
J	number of constraint functions
K	penalty factor
L	vehicle length
$Lift$	total vehicle lift
M	Mach number, or number of objective functions
$\vec{M}$	moment vector
M_x	moment about the x-axis
M_y	moment about the y-axis
M_z	moment about the z-axis
m	base & lower surface power law exponent
N	number of panels in vehicle mesh
$\mathcal{N}$	normal distribution
n	planform surface & base surface power law exponent, or number of samples
$\hat{n}$	outward unit normal
P	pressure
$\mathbb{P}$	bounded parameter uncertainty set
Pr	probability
p	environmental parameter
$\breve{p}$	random parameter value
$\tilde{p}$	discrete set of p values
Q	number of objective functions
q	heat flux
R	gas constant
Re	Reynolds number
$\vec{r}$	position vector from CG to panel

r_y	distance from CG to panel in y direction
r_z	distance from CG to panel in z direction
S_p	vehicle planform area
S_w	vehicle wetted area
T	temperature
t	generation index
U	velocity magnitude
$\mathcal{U}$	uniform distribution
V	vehicle internal volume
v	number of design variables in design vector
w	vehicle width, or post-optimality weights
$\mathbb{X}$	bounded design variable set
x	body fixed longitudinal dimension, or design variable
$\bar{x}$	true Pareto-optimal design set
$\hat{x}$	approximated Pareto-optimal design set
$\vec{x}$	design variable vector
y	body fixed lateral dimension
z	body fixed vertical dimension
z^*	ideal point
β	oblique shock inclination angle
$\bar{\beta}$	pressure gradient parameter
Δ	small perturbation
ΔPM	MOGA Pareto metric function
δ	leading edge inclination angle, or environmental parameter perturbation
ϵ	uncertainty neighborhood
η	volumetric efficiency
θ	vehicle wedge angle
μ	dynamic viscosity
ρ	density
σ	standard deviation
τ	shear stress
ϕ	turbulence wedge half-angle, or probability density function
ψ	boundary-layer stream function (transformed plane)
$\langle \ \rangle_h$	arithmetic mean over generations 1 through t

Subscripts

I	robust regularization formulation
II	explicit averaging formulation
III	perturbation formulation
IV	robust MOGA formulation
0	stagnation value
ab	uncertainty neighborhood index
bad	bad point in objective space
$base$	vehicle base value

CG	about the center of gravity
cc	concave
con	after applying constraints
cv	convex
e	boundary-layer edge
ev	minimized expected value
$good$	good point in objective space
i	panel index, or averaging index
$i.e.$	illustrated example
j	constraint function index
l	lower surface
lam	laminar
lb	lower bound
$local$	at a given spanwise location
m	MOGA objective function index
max	maximum allowed for attached shock
p	planform
$press$	due to pressure
q	MOGA objective function index
$scaled$	after scaling
$span$	at a given value of p
t	at generation t
tot	total
$turb$	turbulent
u	upper surface
ub	upper bound
$visc$	due to viscosity
w	wall
wcs	minimized worst-case scenario
$with$	with a turbulence wedge present
$without$	without a turbulence wedge present
x	based on x distance, or x component
y	y component
z	z component
∞	freestream conditions

Superscripts

$\dagger$	average boundary-layer conditions
$'$	derivative in the transformed plane
$*$	global optimum

Acronyms

ABLT	asymmetric boundary-layer transition
AEDC	Arnold Engineering Development Complex
CFD	computational fluid dynamics

CG	center of gravity
DNS	direct numerical simulation
DOE	design of experiments
GADS	genetic algorithm and direct search
GNC	guidance, navigation, and control
HTV-2	Hypersonic Technology Vehicle-2
L/D	lift-to-drag ratio
MATLAB	Matrix Laboratory
MAXWARP	Maryland Axisymmetric Waverider Program
MOGA	multi-objective genetic algorithm
MOOP	multi-objective optimization problem
NASA	National Aeronautics and Space Administration
NSGA-II	Non-Dominated Sorting Algorithm-II
PDF	probability density function
PLIF	planar laser-induced fluorescence
SAEA	Surrogate-Assisted Evolutionary Algorithm
STABL	Stability and Transition Analysis for hypersonic Boundary-Layers
STS	Space Transportation System
TPS	thermal protection system
UMD	University of Maryland

Chapter 1:   Introduction

1.1   Motivation

Physical deformations, surface imperfections, or surface roughness on a hyper-sonic vehicle can promote early localized boundary-layer transition. If transition occurs asymmetrically, leading to drag asymmetry, it is essential that these effects be small enough to be compensated by the control system of the vehicle [1]. If the effects are too great, the asymmetries can perturb the vehicle to a state which is uncontrollable, leading to vehicle loss.

After the space shuttle *Columbia* accident, as a part of the Return to Flight effort, a focus was set on predicting hypersonic boundary-layer transition onset from damage (e.g., tile impact, gap fillers) [2]. A lack of quality flight data and complete understanding of the phenomena prompted a spacewalk to remove protruding gap filler before the reentry of STS-114. Post STS-114, many space shuttle flight experiments have been performed to investigate the impact of asymmetric boundary-layers due to roughness-induced transition. During the flight experiments, it was found that the shuttle's flight control system had to respond to a roll/yaw moment pro-duced by the experimentally induced asymmetric boundary-layer. Numerous firings of control jets and deflections of control surfaces were necessary to return the shuttle

to the nominal attitude [2].

The importance of vehicle surface conditions and their effects on vehicle controllability has also been identified for hypersonic cruise vehicles, as exemplified by the HTV-2 (Hypersonic Technology Vehicle-2) flight tests. The second flight test of HTV-2 ended in early vehicle termination. An independent review board concluded that the most probable cause of the HTV-2 premature flight termination was an unexpected aeroshell degradation, creating "multiple upsets of increasing severity" [3]. History has shown that it is important to include this phenomena in the models and methods used during the design process of hypersonic vehicles and projectiles.

The design process begins by listing all the mission requirements and constraints that are needed to be satisfied by the aerospace vehicle. The design space is typically wide open, leaving the designers with the task of performing a preliminary analysis in hopes to narrow the scope and provide a rough estimate of the vehicle shape and performance characteristics. This is often accomplished by the use of optimization methods. Traditional optimization methods tend to locate isolated, specific design points with high precision. The resulting design can be sensitive to uncertainty in the design variables or environmental parameters [4]. The process of finding optimal solutions that are the least sensitive to uncertainty is referred to as *robust optimization.* The problem of optimizing a hypersonic vehicle with asymmetric roughness considerations inherently contains uncertainty. For example, the position or severity of surface imperfections or roughnesses are not known a priori. These parameters may change due to high stress flight conditions. This design problem is well suited for robust optimization.

Previous studies have used aerospace applications to evaluate robust optimization methods. Ong et al. [5] used an airfoil design problem to demonstrate their robust optimization scheme max-min SAEA. In a hypersonic framework, Ridolfi et al. [6] used a capsule design problem as a test-bed for their archival-based robust optimization scheme. Generally, robust optimization methods find an optimum by constructing a robust counterpart to the original objective function. The robust counterpart function can be formulated based on different philosophies and therefore may result in different categories of robust optima. For example, methods based on robust regularization [7], are based on a worst-case scenario approach: given an objective function f to be minimized, the robust optimum using robust regularization is the design that minimizes the maximum value of f over the uncertainty [4]. The most common approach is to minimize the expected value of f over the uncertainty. This is typically done through a Monte Carlo integration approximation to the expected value of f. This method is an aggregation method sometimes referred to as *explicit averaging* [6,8,9].

Both robust regularization and explicit averaging methods converge to a single robust optimum design. Engineering design problems often benefit from comparing the results from different robust optimization methods to help analyze the design space and/or aid in a final design selection. To accomplish this, a separate optimization problem needs to be formulated and solved for each method. If the designer wants to analyze the problem for a different uncertainty probability density function (PDF), then a separate optimization problem needs to be formulated and solved. This is tedious as well as computationally expensive. This reveals a missing capa-

bility in state-of-the-art robust optimization methods, specifically when applied to engineering problems. There is a need for an all encompassing robust optimization method that can provide multiple types of robust optima for many uncertainty distributions without having to repeatedly resolve the problem. This will in turn provide engineers, scientists, or designers with information to fully analyze the design space and understand the fundamental physics or principles behind the optimization problem at hand.

Successfully optimizing hypersonic vehicles under asymmetric roughness-induced boundary-layer conditions is essential to the progress of reentry vehicle technology and hypersonic projectile technology. Advancing the state of the art requires a full understanding of the design space. This can only be accomplished through accurate and inexpensive modeling of roughness-induced boundary-layer phenomena coupled with versatile optimization and robust optimization methods.

1.2 Objectives and Contributions

This work characterizes the aerodynamic sensitivities of hypersonic vehicles to asymmetric conditions and explores concepts that balance aerodynamic capability with control. To accomplish this task, an analytical waverider geometry model capable of generating a wide range of concave and convex shapes was used. An aerodynamic model was then used to approximate the aerodynamic forces and moments on the vehicles. Asymmetric flow properties were modeled to simulate the effects of an isolated surface roughness event which may occur on a vehicle (e.g.,

protruding thermal protection system (TPS) tiles, ablation). Multi-objective optimization studies were performed in order to identify vehicle shapes most robust to the moment-induced effects of an asymmetric boundary-layer. Trade-offs between controllability and vehicle performance were investigated.

In this research, a multi-objective robust counterpart formulation is proposed, where post-optimality data handling techniques can identify, among a set of Pareto-optimal solutions, the optimal worst-case scenario and expected value solutions for any uncertainty PDF. Solving the robust multi-objective formulation once produces a set of designs, thus giving the designer more information about the design space. The ability to investigate the design space and compare multiple robust optimum designs is a particularly important contribution to the field of engineering optimization, where providing context with an optimum design is often necessary and useful. This capability is a unique advancement in the state of the art and is not currently available in modern robust optimization methods. The proposed robust multi-objective optimization method was compared to three commonly used robust optimization methods. The foundations behind the proposed method, the convergence criteria, and data handling techniques are discussed in detail. A purely mathematical example problem was used to explore the capability and nuances of the proposed method.

The robust optimum results found using the data handling techniques were compared to the true robust optimum results found analytically. The proposed robust multi-objective method and the three common robust optimization methods were all applied to the vehicle design optimization problem to identify hypersonic

5

shapes that are robust to uncertain surface roughness conditions. The results and performance of each method were then compared and discussed. In particular, the potential for the multi-objective based robust optimization method to reveal design trends is illustrated through the hypersonic vehicle design problem.

In summary, the following were the main objectives of the study:

- Characterize the effects of asymmetric roughness-induced boundary-layer transition on hypersonic vehicle controllability.

- Identify hypersonic shapes best fit to withstand asymmetric flow field effects through optimization techniques.

- Explore the hypersonic vehicle design space through state-of-the-art multi-objective and robust optimization methods using genetic algorithms.

By accomplishing the objectives listed above, the following contributions have been made through this work:

- An analytical roughness-induced boundary-layer transition model was developed to explore the unknown design space of hypersonic vehicles with uncertain surface roughness conditions.

- Hypersonic vehicle shapes are classified for maximum aerodynamic performance, vehicle controllability, vehicle usability, as well as hybrid shapes acting as a compromise between these objectives.

- A novel robust multi-objective optimization method to solve single-objective optimization problems with environmental parameter uncertainty by use of

post-optimality data handling techniques was developed. The method provides a range of robust optimum results, while also capturing trade-offs in the design space, providing capabilities not available in current robust optimization methods.

1.3   Organization of the Dissertation

The remainder of this chapter provides a review of the previous work performed in the fields of hypersonic vehicle design, roughness-induced boundary-layer transition, and state-of-the-art robust optimization methods. Background knowledge and important concepts are discussed. An in-depth analysis of the hypersonic aerodynamic prediction model and pertinent assumptions used in the simulations are outlined in Chapter 2. Chapter 3 presents a detailed discussion on asymmetric boundary-layer transition (ABLT) and discusses the implementation of this phenomena into the aerodynamic model. The hypersonic aerodynamic model and the ABLT model were applied to the vehicle design problem using the methods described in Chapter 4. The design point, structure, and formulations of the optimization problems solved in this work are given in Chapter 5. The optimum designs and explanation of the results are fully outlined in Chapter 6 and summarized in Chapter 7.

The content in this dissertation is a comprehensive piece of literature pulling together previous publications by the current author while providing more detail. References [10–12] form the foundation of this dissertation.

1.4 Previous Work

1.4.1 The Design, Aerodynamics, and Optimization of Hypersonic Vehicles

The classic highly blunted, low lift-to-drag ratio (L/D), hypersonic vehicle shapes have reliably served NASA for the past 50 years. Yet, looking forward, there are particular missions of interest which may benefit from a fundamentally different aeroshell shape. For example, the human exploration of Mars have advantages from the use of mid-L/D vehicle designs due to the large landed mass requirements [13]. Aerocapture missions to Neptune would benefit greatly from high-L/D shapes by utilizing aerodynamic forces during a pass through the Neptune atmosphere to capture into orbit, instead of a large propulsive delta V maneuver.

One of the most promising classes of high-L/D hypersonic vehicle design concepts are waveriders. Waveriders are hypersonic vehicles that are designed such that the entire bow shock is on the underside of the vehicle emanating from the leading edge of the body. As a result, there is no flow spillage from the lower surface to the upper surface of the vehicle. The shockwave creates a high pressure flow which is contained beneath the vehicle, thus producing a high lift-to-drag ratio.

NASA has identified these high-L/D shapes as key research areas within the Entry, Descent, and Landing Technology Roadmap [13] and are currently funding research which are based of the waverider concept [14]. The goals of this proposed research parallel the recommended areas of investment defined in the roadmap;

the primary category of shapes investigated in this work is waveriders (see Section 2.1). However, the analysis isn't too restrictive as canonical hypersonic shapes such as wedge-like, cone-like, convex, and concave vehicle shapes are all possible candidates in the studies performed in this research. That being said, the previous work presented in this section will mainly focus on previous literature pertaining specifically to waveriders.

The concept of a waverider was first conceived in a paper by Nonweiler in 1959 [15]. His first waverider concept was derived by carving out a geometry based on the streamlines and shockwave generated from a two-dimensional hypersonic flow over a wedge. These designs were originally coined as caret waveriders. The waverider concept was further extended to include shapes that are "carved" out of more complex generating flow fields, such as flow over a non-lifting cone [16]. The generation of waverider shapes grew in complexity once again in the 1980s and 1990s, fueled by a renewed interest in hypersonic flight. Sobieczky et al. [17] introduced the method of osculating cones to generate waverider shapes with three-dimensional shock structures. Most of the previous work on the generation of waverider shapes are based of an inverse design approach: a generating flow field is first established, then the waverider design is carved out of the resulting streamlines.

In 1998, Starkey and Lewis [18] took the opposite approach. An analytical, power-law derived hypersonic waverider model was developed using two or three power-law equations to define the upper, lower, and planform shapes of the waverider. From this, five variables can be manipulated to generate a wide range of waverider styles including: caret waveriders, constant wedge angle waveriders with

planar shocks, constant wedge angle waveriders with three-dimensional shocks, and variable angle waveriders with three-dimensional shocks.

Once the waverider concept and shape generation methods were conceived, the next logical task is to evaluate the aerodynamic characteristics of waveriders. This task has been the subject of many research papers spanning from the late 1990s to the 2010s. The previous literature predicted waverider aerodynamics by using numerical, analytical, and experimental techniques. Many papers compare and contrast two or more of these approaches. The papers discussed in the next few paragraphs are a select sample of the vast number of contributions to waverider aerodynamics. These papers were selected to highlight the diversity in the aeroprediction approaches. An organized view of the theory behind most of these methods is available in Anderson [19].

Many of the legacy research papers on predicting the aerodynamic characteristics of waveriders took an *inviscid* analytical approach. Within the overarching category of an inviscid analytical approach existed numerous theories and methods. One of these theories is Piston Theory. This theory calculates pressure distributions along a waverider by assuming an analogous scenario of a piston moving into a column of fluid. This theory can be seen applied to the calculation of stability derivatives in references [20–23] as well as more recently in Oppenheimer et al. [24]. Corrections/additions to this theory have been provided by Liu et al. [25]. Liu provides a hypersonic lifting surface theory, adding the capability to account for the effects of wing thickness and/or flow incidence, upstream influence, and three-dimensionality for an arbitrary lifting surface system in an unsteady flow.

Another subset of inviscid analytical methods are surface inclination methods. These methods theoretically show that surface pressures can be approximated using only the information regarding the angle of incidence of the vehicle surfaces with respect to the freestream. These methods include Newtonian Theory, the tangent-wedge method, and the tangent-cone method. Rasmussen wrote several papers [26–28] outlining the approach and capabilities of using Newtonian Theory to analytically calculate the stability derivatives of waveriders as a function of angle of attack and sideslip angle. He also combines these efforts within the framework of hypersonic-small-disturbance theory [29].

Efforts by Starkey et al. [30] were taken to use shock expansion theory to analytically describe the aerodynamics of waveriders. His method and results were validated with numerical simulations using the waverider aeroprediction code MAXWARP (Maryland Axisymmetric Waverider Program) [31]. Comparing analytical methods with experimental and numerical results was a common theme throughout the literature.

O'Brien and Lewis [32] compared the analytical waverider aerodynamic predictions of Newtonian Theory to a three-dimensional Reynolds-Averaged Navier Stokes solver and found reasonable agreement. Cockrell et al. [33, 34] performed extensive experimental work on two cone-derived waverider shapes with engine integrated vehicle components. Comparisons were made to inviscid numerical computational fluid dynamics (CFD) solutions. It was found that the aerodynamic performance of the fully integrated configuration is severely degraded when compared to a pure waverider. Gillum and Lewis [35] used hypersonic wind tunnel results to examine

the prediction capabilities of Newtonian theory and the tangent wedge method, and to examine the effect of blunted leading edges.

The effects of blunting waverider leading edges is also seen as a topic of interest in the literature. In 1994, Blosser et al. [36] presented waverider leading edge design concepts. Blosser examines the techniques for blunting as well as the impact on leading edge heat flux, via analytical and numerical aerothermodynamic calculations. Blunting concepts and the corresponding aerothermodynamic effects has also been studied more recently by Starkey [37] and Chen et al. [38].

Research comparing analytical inviscid methods with numerical and experimental results drew attention to the importance of viscous effects. Viscous effects were found to be an important aspect to model, even in the high Reynolds number flow of the hypersonic flight regime. This implication is still emphasized in the more recent waverider publications [39–41]. The importance of modeling shear stress brought forth the task of designing waveriders with minimized viscous drag characteristics. These waveriders were coined as viscous optimized waveriders [42].

The ability to accurately (and hopefully inexpensively) predict waverider aerodynamic characteristics helped guide the research towards optimizing waveriders for particular missions. One of the first and foremost computer simulation tools used to optimize waveriders was MAXWARP [31]. The MAXWARP code has been used to generate aerodynamically optimized waverider shapes for maximum cruise mission performance, reentry missions, chemically reacting flow fields, and interplanetary missions [30]. Waverider optimization has been prevalent from the 1990s onward and is still a hot topic of research. For example, Burt et al. [43] used a simulated

annealing optimization method to optimize waverider geometries for high altitude flight, calculating the aerodynamics numerically using a Direct Simulation Monte Carlo method.

An ongoing theme stressed in this study is the fact that traditional optimization techniques tend to find optimum designs which are sensitive to off-design conditions (either in design parameters or environmental parameters). The literature shows that waverider optimization follows this tendency. However, it is important to note that this sensitivity is not only attributed as a side-effect of optimization, but also as a performance characteristic of waveriders in general. Much of the waverider literature in the late 1990s and early 2000s studied the changes in waverider aerodynamic performance for off-design conditions. Two main off-design categories were investigated: off-design Mach number and off-design attitude (i.e. changes in angle of attack and/or sideslip angle).

Tarpley et al. [22, 44] presented a hybrid method to predict the aerodynamics of waveriders for both on- and off-design conditions (including both Mach number and attitude changes). Linear piston theory was used to calculate on-design aerodynamics coupled with tangent wedge and tangent cone methods for the off design regime. The main assumption made was that the shockwave is still attached to the leading edge, even in the off-design conditions. This assumption is somewhat limiting, due to the fact that this would only remain true for small perturbations in freestream Mach number and attitude angles.

For larger perturbations in freestream Mach number, Takashima et al. [42] found that lift-to-drag ratio performance didn't suffer significantly. The lift-to-drag

ratio for a waverider with a design Mach number of six changed by a maximum of 13.5% over a freestream Mach number spanning from four to eight. When extrapolating this effect to a hypothetical waverider mission, Takashima et al. [45] found that when a waverider accelerates through an off-design Mach number to reach cruise conditions, mission parameters like maximum range aren't greatly affected. Even though the overall parameters like lift-to-drag ratio and range aren't greatly affected, Mazhul and Rakchimov [46] found that the shock structures produced by the waverider can in fact be vastly different in configuration for off-design Mach numbers and angles of attack.

Changes in shock structure and flow physics around a waverider are even more exaggerated when considering off-design sideslip conditions. This is seen in Shi et al. [47,48], where CFD simulations were run to analyze waveriders at sideslip conditions. Shi found that a waverider at sideslip conditions produces a complex asymmetric flow field with intricate shock structures. Shockwave boundary-layer interaction was found to occur for Mach numbers faster than the design Mach number. At an angle of attack, the shock detaches and the presence of a small separation bubble and a vortex on upper surface was observed. These flow structures strongly affect the waverider pressure and skin-friction coefficient distributions.

Once the research on waverider aerodynamics simulation and experimentation matured, the community started ramping up hypersonic flight tests [49]. Real-world scenarios revealed more concern about the stability and control of waveriders and hypersonic vehicles. The cause of concern is asymmetric boundary-layer transition [1]. In particular, roughness-induced boundary-layer transition was identified as one

of the most important aspects to study [2, 50, 51]. Previous literature pertaining to roughness-induced boundary-layer transition is reviewed in Section 1.4.2.

1.4.2   Roughness-Induced Boundary-Layer Transition

Boundary-layer transition is a complex phenomena influenced by many contributing factors including, but not limited to, Reynolds number, crossflow, freestream turbulence levels, wall temperature, and vibrations [52]. Among all factors, it has been found that transition can become completely dominated by roughness or ablation effects [53]. As expected with any topic pertaining to turbulence, the research community has been studying roughness-induced boundary-layer transition for a long time, without any sign of slowing down. This may be contributed to the complex nature of the problem coupled with the continuous improvements of ground test facilities, instrumentation, and numerical simulations.

This section has no intention of providing a *complete* review on all of the previous research involving this topic. The history is simply too long and too vast. Highlights of several historically significant papers will be given and an emphasis will be placed on discussing the status of the state-of-the-art. For a more complete background and history of the literature, a survey paper on hypersonic roughness-induced boundary-layer transition has been written by Schneider [53]. Also, Zhong and Wang [54] provide a thorough discussion on the background and literature pertaining to hypersonic boundary-layer receptivity, instability, and transition.

An analysis of roughness elements disturbing laminar flow and inducing tran-

sition can be seen published in the literature as far back as the early 1930s, where Schiller suggested that "the critical height of the excrescence that disturbs the laminar boundary-layer and causes its transition to turbulent flow is the height at which vortices form behind the excrescence" [55]. Early experimental efforts to visualize and explain the physical phenomena responsible for forming the "wedge" of turbulence behind the roughness were completed by Gregory and Walker [56]. These visualization-based studies were extrapolated to hypersonic conditions for conical reentry shapes in 1968 by Canning et al. [57]. Ablative visualization techniques were used, thus by design, highlighting the importance of turbulence wedge local heat flux implications.

The flow structures produced by an isolated roughness in a laminar flow field have stemmed vast amounts of research in of itself. For example, Acarlar and Smith [58] performed experimental studies to exhaustively illustrate and explain the standing horseshoe vortex and shedding hairpin vortex structures produced by an isolated roughness element. Current research studies are still focused around explaining these structures and their subsequent breakdown into a turbulence wedge [59].

The previous literature has also focused on the turbulence wedge downstream of the roughness element. In 1972, Fischer [60] compiled lateral spreading angle data from a wide variety of turbulence wedge experiments. His turbulence wedge spreading data correlation with freestream Mach number is often cited in the previous literature as a validating reference. Even 40 years later, current numerical and experimental papers cite Fischer to validate their measurements [53, 61–63].

Visualizing the turbulence wedge structure is a common approach in both experimental and numerical studies, due to the inherent three-dimensional nature of the flow physics. Experiments performed by Danehy et al. [64, 65] employ planar laser-induced fluorescence (PLIF) techniques to visualize the wall normal and planform planes of flat plate experiments. Numerical validation of the results published by Danehy et al. using direct numerical simulation (DNS) was performed by Iyer et al. [66], further illustrating the interest in roughness-induced boundary-layer transition from both the experimental and numerical research communities.

A common approach taken in the most current literature, is to analyze the numerical stability of the hypersonic boundary-layers. A state-of-the-art suite of codes called STABL and STABL-3D was developed by Candler et al. at the University of Minnesota [67]. This computer code solves hypersonic boundary-layer transition problems using both linear stability theory and parabolized stability equation solutions.

1.4.3 Robust Optimization

The concepts behind robust optimization have been developed independently in many scientific fields, yet can arguably be traced back the furthest in engineering, specifically the field of "quality engineering" [4]. The roots of robust optimization in quality engineering were most strongly planted by Taguchi in the mid 1980s. Taguchi laid the foundation of the techniques and philosophies for quantifying robustness. Taguchi followed a Design of Experiments (DOE) approach, rather than formal

optimization methods, to carry out the process and find robust designs [68].

Since the 1980s, many disciplines have built off of the idea of robustness and applied formal analytical and numerical optimization techniques, making great strides advancing the field. This section serves as a select literature review of the state-of-the-art methods and techniques in robust optimization. Comprehensive literature reviews and survey papers have been written by Beyer and Sendhoff [4], Jin [8] and Kruisselbrink [9] and are recommended for further review.

1.4.3.1 Formulations

Generally, robust optimization methods incorporate uncertainty by constructing robust counterpart objective functions F to the original objective function f [4]. This counterpart function is based off of a particular "philosophy" or statistical representation of uncertainty. For example, worst-case scenario methods use a minimax-type formulation in order to construct a robust counterpart function. Aggregation methods form robust counterparts based on the mathematical moments of f over the uncertainty.

The worst-case scenario form of accounting for uncertainty is directly analogous to the minimax approximation in the field of applied mathematics [69]. This method appears in research spanning multiple disciplines and may be referred to as minimax, robust regularization [7], or simply as a robust counterpart approach [70].

For a minimization optimization problem, methods based on robust regularization minimize the maximum f value over the uncertainty. The robust regularization

technique is nominally used when uncertainty is modeled *deterministically*. For optimization problems where the uncertainty is modeled *probabilistically*, probability measures are provided describing the likelihood for a particular value of the uncertain variable to occur in the domain of interest [4]. Probabilistically modeled uncertainty problems can also be solved with this method, as long as an upper and lower bound on the uncertain variable can be defined.

The robust regularization approach is considered as a worst-case scenario and may be too conservative for some applications. Sometimes the worst-case scenario robust result is infeasible for a particular problem. In such applications, a probabilistic aggregation approach to forming a robust counterpart function is often used. Utility aggregation functions such as expected value, variance, and other higher order moments of f can be used. For many optimization problems, the objective function f isn't in analytical form, and therefore numerical representations of these utility functions need to be used. Seemingly the most common utility function used in robust optimization is the conditional expectation of f [5, 6, 8, 9, 71–75]. The simplest way of calculating the expected value of the original objective function for a particular distribution of uncertainty is through explicit averaging [6, 8, 9].

In the context of applying evolutionary or genetic algorithms, Tsutsui et al. [72,73] developed a more efficient variation of the explicit averaging method. Explicit averaging was reduced from taking an average fitness over n samples to adding a stochastic perturbation to each design in the population for a given generation. Much of the previous work using this perturbation method covered uncertainty in the design variables, while a few others [5, 74] have found applications using other

19

types of uncertainties. For an infinite population size, it has been shown that the perturbation method is equivalent to the explicit averaging method [4,8,74,75]. Also note that if $n = 1$ and the perturbation (Δp, Δx, Δf, etc.) is chosen randomly per generation, then the explicit averaging method is equivalent to the perturbation method.

Another option investigated in the literature is a robust meta-model approach. This approach ties in robustness by constructing a meta-model approximation and solving for an estimated robust design. Response surface methodology, neural networks, and Kriging models have all been proposed. Two good reviews on meta-modeling techniques have been published by Simpson et al. and Jin [76,77].

Beyer and Sendhoff [4] note several problems about the effectiveness of the meta-modeling approach:

1. These techniques are not well suited for large-scale robust optimization problems, when the number of design variables is large.

2. For a fully quadratic response surface, the meta-model must be repeatedly applied in order to get closer to the robust optimum. It is unlikely that the quadratic meta-model represents the robust counterpart adequately.

3. The computational efficiency of the meta-model approach is at least questionable. It is not clear what the response surface really produces as iteration time approaches infinity. Up to now, no proof has been presented that this methodology yields a robust optimum.

Even with these weaknesses, the method is still applied in the literature. If the

number of design variables are small, and a simple response surface is used, the meta-modeling technique can be computationally efficient as seen by Elster and Neumaier [78].

The robust counterpart approach (with or without meta-modeling) form an optimization problem aimed at minimizing a utility function (i.e. expected value) accounting for the uncertainty. It has been identified in the literature that optimizing the expected value may lead to a design with a large variance; this is not always desirable [4]. Some of the previous literature address this problem by using an a priori aggregation scheme [79–81]. These methods assign weights of importance to variance and expected value measures, aggregating them into a single-objective problem. The current state-of-the-art robust optimization methods address this problem by forming multi-objective problems using the variance and expected value as conflicting objective functions [4, 9, 74].

The multi-objective formulations have been solved using both deterministic and heuristic methods. For example, Das [82] solves for a Pareto-optimal front between variance and expected value objective functions using a deterministic non-linear programming method. Chen [83] and Rolander et al. [84] formulate their multi-objective problem in a compromise programming (or sometimes called goal programming) structure.

Solving the robust multi-objective formulations using genetic algorithms is a budding research area. Jin and Sendhoff [74] solve a two objective function optimization problem using genetic algorithms. The objective function f and the variance of f over the uncertainty act as the two conflicting objectives. Ray [85] adds one more

objective forming a three objective function robust optimization problem, solved using evolutionary algorithms. Here the objective function f, the mean value of f and the variance of f act as the three conflicting functions. An interesting extension to this category of heuristic-based solvers can be seen in Sorensen [86]. Sorensen uses a meta-heuristic method, called tabu search, to search for robust optimum solutions. These state-of-the-art multi-objective formulations and methods are only a first step towards providing the designer with more insight into the nature of the robust design space. These methods are still limited to one particular uncertainty PDF for one nominal value of the uncertain variable. The methods are also limited to providing robust optimum answers based on moments of the uncertainty (expected value, variance, etc.) *or* worst-case scenario robust optimum answers. The literature review completed for the current study found no methods that can concurrently provide *both* of these types of robust optima.

The current work developed a novel robust multi-objective optimization formulation and method which allows for post-optimality data handling techniques to find robust optimum designs that follow the worst-case scenario and best mean fitness approaches of robust regularization and explicit averaging. This can be seen as an a posteriori aggregation method to contrast the aforementioned a priori aggregation methods. Ideally, this method has the ability to post-optimally pick designs that are most robust for any uncertainty PDF and for various nominal values or the uncertain parameter. Therefore, many types of results can be identified and analyzed by solving only one multi-objective optimization problem.

Chapter 2:   Hypersonic Aerodynamics

The aerodynamic model was constructed using multiple different aerodynamic approximation theories and methods. Certain methods are only applicable to vehicles with an infinitely sharp leading edge, while others must be used for a blunted leading edge. The model is discussed in two subsections based on the leading edge conditions. For both leading edge conditions, the flow over the waverider is assumed to be two-dimensional with streamlines flowing straight back over the vehicle. This assumption was also made by Starkey in his analytical calculations [30] and validated with CFD results [87]. The aerodynamic model for waveriders with infinitely sharp leading edges is based off the work presented by Starkey [30]. The analysis of blunted leading edges, however, required several modifications and extensions in order to render the approach applicable to a blunted leading edge. Gillum and Lewis [35], using experimental measurements, found that blunted waverider aerodynamic coefficients can be accurately predicted using tangent-wedge and Newtonian theory approximations. The results found by Gillum and Lewis serve as validation to the approach taken in this work. The overall aerodynamic analysis in this work is implemented as a panel method, where the waverider geometry is constructed as a mesh and the aerodynamic calculations are applied to differential area elements.

2.1 Vehicle Geometry

Starkey [30] developed an analytical description of waverider geometries that uses three, two-dimensional power-law equations to generate a parametric hypersonic vehicle with a three-dimensional shock. The curvature of the planform (p) and upper surfaces (u) are defined by

$$y_p = Ax^n \ , \ y_u = Bz_u^n \ . \tag{2.1}$$

The curvature of the lower surface (l) can be defined either for a convex vehicle (cv) or a concave vehicle (cc) by

$$y_{l,cv} = C_{cv}\left(-z_{l,cv} + x\tan\theta\right)^m \ , \ y_{l,cc} = C_{cc}\left(z_{l,cc} - x\tan\theta\right)^m \ . \tag{2.2}$$

These equations allow for the generation of a wide variety of vehicle geometries. An example of a convex vehicle derived using these equations is shown in Figure 2.1, and a concave vehicle in Figure 2.2. By varying the constants A, B, C, m, and n in Equations 2.1 and 2.2, geometries from highly convex shapes to highly concave shapes, representing a range of low lift-to-drag ratio shapes to high lift-to-drag ratio shapes can be modeled. This methodology for defining a vehicle geometry with infinitely sharp leading edges was used in the current study.

A modification to Starkey's method was made to allow for a parametric description of leading edge bluntness. There are two ways to blunt the leading edge of an initially sharp vehicle: one is to remove or "sandpaper" the leading edge down to a desired shape, the second is to separate the upper and lower surfaces and add material to create the desired leading edge. The latter method was chosen here
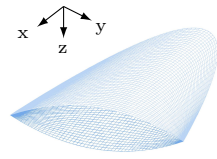
(a) Isometric view   (b) Planform view
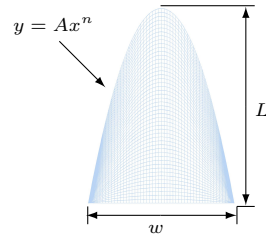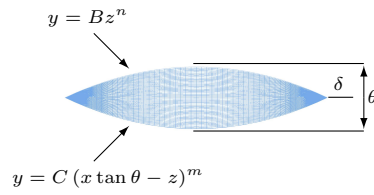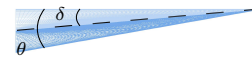
(c) Rear View   (d) Side View

Figure 2.1: Example convex parametric waverider shape.
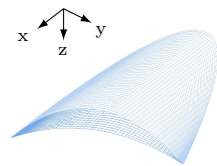
(a) Isometric View   (b) Planform View
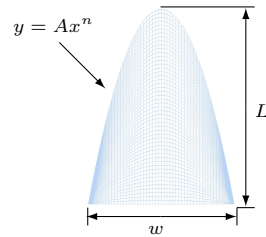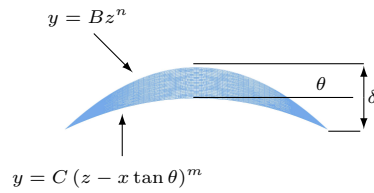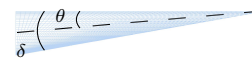
(c) Rear View   (d) Side View

Figure 2.2: Example concave parametric waverider shape.

as suggested by Starkey [37]. An upper and lower surface separation distance, d, was added to the list of variables defining the vehicle geometry. The side cross section of the blunted leading edge was prescribed as a semicircle. The radius of the semicircle varies with spanwise location (y direction) such that the leading edge is always tangent to the lower surface. An example blunted waverider shape is shown in Figure 2.3. The profile shapes of the infinitely sharp and blunted waveriders at each spanwise location are a wedge and a blunted wedge as seen in Figure 2.2(d) and Figure 2.3(d) respectively.

(a) Isometric View

(b) Planform View

(c) Rear View

(d) Side View
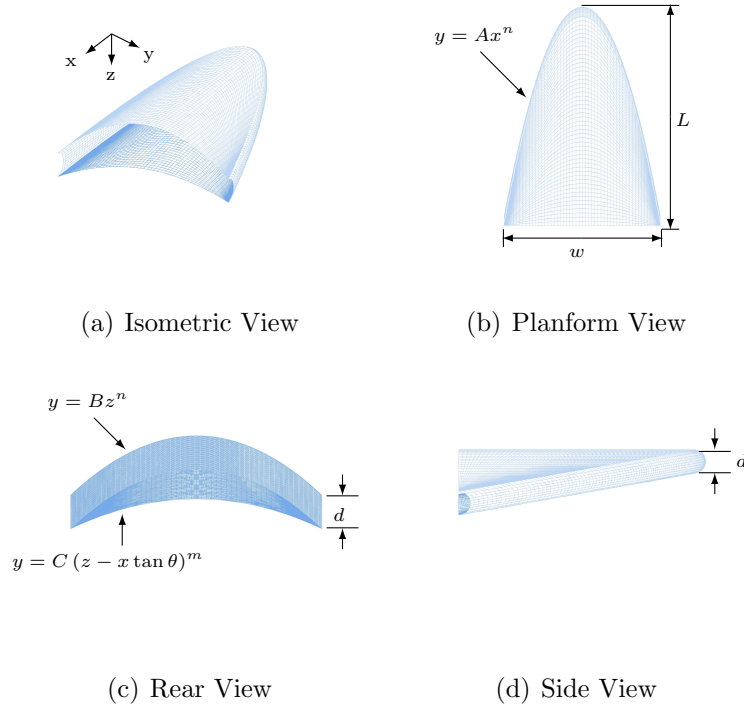
Figure 2.3: Example blunted concave parametric waverider shape.

26

2.2   Infinitely Sharp Leading Edge

2.2.1   Pressure Forces

The vehicle geometry modeling in Section 2.1 generates a wedge profile at each spanwise location on the vehicle, with the top surface oriented parallel with the freestream. When assuming two-dimensional flow, the top surface flow properties are equal to the freestream. A constraint was placed in the optimization schemes (see Chapter 5) limiting the wedge deflection angle of the bottom surface at any given spanwise location θ_{local}, to be less than the maximum deflection angle θ_{max} allowed for an attached shockwave. With these assumptions, the lower surface properties can be calculated using oblique shock theory. Flow properties on the top and bottom surfaces of the waverider are approximated using perfect gas and isentropic relations.

The vehicle geometry is discretized into a mesh with a finite number of differential areas or panels. Examples of these meshes are seen in Figures 2.1 and 2.2. A local deflection angle and a local shockwave angle exists at each spanwise location. Oblique shock relations are used to find the properties on the lower surface of the waverider. The lift, drag, and side forces are calculated by multiplying panel surface pressure by the corresponding differential area, splitting the force into components as determined by the unit normal direction of the panel, and summing over all panels. The base pressure is assumed to be equal to the freestream pressure. A profile cross-section view of the pressures at a given span can be seen in Figure 2.4.
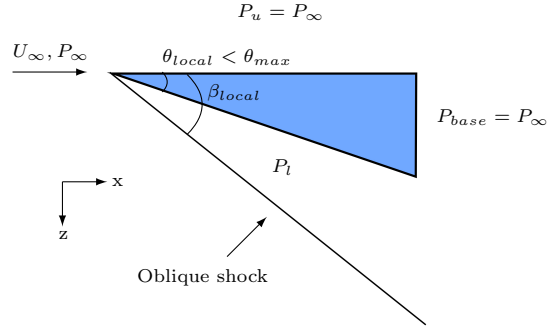
Figure 2.4: Profile cross-section view at some given local span location.

2.2.2 Viscous Forces

Laminar and turbulent viscous forces for the top and bottom surfaces of the waverider are calculated using the reference temperature method after applying a flat plate assumption to the compressible boundary-layer equations [88]. The laminar shear stress at the wall is given by

$$\tau_{w,lam} \approx 0.332 \rho_e {U_e}^2 \sqrt{\frac{Ch^\dagger}{Re_{x,e}}} \; , \tag{2.3}$$

where subscript e represents boundary-layer edge conditions and superscript $\dagger$ represents average boundary-layer conditions. The boundary-layer edge conditions are given by the flow properties calculated in Section 2.2.1. The Chapman-Rubesin parameter $Ch^\dagger$ is found using the power-law viscosity approximation given by

$$Ch^\dagger = \left(\frac{T^\dagger}{T_e}\right)^{-\frac{1}{3}} \; , \tag{2.4}$$

28

where $\frac{T^\dagger}{T_e}$ is found using Eckert's empirical estimate for the average boundary-layer temperature given by

$$\frac{T^\dagger}{T_e} \approx 0.5 + 0.039 M_e^2 + 0.5\frac{T_w}{T_e} \ . \tag{2.5}$$

The wall temperature T_w is approximated as 1200K. This is a reasonable estimate for hypersonic vehicles at cruise conditions assuming active wall cooling [30].

The turbulent shear stress at the wall is found by utilizing the power-law approximation for flat plates [88] given by

$$\tau_{w,turb} \approx \frac{0.0592\rho^\dagger U_e^2}{2\left(Re^\dagger\right)^{0.2}} \ , \tag{2.6}$$

where

$$Re^\dagger = \frac{\rho^\dagger U_e x}{\mu^\dagger} \ , \tag{2.7}$$

$$\rho^\dagger = \frac{P_e}{RT^\dagger} \ . \tag{2.8}$$

The viscosity $\mu^\dagger$ is calculated using Sutherland's formula at temperature $T^\dagger$. Once the wall shear stress is calculated for each panel, the viscous force can be found by multiplying the shear stress with the corresponding differential area. A small angle approximation is used, assuming the friction force only contributes to drag in the x direction and therefore has zero contribution to lift or side force.

2.2.3 Moment Calculations

Contributions to the roll, pitch, and yaw moment coefficients are given by both the pressure forces and the viscous forces. The pressure force moment coefficient vector is defined as

$$\vec{C}_{M_{CG,press}} \equiv \frac{\vec{M}_{CG,press}}{\frac{1}{2}\rho_\infty U_\infty^2 S_p L} \ , \tag{2.9}$$

where S_p is the planform area, L is the length of the vehicle, and $\vec{M}_{CG,press}$ is the moment vector about the center of gravity due to pressure forces given by

$$\vec{M}_{CG,press} = \sum_{i=1}^{N} (PdA)_i \, (\vec{r}_i \times \hat{n}_i) \ , \tag{2.10}$$

where subscript i represents a given panel in the waverider mesh, N is the total number of panels making up the entire surface (top and bottom) of the waverider, dA is the area of the panel, $\hat{n}$ is the outward unit normal of the panel, and $\vec{r}$ is a position vector from the vehicle center of gravity to the centroid of the panel.

The viscous force contribution to the moment coefficient vector is found by applying a small-angle approximation. The wedge angles are assumed to be small enough that the shear stress on the lower surface can be approximated as pointing purely in the drag direction. Therefore, the moment coefficient is defined as

$$\vec{C}_{M_{CG,visc}} \equiv \frac{\vec{M}_{CG,visc}}{\frac{1}{2}\rho_\infty U_\infty^2 S_p L} \ , \tag{2.11}$$

where $\vec{M}_{CG,visc}$ is the moment vector about the center of gravity due to viscous forces given by

$$\vec{M}_{CG,visc} = \begin{bmatrix} M_{xCG,visc} & M_{yCG,visc} & M_{zCG,visc} \end{bmatrix} \ , \tag{2.12}$$

where

$$M_{xCG,visc} = 0 \ ,$$

$$M_{yCG,visc} = \sum_{i=1}^{N} (\tau_w dA r_z)_i \ , \tag{2.13}$$

$$M_{zCG,visc} = \sum_{i=1}^{N} (\tau_w dA r_y)_i \ .$$

The variables r_y and r_z are the distances from the center of gravity to the panel centroid in the y and z directions respectively. $M_{xCG,visc}$ is equal to zero because the

shear stress points strictly in the x direction. The total moment coefficient vector (x, y, and z components are roll, pitch, and yaw respectively) is the sum of the pressure and the viscous contributions

$$\vec{C}_{M_{CG,tot}} = \vec{C}_{M_{CG,press}} + \vec{C}_{M_{CG,visc}} . \tag{2.14}$$

2.3 Blunted Leading Edge

2.3.1 Pressure Forces

The geometry model in Section 2.1 for a blunted leading edge waverider generates a blunted wedge profile at each spanwise location on the vehicle, with the top surface oriented parallel with the freestream, as illustrated in Figure 2.5. As opposed to the infinitely sharp leading edge, where an attached shockwave is present, a blunted leading edge produces a bow shock. Predicting the bow shock shape and calculating the flow field downstream of the shock is a "daunting task" and is often calculated using CFD [19]. The goal of the current work was to construct a more computationally inexpensive aerodynamic prediction model so that optimization schemes can be implemented. Therefore, a more appropriate approach was to use surface inclination methods.

Modified Newtonian Theory is most suited for blunt surfaces where the deflection angle is greater than the max deflection angle allowed for an attached oblique shock wave. For more slender shapes, tangent-wedge, tangent-cone, or shock expansion method is more accurate [19]. For the blunted wedge shapes of interest in this work, a hybrid approach was taken. For the blunted leading edge section, region
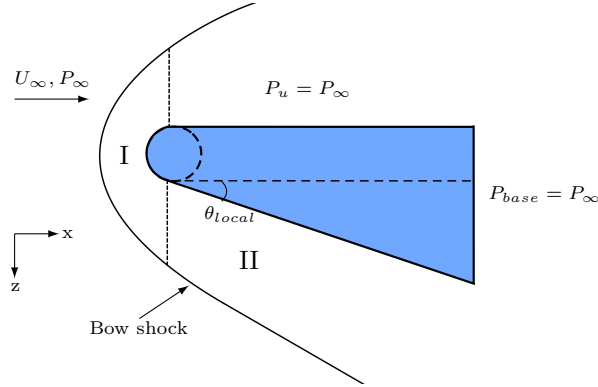
Figure 2.5: Profile cross-section view at some given local span location.

I in Figure 2.5, Modified Newtonian Theory is applied to approximate the surface pressure. For the lower surface, region II in the figure, the local inclination angle is checked to see if it is greater than or less than the max deflection angle θ_{max}. If the local wedge angle is greater than the max deflection angle, Modified Newtonian Theory is applied to approximate the surface pressure. If the local deflection angle is less than the maximum deflection angle, then a tangent-wedge approximation is used. This hybrid approach was coupled with the perfect gas and isentropic relations to approximate additional flow properties on the leading edge and the bottom surface of the waverider. The lift, drag, and side forces are calculated by multiplying each panel surface pressure by the corresponding differential area, splitting up the force into components as determined by the unit normal direction of the panel, and then summing over all of the panels. As in the infinitely sharp leading edge case, the top and base surface flow properties are assumed to be equal to the freestream conditions.

Using one or many different surface inclination methods to approximate pressures is common in the preliminary design of hypersonic vehicles [19]. Yet, surface inclination methods do not model flow spillage or leaking that is known to occur for blunted waverider bodies [38]. Past studies have shown that even with an appreciable bow shock stand-off distance, significant spillage does not occur [36]. For this study, flow spillage was assumed negligible.

2.3.2 Viscous Forces and Leading Edge Heat Flux

The laminar and turbulent viscous drag calculations for the upper and lower surface of the blunted waverider are performed using the methods outlined for the sharp leading edge waverider, but now the boundary-layer edge conditions (denoted by subscript e in the equations) are calculated using the hybrid surface inclination method described in the previous section.

The flat plate assumption inherent in Equations 2.3 and 2.6 no longer holds for the curved blunt leading edge surface. Solutions to the boundary-layer equations for the blunted leading edge will have a dependence on a pressure gradient parameter $\bar{\beta}$. Calculations of shear stress and heat flux along the leading edge are performed using a method formulated by Bae and Emanuel [89, 90]. This method enables all the boundary-layer properties to be determined by a set of two-dimensional lookup tables as a function of $\bar{\beta}$ and g_w. The parameter g_w is the temperature ratio defined by

$$g_w = \frac{T_w}{T_{0e}} \; . \tag{2.15}$$

The method uses laminar compressible similarity equations under the assumptions of steady flow of a perfect gas with unity values for the Prandtl number and Chapman-Rubesin parameter given by

$$\psi''' + \psi\psi'' + \bar{\beta}\left[g_w + (1 - g_w)H - \psi'^2\right] = 0 \ , \tag{2.16}$$

$$H'' + \psi H' = 0 \ . \tag{2.17}$$

The bounding wall is assumed impermeable and the flow is assumed two-dimensional. Numerical solutions for Equations 2.16 and 2.17 were calculated by Emanuel for a range of $\bar{\beta}$ and g_w values. Resulting data for ψ''_w and H'_w was compiled into two-dimensional tables [89].

$\bar{\beta}$ and g_w values are calculated for each panel on the blunted leading edge of the waverider. By interpolating from the tables described above, ψ''_w and H'_w values are calculated. Shear stress at the wall, τ_w, and heat flux at wall, q_w, were then found by transforming the ψ''_w and H'_w values back to the physical plane. The viscous drag is found by calculating the τ_w component in the x direction and multiplying by the corresponding differential area of each panel, then summing over all panels. The sum of the viscous forces in the z direction is assumed to be negligible due to near symmetry above and below the stagnation point on the leading edge. Figure 2.6 below exemplifies the breakdown of τ_w into the x and z components τ_{w_x} and τ_{w_z}, respectively.
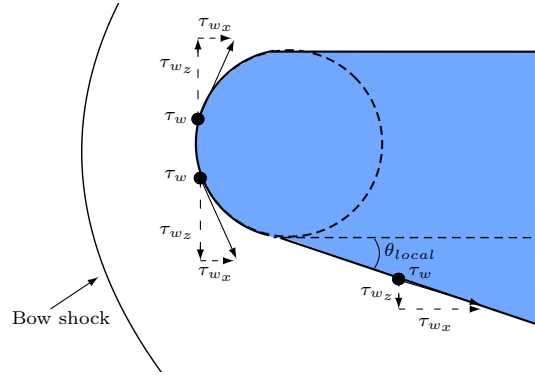
Figure 2.6: Shear stress components in the x and z directions.

2.3.3 Moment Calculations

Contributions to the roll, pitch, and yaw moment coefficients from pressure forces for the top, bottom, and leading edge surfaces are given by Equation 2.9. The viscous contribution for the top and bottom surface is given by Equation 2.11. The *leading edge* viscous contribution to the moment coefficients are calculated using Equations 2.11 through 2.13, but using τ_{w_x} instead of τ_w.

Chapter 3:   Asymmetric Boundary-Layer Transition

In hypersonic vehicle design, modeling boundary-layer transition is important for prediction and control of heat transfer and skin friction on the vehicle. By extension, predicting boundary-layer transition is crucial in designing a vehicle's TPS and GNC (guidance, navigation, and control) system. Transition is a complex phenomena influenced by many contributing factors including, but not limited to, Reynolds number, crossflow, freestream turbulence levels, wall temperature, and vibrations [52]. Among all factors, it has been found that transition can become completely dominated by roughness or ablation effects [53]. This allows the current work to take an approach that assumes, somewhere along the surface of the vehicle, an isolated roughness is present and the effects are strong enough to dominate transition.

3.1   Roughness-Induced Transition

There appears to be at least three fundamentally different ways by which roughness affects transition [53]:

1. Roughness generates a wake with streamwise vorticity and a possibly unstable shear layer. This wake may transition to turbulence immediately behind an

effective roughness.

2. Streamwise vorticity behind a small roughness element can grow via instability mechanisms such as stationary crossflow, Görtler, or transient growth. These instabilities then lead to transition.

3. Roughness can interact with acoustic waves or freestream disturbances generating instability waves.

The first of these three modes is the most understood and was the focus for developing the model in the present study. The goal of the current work was to model the roughness-induced transition as computationally inexpensively as possible while retaining as much physical accuracy as possible. This was done by analyzing the physical effects of surface roughness on transition, identifying any parametric trends that exist, then establishing simplifying assumptions. The following sections outline this approach and give a summary of the physical effects, parametric trends, and the model which was developed. For a more detailed analysis, a comprehensive literature review of the effects of roughness on hypersonic boundary-layer transition was written by Schneider [53].

3.1.1 Physical Effects

Surface roughness is usually categorized into two types: isolated or distributed. Isolated roughness includes steps, gaps, joints, or discrete machining flaws. Distributed roughness may include machining or finishing patterns on a surface or screw threads [53]. The present study focused on the effects of an isolated rough-

ness since more experimental and computational work has been carried out with this type.

An isolated surface roughness promotes boundary-layer transition producing a turbulence wedge downstream of the disturbance. The establishment of a turbulent wedge starts with a single disturbance source in a laminar boundary-layer. A standing horseshoe vortex system develops around the roughness element and trails some distance downstream until a breakdown into turbulence occurs. The breakdown produces a near perfect symmetrical pattern of turbulent flow. Unsteady structures within the turbulent region break down into smaller substructures which grow in the spanwise direction as they propagate downstream [59, 66]. Turbulence wedges generated by the presence of an isolated surface roughness element exist in subsonic, supersonic, and hypersonic flows. Examples of typical turbulence wedges produced by an isolated roughness in a hypersonic flow field are shown in Figure 3.1.

3.1.2 Parametric Trends

3.1.2.1 Roughness Height and Effective Roughness

In general, roughness affects boundary-layer transition by moving the transition point upstream of the transition location for a smooth wall. The amount of upstream movement increases with roughness height. At a particular height, the transition location will be located close to the roughness element, and any further increase in height will cause a larger disturbance but will not move the location any further upstream. This roughness condition is termed effective [53].
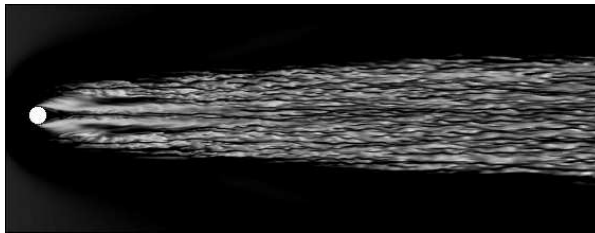
(a) Instantaneous velocity contours at a wall normal

plane ($M_\infty = 3.37$). [66]
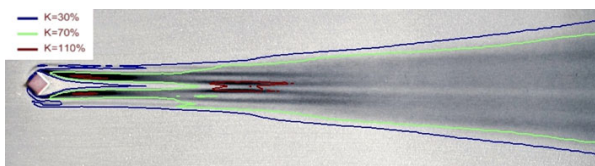
(b) Sublimation pattern and turbulent heat flux of

wake past isolated roughness ($M_e = 2.9$). [91]

Figure 3.1: Example turbulence wedge generated from isolated surface roughness [66, 91].

The effective roughness height is dependent on several factors including boundary-layer edge Mach number, position of the roughness with respect to the leading edge, and wall temperature. The present work assumes that any disturbance modeled on a vehicle will be effective. Shocks are regularly seen in schleiren images for roughness elements of heights larger than the boundary-layer thickness [53]. A key assumption in the current work is that the roughness height will be on the order of the boundary-layer thickness or smaller. Therefore, no additional shocks as a result of the roughness were modeled .

3.1.2.2 Roughness Shape

Effective isolated roughnesses promote boundary-layer transition efficiently, yet transition may still occur at a certain distance downstream of the trip location. The distance between the trip location and transition location is found to be affected by factors such as boundary-layer edge Mach number and the roughness shape.

Tirtey et al. [91] experimentally produced turbulence wedges using a variety of isolated roughness shapes shown in Figure 3.2(a). Infrared thermography measurements were taken to characterize the heat load distribution in the wake of the roughness. A modified Stanton number distribution along the centerline of the turbulence wedge was calculated for each roughness shape. Resulting distributions were compared to laminar and turbulent theoretical results (calculated using Eckert's reference temperature method). The comparison plot is given in Figure 3.2(b). The dashed lines show that for all cases, areas outside of the turbulent wedge wake are well approximated by laminar flat plate theory. The solid lines show that upstream of the disturbance, the flow is also approximately laminar. At the centerline of the turbulence wedges downstream of the roughness, the solid lines show that the flow will eventually fully transition to turbulence. When fully turbulent, the flow is well approximated by theoretical calculations. For the same freestream conditions, the shape of the roughness strongly influences how quickly or effectively the flow is tripped from laminar to turbulent.

The model constructed in the present work did not assume any particular roughness geometry. Rather, an assumption was made that at a particular location

on the surface of the vehicle, an isolated roughness disturbance exists such that flow

will transition to a fully turbulent boundary-layer immediately downstream.
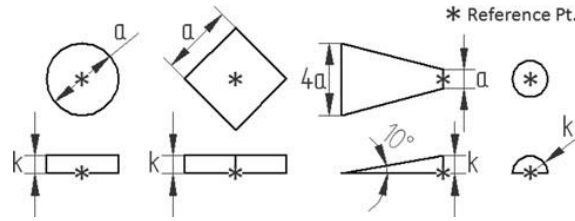
(a) Roughness element geometries
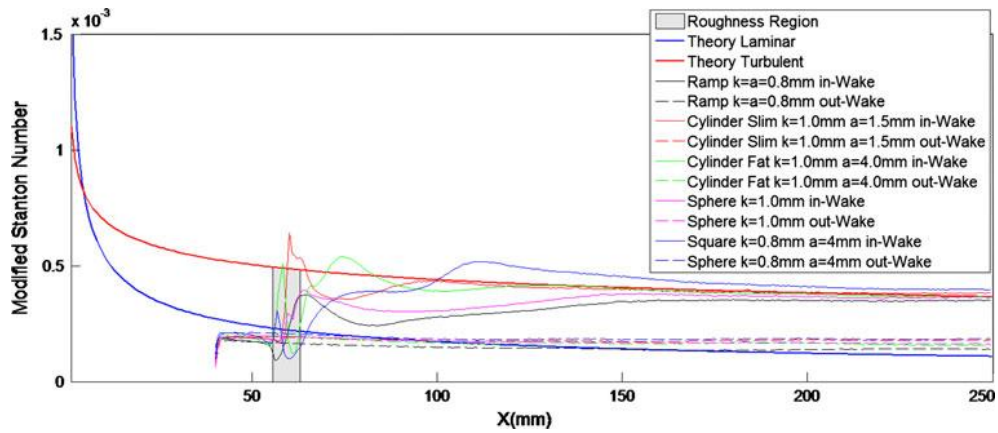
(b) Modified Stanton number distribution along wake axis compared to laminar and

turbulent heating theoretical predictions

Figure 3.2: Effect of roughness shape on transition from Tirtey et al. [91]

3.1.2.3   Turbulence Wedge Spreading Angle

The spanwise growth of the turbulent region as it moves downstream of a sur-

face roughness is measured by a lateral spreading angle. The lateral spreading angle

is defined as the half-angle of the turbulence wedge assuming symmetrical growth in

the lateral direction. Fischer [60] shows a parametric trend existing between Mach

number and spreading angle. Although not pursued in the current work, the prob-

lem still remains to be studied to rule out any other parametric trends that may exist (e.g., possibly with wall temperature [63] or tunnel noise [53]).

Fischer compiled lateral spreading angle data from a wide variety of turbulence wedge experiments [60]. Variation of the lateral spreading angle with boundary-layer edge Mach number is presented in Figure 3.3. The figure shows that with increasing boundary-layer edge Mach number, the spreading angle decreases.
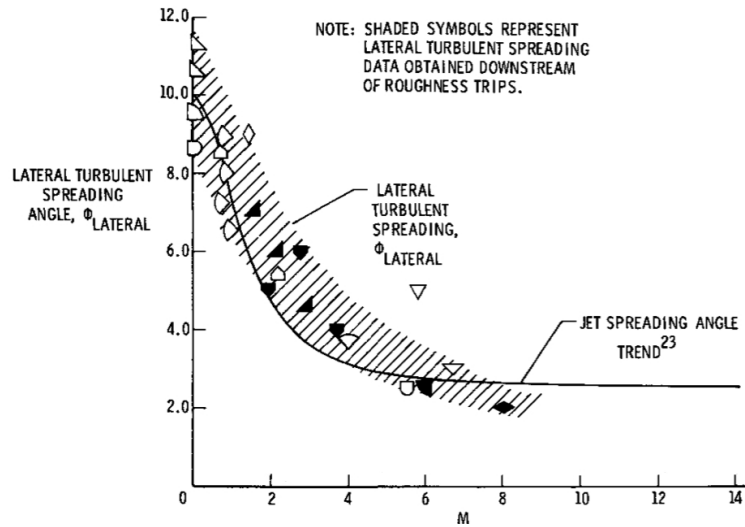
Figure 3.3: Variation of turbulent spreading with boundary-layer edge Mach number adapted from Fischer [60].

The turbulence wedge model constructed for the current work (described in Section 3.1.3) requires a lateral spreading angle to define the area on the waverider where the turbulence wedge exists. This spreading angle was approximated by the value of the data point that vertically bisects the shaded region of Figure 3.3 at a given Mach number. For example, at a Mach number of 4, the shaded region spans from 3.0° to 5.0°. So, the resulting spreading angle for a design Mach number of 4 would be approximated as 4.0°.

42

3.1.3 Turbulence Wedge Model

One of the goals in this study is to inexpensively model the aerodynamics, in efforts to employ optimization methods. To accomplish this, roughness-induced boundary-layer transition was *not* modeled using any CFD or numerical boundary-layer transition theory (e.g. Johnson and Candler [67]). To model the influence of surface deformations or roughness on a hypersonic vehicle, several simplifying assumptions are made. The disturbance is assumed to be severe enough to fully trip the boundary-layer immediately downstream of the isolated roughness. Therefore, the vertex of the turbulence wedge coincides with the disturbance point. The turbulence wedge centerline is oriented parallel to the vehicle body x-axis. The Mach number dependence of the turbulence wedge is included in the model using a turbulence wedge half-angle parameter. This angle is defined by the curve presented by Fischer [60]. The boundary-layer outside of the turbulence wedge is modeled as completely laminar, while the flow inside the turbulence wedge is modeled as fully turbulent; no transition region is defined. The location and geometry of the turbulence wedge can now be described by four parameters: x position, y position, upper or lower surface, and turbulence wedge half-angle. Figure 3.4 shows an example of the parametrically described asymmetry as applied to an example vehicle geometry from Section 2.1.

(a) Isometric view

(b) Planform view
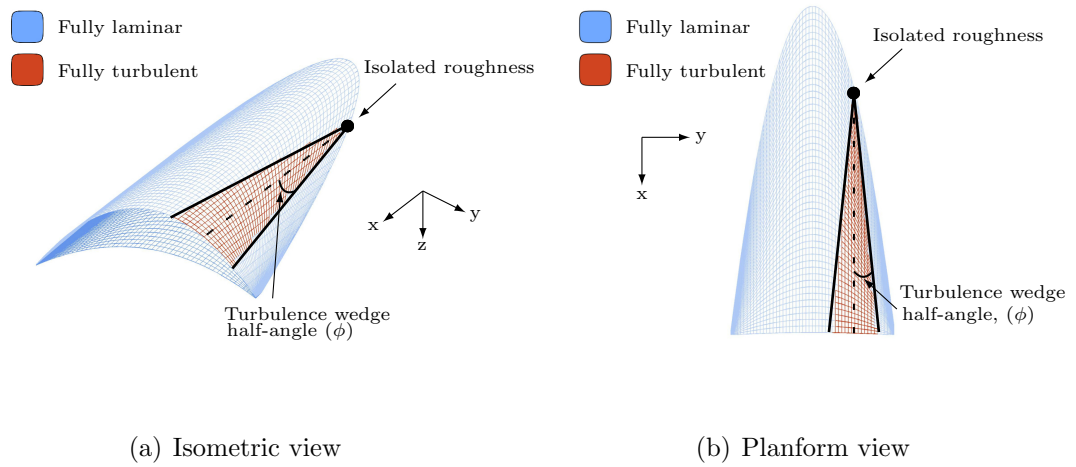
Figure 3.4: Example of an isolated roughness element applied to upper surface of a generic hypersonic vehicle.

Chapter 4:   Optimization Methods, Algorithms, and Definitions

This chapter presents the optimization methods, algorithms, and definitions that were used in this work. All optimization problems formed in this study were solved using genetic algorithms to help ensure global optimality and to remove the requirement of numerically calculating derivative information. The use of genetic algorithms were possible due to the relatively inexpensive nature of the objective functions.

A brief overview of traditional genetic algorithm optimization methods is provided in Section 4.1. This section gives the basics of genetic algorithms as well as the current most established methods and concepts within a multi-objective genetic algorithm context. One of the main contributions in this work is the formulation of a novel robust optimization method. This work provides comparisons between the performance of the proposed method to common robust optimization techniques found in the literature. A detailed discussion on these robust optimization methods is provided in Section 4.2. To illustrate the use of the proposed robust multi-objective method, an illustrated example is provided in Section 4.3. In particular, Section 4.4 focused on analyzing the changes in convergence and accuracy of the method with changes in the genetic algorithm initial conditions and data handling settings.

4.1 Traditional Optimization Methods

4.1.1 Genetic Algorithms

This section serves as a cursory introduction into genetic algorithms. It will provide the basic definitions of the terms used in this study as well as a top level explanation into the process of solving an optimization problem using a standard genetic algorithm. An in-depth discussion on the history, theory, and use of genetic algorithms is available in a book by Mitchell [92].

The theory behind genetic algorithms stems from the biological process of evolution. In nature, as a population of a particular species reproduces and survives from generation to generation, the species evolves. Evolution is the mechanism for which changes and improvements are made based on which particular traits generate "fit" individuals who can survive. In other words, it is a game of "survival of the fittest". This basic idea is applied to optimization problems by starting with a set of possible solutions. Each solution is encoded into a sequence of genes (hence the name *genetic* algorithms), where they compete by being measured against the objective function of the optimization problem. These individuals are then ranked by their level of optimality, reproduce and mutate to form a second generation of solutions. The theory is that as the generations progress, the new solutions will become better and better over time. To help understand the genetic algorithm process and the discussions presented in this study, some of the basic terms are listed below. These terms were adapted from Starkey [87]:

- Population: A group of potential solutions.

- Generation: A particular time or iteration in the process of the algorithm.

- Encoding: The method in which real numbers are converted into binary.

- Chromosome: The compilation of parameters for a potential solution (i.e. the encoded version of the design vector).

- Gene: The building blocks of a chromosome (i.e. the encoded version of one design variable in the design vector).

- Objective Function (or Fitness Function): A performance indicator, taken as the function to be maximized or minimized in the optimization problem. The value is often called its fitness.

- Reproduction: The process in which a new generation is created.

- Selection: The procedure by which survivors are selected to reproduce and populate the next generation.

- Parents: Survivors of the selection process who may reproduce.

- Offspring/Children: The resulting designs from mating pairs of parents.

- Mating: The mechanism through which two parent chromosomes can produce offspring by the exchange of information.

- Crossover: The actual exchange of information between survivors.

- Mutation: A random process whereby a chromosome undergoes a small change (such as a flipping of a binary bit from 0 to 1 or vice versa).

Now with a better understanding of the terminology used in the field of genetic algorithms, the actual algorithm or process of solving an optimization problem using genetic algorithms can be discussed. Figure 4.1 presents a flowchart illustrating the basic procedures found in genetic algorithms. This process is generally the steps taken and form a base for such algorithms. Many algorithms have made tweaks, updates, and changes to this procedure to make it more accurate, quick, and effective.

The general genetic algorithm optimization process starts with the creation of an initial population of designs. This population can be generated randomly or "intelligently" using statistical methods (e.g., Latin hypercube sampling). Next, each individual in the (initial) population is evaluated using the objective function to quantify its fitness. Then, the convergence criteria is checked. Usually this checks to see if a desired optimum value is met, or if the progression has ceased to improve from one generation to the next. If the population is still the initial population, it is likely that the convergence criteria hasn't been satisfied. If not, then the population follows the mating process.

The mating process includes a variety of steps. First, the individuals in the population are ranked according to their fitness. Then, the numerous pairs of designs, known as parents, are selected. The selection process varies from algorithm to algorithm. Once the parent pairs are decided upon, they follow the crossover
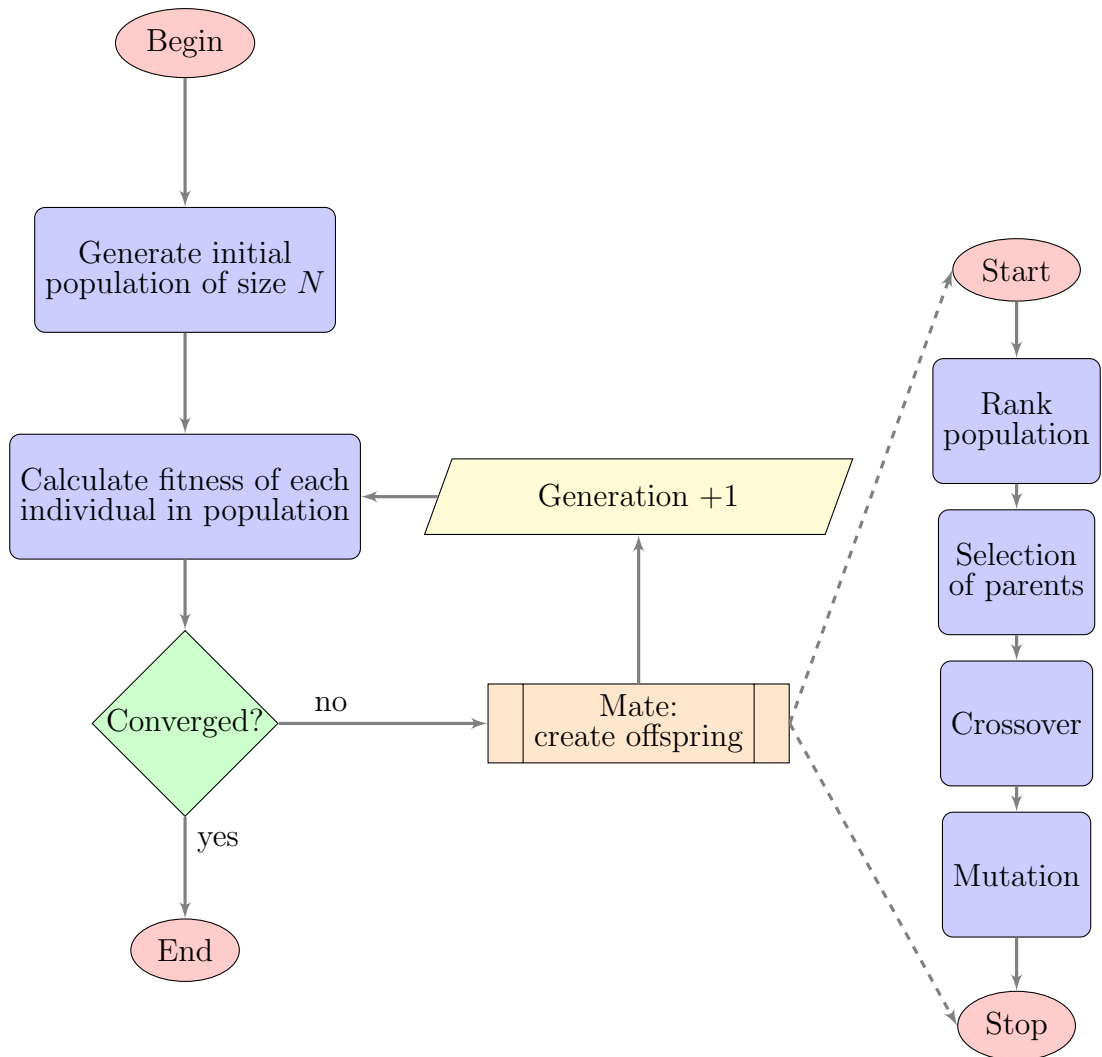
Figure 4.1: Generalized genetic algorithm process.

and mutation processes. The parent design vectors are encoded into binary chromosomes, where the information is split and spliced forming new designs, called offspring. A fraction of these offspring are subject to random binary bit flips in a process called mutation. This completes the reproduction process through mating; the next generation of designs has been formed. This new generation then repeats the process, starting with calculating the fitness of the individuals in the new population. This process is repeated until the convergence criteria are met.

The overarching premise is that the solutions with the best fitness are more likely to survive the selection process and mate to produce the next generation of designs. Over time, the new generations build off the success of the survival of the previous generations, thus "evolving" into the best fit (or optimum) designs. Genetic algorithms are beneficial in many optimization problems due to their ability to solve the problem without the need of gradient information. It is a zero-th order method, meaning only the objective function value is needed. Also, the mutation and crossover processes give more assurance of reaching a global optimum, where gradient-based methods can only guarantee finding a local optimum.

4.1.2 Multi-Objective Genetic Algorithms (MOGA)

This section serves as a brief introduction into the additions necessary to solve multi-objective optimization problems (MOOP) using genetic algorithms. It will provide the basic definitions of the terms used in this study as well a top level explanation into the process of solving an optimization problem using a standard

genetic algorithm discussed in Section 4.1.1. There are many different schemes, additions, methods, and algorithms in the literature aimed at solving multi-objective problems using genetic algorithms. Yet, for the most part, they stick to the overall premise of genetic algorithms. This section will base its discussion off of the NSGA-II algorithm developed by Deb et al. [93]. A detailed discussion on MOGA algorithms and nuances to the processes involved are available in a text written by Deb [94].

To help understand the multi-objective genetic algorithm process and the discussions presented in this study, some of the basic terms used in the field of multi-objective genetic algorithms are listed below. These definitions were adapted from Deb [94]:

- Domination: A design x_1 is said to dominate another design x_2 if both conditions are true:

  1. The design x_1 is no worse than x_2 in all objectives.

  2. The design x_1 is strictly better than x_2 in at least one objective.

  Note, that if x_1 dominates x_2 it is also customary to say that x_1 is non-dominated by x_2.

- Non-dominated set: Among a set of designs P, the non-dominated set of designs P' are those that are not dominated by any member of the set P.

- Global Pareto-optimal set/front: The non-dominated set of the entire feasible search space is the global Pareto-optimal set. Each design within the set is said to be globally Pareto-optimal.

- Local Pareto-optimal set/front: The non-dominated set of a *local* feasible search space is the local Pareto-optimal set. Each design within the set is said to be locally Pareto-optimal.

- Extreme Pareto-optimal points: The points in the Pareto-optimal set which have the best value for each individual objective function (See Figure 6.1 for an example).

- Rank: An attribute of each design, given to quantify its level of Pareto-optimality. Among set of solutions P, the designs in the local Pareto-optimal set are said to have a rank of 1. The designs in the local Pareto-optimal set that exists if all rank 1 designs are removed from P, are said to have a rank of 2. This ranking process is repeated until all designs in P are ranked.

- Diversity: A quality metric for a set of Pareto-optimal designs. The goal is to have a set of designs with maximum diversity. Two designs are diverse in objective space if their Euclidean distance in the objective space is large. For a set of results, this means the desired effect is to have large, even spacing between individuals in the Pareto-optimal set. Maximum diversity helps ensure an equal and comprehensive sampling of the trade-offs in the design space.

- Spread: A quality metric for a set of Pareto-optimal designs. The goal is to maximize spread. The spread is the total Euclidean distance in objective space between the extreme Pareto-optimal points. A maximum spread helps ensure a wide sampling of the trade-offs in the design space.

Now with a better understanding of the terminology used in multi-objective genetic algorithms, the process of solving a multi-objective optimization problem using genetic algorithms can be discussed. The process is illustrated by discussing changes or additions made to the general genetic algorithm procedure given in Figure 4.1. Once again, the process discussed here is generalized and forms a base for MOGAs. Many different algorithms exist which may make tweaks, updates, and changes to this procedure to make it more accurate, quick, and effective.

The first difference in following the generalized genetic algorithm procedure for MOOPs is in the convergence decision phase. Here, different criteria are necessary to see if a set of solutions has sufficiently progressed towards an optimum, rather than just the single most optimum design out of a given population. Many different criteria exist which tie in the metrics such as diversity and spread, among others. The second difference is in the *Rank population* step in the flowchart. Note, do not confuse the word *Rank* in *Rank population* with the definition of rank in the above list of terms. In this step, since there are multiple objectives, ranking each of individuals from best to worst is not straight forward. Most often than not, an aggregation-based scheme is taken to add up the fitness between the objectives, while scaling the values by taking into account a design's rank and diversity. Most of the other procedures within the flowchart remain the same for multi-objective problems.

4.2 Robust Optimization Methods

Consider the following optimization problem:

$$\min_{\vec{x}} \quad f(\vec{x}, p)$$

$$\vec{x} \in \mathbb{X} = \{\vec{x} | \vec{x}_{lb} \leq \vec{x} \leq \vec{x}_{ub}\} \quad, \tag{4.1}$$

where $\vec{x}$ is a vector of design variables and p is an operating condition or an environmental parameter. The problem defined by Equation 4.1 will be referred to as the *original* optimization problem. The original optimization problem can contain different kinds of uncertainties. Uncertainties can exist in the design vectors $(\vec{x})$, the environmental parameter (p), or in the objective function output $(f(\vec{x}, p))$ [4]. This work deals with solving the original problem while accounting for changing environmental parameters or operating conditions due to uncertainty. For a more detailed review on robust optimization and the current state-of-the-art methods, a comprehensive survey is provided by Beyer and Sendhoff [4].

Generally, robust optimization methods incorporate uncertainty by constructing robust counterpart objective functions F to the original objective function f [4]. For example, worst-case scenario methods use a minimax-type formulation in order to construct a robust counterpart function. Aggregation methods form robust counterparts based on the mathematical moments of f over the uncertainty. For the methods described in Section 4.2.1, set $f = F_I$. For Section 4.2.2, set $f = F_{II}$ or F_{III}. For the method in Section 4.2.3, the robust counterpart formulation is multi-objective, so the original objective function f is replaced by a set of M robust counterpart objective functions, $f = [F_{IV_1}, ..., F_{IV_M}]$.

In the present work, a novel multi-objective robust counterpart formulation is proposed, where post-optimality data handling techniques can identify, among a set of Pareto-optimal solutions, the optimal worst-case scenario and expected value solutions for any uncertainty PDF. Solving the robust multi-objective formulation once produces a set of designs, thus giving the designer more information about the design space. The foundations behind a robust regularization-based method, two aggregation-based methods, and the novel multi-objective based robust optimization method are presented and compared in this Sections 4.2.1, 4.2.2, and 4.2.3, respectively. The optimization problem formulation, convergence criteria, and data handling techniques behind the robust multi-objective optimization method are discussed in detail in Section 4.2.3.

The robust multi-objective optimization method is applied to an example optimization problem in Section 4.3. The robust optimum results found using the data handling techniques are compared to the true robust optimum results found analytically. Accuracy and convergence studies were conducted by running multiple simulations with varying method initial conditions and data handling technique settings. The method accuracy was measured by calculating the average error and root-mean-square error between the predicted and analytical robust optimum results.

The robust multi-objective formulation and three commonly used robust method formulations were applied to the ABLT design problem (Section 5.3.2) and the results from each method were compared (Section 6.2.2). It was found that the robust multi-objective optimization method was able to find the same results as the other

robust optimization methods, while providing more insight into the physics behind the design problem by illustrating trade-offs that exist in the design space.

4.2.1 Robust Regularization

This form of accounting for uncertainty is directly analogous to the *minimax approximation* in the field of applied mathematics [69]. This method appears in research spanning multiple disciplines and may be referred to as *minimax, robust regularization* [7], or simply as a *robust counterpart approach* [70].

A robust regularization-based method accounts for uncertainty by formulating a robust counterpart function that represents the worst-case scenario. For a minimization problem, as in Equation 4.1, a robust regularization-based method minimizes the maximum f value over all possible uncertainty in parameter p. The robust counterpart function is defined as the following:

$$F_I\left(\vec{x}\right) = \sup_{p \in \mathbb{P}} f\left(\vec{x}, p\right) \; , \tag{4.2}$$

where $\mathbb{P}$ is the full range of possible operating conditions due to the uncertainty in parameter p. The set $\mathbb{P}$ is defined by the upper and lower bounds, p_{ub} and p_{lb} respectively:

$$p \in \mathbb{P} = \{p | p_{lb} \leq p \leq p_{ub}\} \; . \tag{4.3}$$

Equation 4.3 defines the parameter domain for nominal value of p plus any possible associated uncertainty. Given this definition, the robust regularization technique is nominally used when uncertainty is modeled *deterministically*. Optimization problems where the uncertainty is modeled *probabilistically*, probability measures

describing the likelihood for a particular value of p in that domain to occur are provided [4]. Probabilistically modeled uncertainty problems can also be solved with this method, as long as an upper and lower bound on p can be defined. Inserting Equation 4.2 and 4.3 into the original optimization problem (Equation 4.1) forms the robust optimization problem defined by using a robust regularization-based method:

$$\min_{\vec{x}} \quad \sup_{p} f\left(\vec{x}, p\right)$$

$$\vec{x} \in \mathbb{X} = \{\vec{x} | \vec{x}_{lb} \leq \vec{x} \leq \vec{x}_{ub}\}$$
$$p \in \mathbb{P} = \{p | p_{lb} \leq p \leq p_{ub}\} .$$

(4.4)

4.2.2 Aggregation Approach

The robust regularization approach is considered as a worst-case scenario and may be too conservative for some applications. In such applications, a probabilistic aggregation approach to forming a robust counterpart function is often used. The most common technique is to use an approximation of the conditional expectation of f [5, 6, 8, 9, 71–75]. The simplest way of calculating the expected value of the original objective function for a particular distribution of uncertainty is through explicit averaging [6,8,9]. Given a nominal value p and some associated uncertainty, the robust counterpart function using explicit averaging is defined by,

$$F_{II}\left(\vec{x}, p\right) = \sum_{i=1}^{n} \frac{1}{n} f\left(\vec{x}, p + \Delta p_i\right) ,$$

(4.5)

where Δp_i is a small perturbation generated from the realization of the probability density function of the uncertainty in the nominal value of the environmental parameter p.

In the context of applying evolutionary or genetic algorithms, Tsutsui et al. [72,73] developed a more efficient variation of this method. The method was reduced from taking an average fitness over n samples to adding a stochastic perturbation to each design in the population for a given generation. Much of the previous work using this perturbation method covered uncertainty in the design variables, while a few others [5, 74] have found applications using other types of uncertainties. The current work will apply the perturbation method to uncertainty in the environmental parameter p, thus forming the following robust counterpart function:

$$F_{III}\left(\vec{x}, p\left(t\right)\right) = f\left(\vec{x}, p + \Delta p\left(t\right)\right) \ , \tag{4.6}$$

where t is the generation index and $\Delta p\left(t\right)$ is the random perturbation added to the nominal value of the parameter at generation t. The distribution of the random perturbation should be consistent with the probability density function of the uncertainty associated with the environmental parameter. For an infinite population size, it has been shown that the perturbation method is equivalent to the explicit averaging method [4, 8, 74, 75]. Also note that if $n = 1$ and Δp is chosen randomly per generation, then the explicit averaging method is equivalent to the perturbation method (i.e., Equation 4.5 reduces to Equation 4.6).

4.2.3   Novel Multi-Objective Approach

The explicit averaging and perturbation methods described in Section 4.2.2 form an optimization problem aimed at minimizing the expected value of the original objective function over the uncertainty in the environmental parameter. Optimizing

the expected value may lead to a design with a large variance; this is not always desirable [4]. The current state-of-the-art robust optimization methods begin to address this problem by forming a multi-objective problem using the variance and expected value as conflicting objective functions [4, 9, 74]. This is a beginning step to providing the designer with more insight into the nature of the robust design space. Yet, these methods are still limited to one particular uncertainty PDF for one nominal value.

The current work developed a novel robust multi-objective optimization formulation and method which allows for post-optimality data handling techniques to find robust optimum designs that follow the worst-case scenario and best mean fitness approaches of robust regularization and explicit averaging. The method has the ability to post-optimally pick designs that are most robust for any uncertainty PDF and for various nominal values or the uncertain parameter. Therefore, many types of results can be identified and analyzed by solving only one multi-objective optimization problem.

The robust multi-objective formulation should be solved using a multi-objective optimization solver, algorithm, or method which is most appropriate for the applied application. For example, if the objective function in the original optimization problem (Equation 4.1) is expensive, a gradient-based method using meta-models or surrogates may be most appropriate. If the objective function contains many local minima or maxima, and the objective function is relatively inexpensive, a genetic algorithm-based solver would be more appropriate. If the expected value integral is inexpensive and accurate to approximate using Monte Carlo integration, it may be

most efficient to couple the aggregation technique with a gradient-based method. Keep in mind the pros/cons of the methods reviewed in Section 1.4.3.1 should be consulted to evaluate which optimization formulation and solver (gradient-based with explicit averaging, perturbation-based with genetic algorithms, meta-models, etc.) would be best.

4.2.3.1 Robust MOOP Formulation

For the original optimization problem in Equation 4.1, the robust multi-objective optimization method forms a set of robust counterpart functions given by,

$$
\min_{\vec{x}} \quad F_m\left(\vec{x}\right) = \mathrm{E}\left[f|\vec{x}, p_m\right] \quad m = 1, 2, \ldots, M
$$

$$
\begin{aligned}
&\vec{x} \in \mathbb{X} \\
&\mathbb{X} = \{\vec{x} | \vec{x}_{lb} \le \vec{x} \le \vec{x}_{ub}\} \\
&(p_m + \delta_m) \in \mathbb{P}_m \\
&\delta_m \sim \mathcal{U}\left(\delta_{lb_m}, \delta_{ub_m}\right) \\
&\mathbb{P} = \bigcup_{m=1}^{M} \mathbb{P}_m \ ,
\end{aligned} \tag{4.7}
$$

where $\mathbb{P}$ is the full range of possible operating conditions due to the uncertainty in parameter p. The set $\mathbb{P}$ is defined by the upper and lower bounds, p_{ub} and p_{lb} respectively:

$$
p \in \mathbb{P} = \{p | p_{lb} \le p \le p_{ub}\} \ . \tag{4.8}
$$

The method assigns each of the M objective functions with the task of minimizing the expected value of f over an uncertainty subset $\mathbb{P}_m$. Each subset has a defined nominal value p_m and associated uncertainty δ_m, which is sampled uniformly, such that $(p_m + \delta_m)$ always exists within $\mathbb{P}_m$. Note that this removes the functional

dependence on the nominal value p_m, thus F_m is solely a function of $\vec{x}$. The number of parameter uncertainty subsets, M, and the size of each subset $\mathbb{P}_m$ is chosen by the designer. Once this multi-objective optimization problem is solved, post-optimality data handling equations can be used to predict different types of robust optimum designs.

As mentioned in the introduction to this chapter, Equation 4.7 can be solved using any multi-objective optimization method (direct search methods, surrogate assisted methods, genetic algorithms, gradient-based methods, etc.). From this point on, all investigations and applications of the novel robust MOOP formulation and data handling method in this work are carried out from a genetic algorithm perspective. In particular, the perturbation approach by Tsutsui [72, 73] is used to handle the expected value operators, $\mathrm{E}\left[f|\vec{x}, p_m\right]$, in Equation 4.7. If another method is taken to solve the MOOP, use the data handling analysis in Section 4.2.3.2 starting with Equation 4.11, replacing $\langle F_{IV_m}(\vec{x})\rangle_h$ with $F_m(\vec{x})$ when using the post-optimality equations (Equations 4.11, 4.12, 4.13, 4.14, and 4.15).

The robust MOGA equivalent of Equation 4.7, using the perturbation method, is given by,

$$\min_{\vec{x}} \quad F_{IV_m}\left(\vec{x}, \check{p}_m\left(t\right)\right) = f\left(\vec{x}, \check{p}_m\left(t\right)\right) \quad m = 1, 2, \ldots, M$$

$$\begin{aligned}
&\vec{x} \in \mathbb{X} \\
&\mathbb{X} = \{\vec{x}|\vec{x}_{lb} \leq \vec{x} \leq \vec{x}_{ub}\} \\
&\check{p}_m\left(t\right) \sim \mathcal{U}\left(p_{lb_m}, p_{ub_m}\right) \\
&\mathbb{P}_m = \{p|p_{lb_m} \leq p \leq p_{ub_m}\} \\
&\mathbb{P} = \bigcup_{m=1}^{M} \mathbb{P}_m .
\end{aligned} \tag{4.9}$$

Parameter t is the genetic algorithm generation index, and $\breve{p}_m(t)$ is a random parameter value chosen over a uniform distribution of points belonging to $\mathbb{P}_m$. The number of parameter uncertainty subsets, M, and the size of each subset $\mathbb{P}_m$ is chosen by the designer. The versatility in predicting results for different probability distributions increases with M. This will become apparent when discussing the post-optimality data handling techniques. Yet, as M increases, multi-objective genetic algorithms have a more difficult time advancing the Pareto-optimal front and producing diverse results [94, 95]. Once again this formulation can viewed as a multi-objective implementation of the perturbation method by Tsutsui et al. [72,73], as applied to parameter uncertainties.

4.2.3.2   Convergence Criteria and Data Handling

The robust multi-objective optimization method presented here utilizes a perturbation-based approach. The robust counterpart environmental parameter $\breve{p}_m(t)$ changes from generation to generation, rendering generation history plots based on objective function values noisy and difficult to interpret. Therefore, this method cannot use convergence criteria based on information from a single generation. Convergence criteria of this type are typical in non-perturbation-based optimization [94,96]. Instead, the Pareto-optimal solution set and the convergence status of the method at a given generation needs to be an average over previous generations.

At any generation index t, there exists a *local* set of Pareto-optimal solutions. These points are the non-dominated designs in the particular objective space defined

by the parameter set $[\check{p}_1(t), ..., \check{p}_M(t)]$. Qualitatively, the set of *true* Pareto-optimal solutions, $\bar{x}$, are the ones that are most common for all possible sets of $\check{p}$. An approximated set of true Pareto-optimal solutions, $\hat{x}$, at generation t is calculated by the following steps:

1. For each generation from 1 to t, identify the local Pareto-optimal solutions and add them to a running archive.

2. Generate a v-dimensional histogram with bins containing counts of the design vectors in the archive, where v is the length of $\vec{x}$.

3. Isolate the bins with bin counts greater than the mean bin count over all bins. The mean values of $x_1, ..., x_v$, in each of these v-dimensional bins, form a design.

4. Collectively, the designs from Step 3 form the approximation of the set of true Pareto-optimal solutions, $\hat{x}_t$.

As the generations progress, changes in the set of designs $\hat{x}_t$ should become less frequent and the set should eventually converge. No rigorous proof of convergence has been performed, but convergence towards a particular $\hat{x}$ was demonstrated for the example optimization problem in Section 4.3 and the ABLT optimization problem results in Section 6.2.2.4. Accuracy and convergence trends corresponding to this method are investigated in Section 4.4. Since $\hat{x}_t$ is an approximation, the design vectors in this set are not guaranteed to be non-dominated. Therefore, the final step after convergence is to filter out all the dominated points to ensure that the final

set is completely Pareto-optimal.

Changes in $\hat{x}_t$ from one generation to the next were measured as the total number of unique designs that were added to or subtracted from $\hat{x}$ from one generation to the next. This metric, represented as a percent change with respect to the average size of $\hat{x}$ over generation t and $t - 1$, is referred to as $\Delta PM(t)$. For example, given a single design variable $(v = 1)$, if the approximated set of true Pareto-optimal solutions at generation 100 is $\hat{x}_{100} = \{1, 2, 3, 4\}$ and at generation 101 is $\hat{x}_{101} = \{1, 2, 3, 4, 5, 6\}$, then the value of $\Delta PM(101) = 40\%$. Written in set notation, $\Delta PM(t)$ is defined by,

$$\Delta PM(t) = 100 * \frac{|\hat{x}_t \bigtriangleup \hat{x}_{t-1}|}{\frac{1}{2}(|\hat{x}_t| + |\hat{x}_{t-1}|)} . \tag{4.10}$$

The results from the perturbation-based robust multi-objective formulation are in the form of a generation-dependent Pareto-optimal hypersurface in objective function space. The Pareto-optimal solutions most common in a large generation by generation archival set are the results of interest.

Once an approximation to the true set of Pareto-optimal solutions is identified, post-optimality data handling techniques can be employed to identify different types of "preferred" robust optimal designs [94]. An optimal worst-case scenario solution is found from the set of Pareto-optimal solutions using the following weighted minimax formula:

$$\vec{x}_{wcs} = \min_{\vec{x} \in \hat{x}_t} \left(\max_{m=1}^{M} w_m \langle F_{IV_m}(\vec{x}) \rangle_h \right) , \tag{4.11}$$

where, $\langle F_{IV_m}(\vec{x}) \rangle_h$ is the mean m-th objective function value over h generations (1 to t) for the Pareto-optimal design $\vec{x} \in \hat{x}_t$. The weights w_1 through w_m are defined

by the following:

$$
w_m = \begin{cases} 0, & \text{if} \quad \mathbb{P}_m \subset \mathbb{P}_{wcs} \\ \\ 1, & \text{if} \quad \mathbb{P}_m \not\subset \mathbb{P}_{wcs} \end{cases} ,
\tag{4.12}
$$

$$
\mathbb{P}_{wcs} \subseteq \mathbb{P} ,
$$

where $\mathbb{P}_{wcs}$ is the uncertainty subset over which the worst-case scenario is being analyzed. In other words, the designer may not always want to find the worst-case scenario over the entire uncertainty set $\mathbb{P}$, but yet a subset $\mathbb{P}_{wcs}$.

A minimized expected value solution is found by using a weighted L^1-norm formula defined by,

$$
\vec{x}_{ev} = \min_{\vec{x} \in \hat{x}_t} \left(\sum_{m=1}^{M} w_m |\langle F_{IV_m} (\vec{x}) \rangle_h - z_m^*| \right) ,
\tag{4.13}
$$

where z_m^* is the *ideal* m-th objective function value, equal to the best possible value found over the entire Pareto-optimal set defined by:

$$
z_m^* = \min_{\vec{x} \in \hat{x}_t} \langle F_{IV_m} (\vec{x}) \rangle_h .
\tag{4.14}
$$

The weights w_1 through w_M are set by the nominal parameter value, p, and accompanying perturbation δ (a realization from the uncertainty PDF). Typically, these weights are defined such that they sum to one [94]. The weights can be calculated as follows:

$$
w_m = \frac{\Pr (p + \delta \in \mathbb{P}_m)}{\Pr (p + \delta \in \mathbb{P})} .
\tag{4.15}
$$

For example, consider an optimization problem aimed to minimize the expected value of $f (\vec{x}, p)$ where $p = 0.5$ and the uncertainty in p is assumed to be uniformly distributed about p with a lower and upper bound of $p_{lb} = 0.0$ and $p_{ub} = 1.0$.

Assume the robust MOGA method problem is using five objective functions $(M = 5)$ where the uncertainty is split into equally spaced subsets $\mathbb{P}_m$:

$$\mathbb{P}_1 = \{p | 0.0 \le p < 0.2\} \ ,$$
$$\mathbb{P}_2 = \{p | 0.2 \le p < 0.4\} \ ,$$
$$\mathbb{P}_3 = \{p | 0.4 \le p < 0.6\} \ , \tag{4.16}$$
$$\mathbb{P}_4 = \{p | 0.6 \le p < 0.8\} \ ,$$
$$\mathbb{P}_5 = \{p | 0.8 \le p \le 1.0\} \ .$$

Following Equation 4.15 the calculation of w_m would produce

$$w_1 = w_2 = w_3 = w_4 = w_5 = \frac{1}{5} \ . \tag{4.17}$$

Now consider the same problem for uncertainty that follows a truncated normal distribution rather than a uniform distribution. Here p values are sampled from a truncated normally-distributed probability density function with a mean of 0.5, standard deviation of 0.2, and bounded by $p_{lb} = 0.0$ and $p_{ub} = 1.0$. Equation 4.15 would then produce the following weights:

$$\begin{aligned}
w_1 &= 0.0614 \ , \\
w_2 &= 0.2449 \ , \\
w_3 &= 0.3879 \ , \\
w_4 &= 0.2449 \ , \\
w_5 &= 0.0614 \ .
\end{aligned} \tag{4.18}$$

4.3 Illustrative Example

An example optimization problem will be used in this section to illustrate the use of the robust MOGA formulation proposed in Section 4.2.3. An optimization problem with two design variables and one environmental parameter will be used as the *original* problem. The original optimization problem formulation is presented in Section 4.3.1. Worst-case scenario robust optimum solutions and minimum expected value robust optimum solutions were derived analytically in Section 4.3.2. The multi-objective robust counterpart optimization problem was then formed and solved using genetic algorithms in Section 4.3.3. The optimization results and the overall effectiveness of the proposed method was analyzed by comparisons with the analytical solutions. The optimization problem formulation and set of results in Section 4.3.3 will be referred to as the baseline simulation.

4.3.1 Original Optimization Problem

Consider the following original optimization problem:

$$\min_{\vec{x}} \quad f_{i.e.}\left(\vec{x}, p\right) = 1 - \left(0.4 + \frac{1}{2 + x_1}\right) \exp\left(-\frac{\left(p - x_2\right)^2}{2 x_1{}^2}\right)$$

$$\vec{x} \in \mathbb{X}$$

$$\mathbb{X} = \left\{(x_1, x_2) \,|\, x_1 \in [0.1, 1], x_2 \in [0, 1]\right\},$$

(4.19)

where the environmental parameter p ranges from zero to one.

Figures 4.2 and 4.3 present two-dimensional slices of the design space defined by Equation 4.19. The objective function value $f_{i.e.}$ as a function of p for increasing values of x_1 and a constant x_2 forms inverted bell shaped curves with increasing
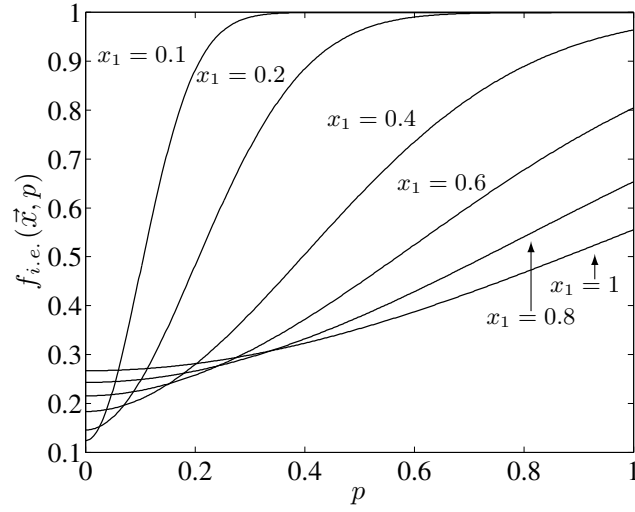
(a)
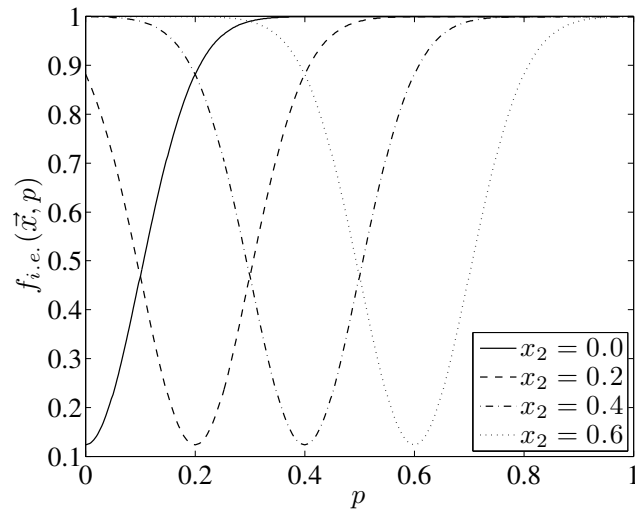
(b)

Figure 4.2: $f_{i.e.}$ curves as a function of p and $\vec{x}$.
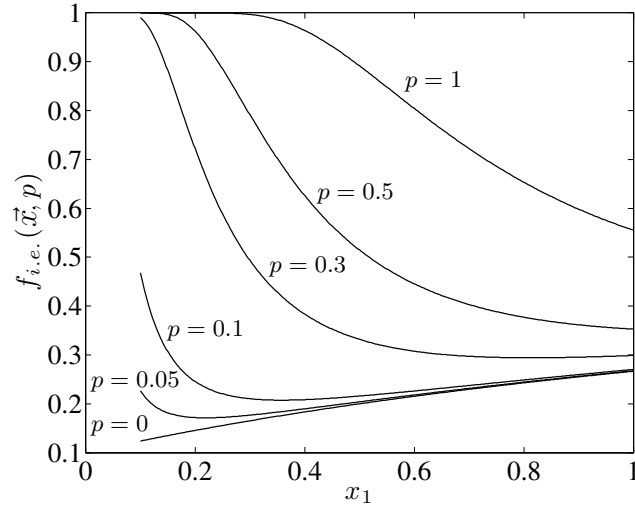
(a)
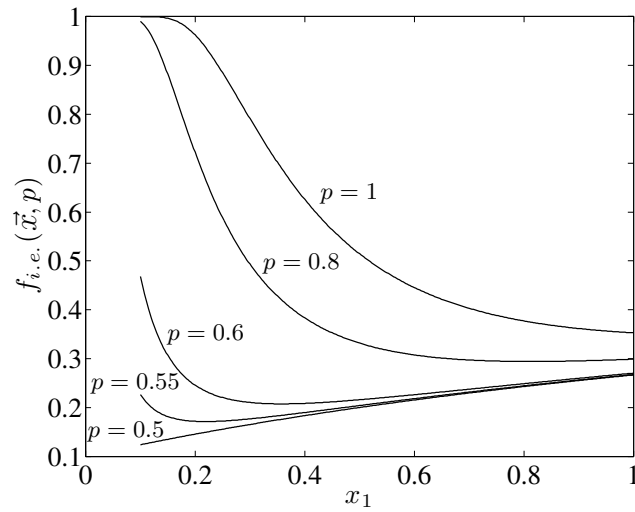
(b)

Figure 4.3: $f_{i.e.}$ curves as a function of p and $\vec{x}$.

width (Figure 4.2(a), where $x_2 = 0.0$). As x_1 increases from 0.1 to 1.0, the width of the curve increases and the minimum value of $f_{i.e.}$ increases slightly, thus flattening and raising the curve. The values of $f_{i.e.}$ as a function of p and x_2 for a constant x_1 form an inverted bell shape of constant width, with x_2 defining the center of the bell. Contours of $f_{i.e.}$ vs. p for varying values of x_2 with $x_1 = 0.1$ are plotted in Figure 4.2(b). The objective function when plotted as a function of x_1 for given values of p and a constant x_2 is presented in Figures 4.3(a) and 4.3(b), where $x_2 = 0.0$ and $x_2 = 0.5$, respectively. This particular objective function was chosen due its smooth monotonic nature and its ability to render a range of robust optimum solutions spanning the design space.

4.3.2 Analytical Robust Optimum Solutions

4.3.2.1 Optimal Expected Value

A robust counterpart approach to Equation 4.19, where the goal is to minimize the expected value of $f_{i.e.}$, forms the following robust optimization problem:

$$\min_{\vec{x} \in \mathbb{X}} \quad \mathrm{E}\left[f_{i.e.} | \vec{x}, p\right] . \tag{4.20}$$

Inserting $f_{i.e.}$ from Equation 4.19, $\mathrm{E}\left[f_{i.e.} | \vec{x}, p\right]$ becomes

$$\int_{-\infty}^{\infty} \left[-\left(0.4 + \frac{1}{x_1 + 2}\right) \exp\left(-\frac{(p + \delta - x_2)^2}{2 x_1{}^2}\right) + 1 \right] \phi\left(\delta\right) d\delta , \tag{4.21}$$

where δ is a perturbation away from a nominal value, p, due to uncertainty and $\phi\left(\delta\right)$ is the accompanying probability density function of the uncertainty. After applying the assumption that for any value of p the perturbation δ is a realization from a

zero mean normally distributed PDF with a variance of σ^2,

$$\phi\left(\delta\right) = \mathcal{N}\left(0, \sigma^2\right) , \tag{4.22}$$

the expression in Equation 4.21 simplifies to

$$-\frac{0.4 + \frac{1}{x_1+2}}{\sqrt{\frac{\sigma^2}{x_1^2}+1}} \exp\left(\frac{-\left(p-x_2\right)^2}{2\left(\sigma^2+x_1^2\right)}\right) + 1 . \tag{4.23}$$

The global robust optimum design $\vec{x}^*$ that minimizes Equation 4.23 with respect to

$\vec{x}$ is

$$\vec{x}^* = \left(x_1^*, x_2^*\right) ,$$

$$\sigma^2 = \frac{5x_1^{*3}}{2x_1^{*2} + 8x_1^* + 18} , \tag{4.24}$$

$$x_2^* = p .$$

4.3.2.2   Optimal Worst-Case Scenario

Using a robust regularization approach, where the uncertainty in p is defined

over some uniformly distributed neighborhood $\epsilon \in [a, b]$, the robust optimum coun-

terpart to Equation 4.19 would be,

$$\min_{\vec{x} \in \mathbb{X}} \ \sup_{\epsilon \in [a,b]} \ f_{i.e.}\left(\vec{x}, \epsilon\right) , \tag{4.25}$$

where $0.0 \leq a \leq b$ and $b \leq 1.0$. Solving the inner optimization problem, i.e. finding

the supremum, gives the following:

$$\sup_{\epsilon \in [a,b]} \ f_{i.e.}\left(\vec{x}, \epsilon\right) = \begin{cases} A, & \text{if } B \text{ or } C \\[2ex] D, & \text{if } E \text{ or } F \end{cases} , \tag{4.26}$$

where,

$$A = -\left(0.4 + \frac{1}{x_1 + 2}\right) \exp\left(-\frac{(b - x_2)^2}{2x_1{}^2}\right) + 1 \ ,$$

$$B = x_2 \le a \ ,$$

$$C = a \le x_2 \le b \text{ and } x_2 \le \left(\frac{b - a}{a} + a\right) \ ,$$

$$D = -\left(0.4 + \frac{1}{x_1 + 2}\right) \exp\left(-\frac{(a - x_2)^2}{2x_1{}^2}\right) + 1 \ ,$$

$$E = x_2 \ge b \ ,$$

$$F = a \le x_2 \le b \text{ and } x_2 \ge \left(\frac{b - a}{a} + a\right) \ . \tag{4.27}$$

The global robust optimum design $\vec{x}^*$ that minimizes Equation 4.26 with respect to $\vec{x}$ (i.e. solving the outer optimization problem in Equation 4.25) is

$$\vec{x}^* = (x_1^*, x_2^*) \ ,$$

$$\left(\tfrac{b-a}{2}\right)^2 = \frac{5x_1^{*3}}{2x_1^{*2} + 13x_1^* + 18} \ , \tag{4.28}$$

$$x_2^* = \left(\frac{b}{a} + a - 1\right) \ .$$

4.3.3 Robust MOGA Formulation & Data Handling Solutions: Baseline Simulation

The first step in forming the robust optimization problem using the proposed multi-objective method is to choose the subsets $\mathbb{P}_m$ for the problem. For this example, lower and upper bounds on the possible range of values of p will be 0.0 and 1.0, respectively. Therefore, using Equation 4.8, $\mathbb{P} = \{p | 0.0 \le p \le 1.0\}$. The full

uncertainty set was split into the following five subsets:

$$\mathbb{P}_1 = \{p|0.0 \leq p \leq 0.2\},$$

$$\mathbb{P}_2 = \{p|0.2 \leq p \leq 0.4\},$$

$$\mathbb{P}_3 = \{p|0.4 \leq p \leq 0.6\}, \quad (4.29)$$

$$\mathbb{P}_4 = \{p|0.6 \leq p \leq 0.8\},$$

$$\mathbb{P}_5 = \{p|0.8 \leq p \leq 1.0\}.$$

These subsets were chosen in order to equally sample the uncertainty space and balance the trade-off between accuracy of the post-optimality handling predictions and the MOGA problem complexity (as the number of subsets increases the problem becomes more difficult to solve [94, 95]). Following the method outlined by Equation 4.9 and given the original optimization problem in Equation 4.19, the robust multi-objective optimization method forms the following MOGA-based optimization problem:

$$\min_{\vec{x}} \quad F_{IV_m}\left(\vec{x}, \breve{p}_m\left(t\right)\right) = f_{i.e.}\left(\vec{x}, \breve{p}_m\left(t\right)\right) \quad m = 1, 2, 3, 4, 5$$

$$\vec{x} \in \mathbb{X}$$
$$\mathbb{X} = \{(x_1, x_2)\,|x_1 \in [0.1, 1]\,, x_2 \in [0, 1]\}$$
$$\breve{p}_1\left(t\right) \sim \mathcal{U}\left(0.0, 0.2\right) \quad (4.30)$$
$$\breve{p}_2\left(t\right) \sim \mathcal{U}\left(0.2, 0.4\right)$$
$$\breve{p}_3\left(t\right) \sim \mathcal{U}\left(0.4, 0.6\right)$$
$$\breve{p}_4\left(t\right) \sim \mathcal{U}\left(0.6, 0.8\right)$$
$$\breve{p}_5\left(t\right) \sim \mathcal{U}\left(0.8, 1.0\right).$$

A qualitative way of reading the optimization problem outlined in Equation 4.30 is as follows:

- Objective 1 $\left(\min\limits_{\vec{x}} F_{IV_1}\right)$ will find the value of $\vec{x}$ such that the mean value of $f_{i.e.}$ over $p = [0.0, 0.2]$ is minimized.

- Objective 2 ($\min\limits_{\vec{x}} F_{IV_2}$) will find the value of $\vec{x}$ such that the mean value of $f_{i.e.}$ over $p = [0.2, 0.4]$ is minimized.

- Objective 3 ($\min\limits_{\vec{x}} F_{IV_3}$) will find the value of $\vec{x}$ such that the mean value of $f_{i.e.}$ over $p = [0.4, 0.6]$ is minimized.

- Objective 4 ($\min\limits_{\vec{x}} F_{IV_4}$) will find the value of $\vec{x}$ such that the mean value of $f_{i.e.}$ over $p = [0.6, 0.8]$ is minimized.

- Objective 5 ($\min\limits_{\vec{x}} F_{IV_5}$) will find the value of $\vec{x}$ such that the mean value of $f_{i.e.}$ over $p = [0.8, 1.0]$ is minimized.

With the true robust optimum designs known analytically (Section 4.3.2), comparisons can be made to the results predicted by the robust MOGA formulation when solving Equation 4.30 using a MOGA solver and applying the post-optimality data handling techniques. The multi-objective optimization problem was solved using a modified version of the MOGA solver in the MATLAB Genetic Algorithm and Direct Search toolbox (GADS). The multi-objective genetic algorithm solver in the GADS toolbox employs a version of an elitist non-dominated sorting genetic algorithm method, NSGA-II [93]. The genetic algorithm options and settings used to solve Equation 4.30 are listed in Table 4.1.

The simulation was run for 500 generations in order to illustrate the generation history trends of the convergence metric ΔPM. Figure 4.4 plots the moving average of ΔPM over 10 generations as a function of current generation number. The value of the moving average of ΔPM at generation 1 is about 27. As generations progress, the moving average value of ΔPM decreases rapidly until about

Table 4.1: MOGA options used for solving Equation 4.30.

Genetic algorithm option	Setting
Population size	600
Generations	500
Initial population	Random within $\vec{x}_{lb}$ and $\vec{x}_{ub}$
Fitness scaling	Based on the individual's rank in the sorted scores
Selection	Tournament selection
Crossover	Randomized
Mutation	Gaussian
Crossover fraction	0.8

generation 25. After generation 25, the overall trend continues to decrease slowly until about generation 125. From generation 125 onward, no appreciable decrease is seen. Similar convergence trends were found when the robust multi-objective method was applied to the vehicle design optimization problem in Section 6.2.2.4. This simulation was said to have converged when the moving average of ΔPM over 10 generations is equal to zero. This first occurs at generation 135. Therefore, the approximation to the true Pareto-optimal solution at generation 135 ($\hat{x}_{135}$) will be used in the analysis.

The set of Pareto-optimal solutions at generation 135 contains 337 individuals in the population. The predicted optimal worst-case scenario and expected value solutions can be picked out of the set of 337 solutions using Equations 4.11 and 4.13, respectively. Figure 4.5 and Figure 4.6 compare the analytical optimal expected value designs using Equation 4.24 to the predicted optimal expected value designs using Equation 4.13 for p values spanning from 0.2 to 0.8 in increments of 0.1

(a) Full generation history.

(b) Generation history zoomed in.
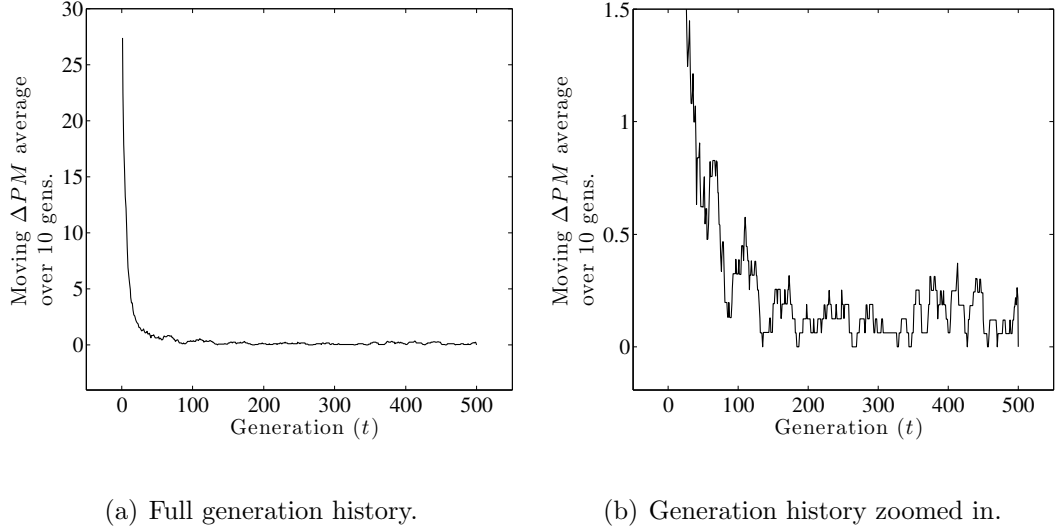
Figure 4.4: Mean ΔPM generation history.

and σ values from 0.02 to 0.2 in increments of 0.02. Errors in predicted x_1^* values over the p-σ combinations reveal particular areas of accuracy and inaccuracy when compared to the analytical values. When $p = 0.3$, 0.5, and 0.7, predicted values of x_1^* were consistently within ± 0.075 of the analytical values for all values of σ. The predictions for $p = 0.2$, 0.4, 0.6, and 0.8, diverged from the analytical values when σ dropped below a value of about 0.15, 0.08, 0.08, and 0.08, respectively. These areas of accuracy and inaccuracy are governed by the calculated weights in Equation 4.15.

When the environmental parameter p is 0.2, 0.4, 0.6, or 0.8, for the subsets given by Equation 4.29, the uncertainty PDF for the lower values of σ renders w_m values that mostly span two adjacent $\mathbb{P}_m$ subsets. Therefore, for σ values less than about 0.1, the weights for the two adjacent subsets $\mathbb{P}_m$ are about equal and Equation 4.13 selects the same solution from the Pareto-optimal set. The solutions thus diverge from the analytical solutions for decreasing σ. As σ becomes greater than about 0.1, the weights w_m become distributed more evenly among the other
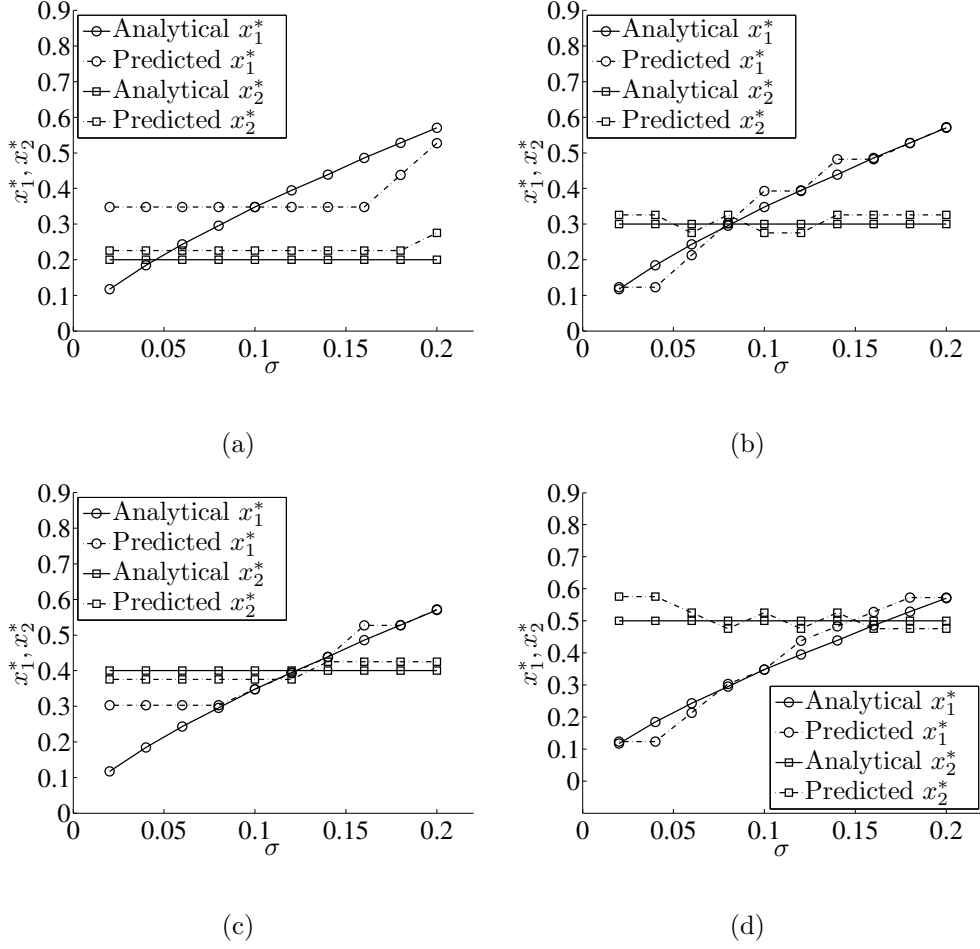
Figure 4.5: Baseline analytical and predicted optimum expected value design vectors for p values of 0.2, 0.3, 0.4, and 0.5, respectively.

three subsets, which in turn enables Equation 4.13 to select different solutions within the Pareto-optimal set.

When the environmental parameter p is 0.3, 0.5, or 0.7, the uncertainty PDF is centered within subset $\mathbb{P}_2$, $\mathbb{P}_3$, and $\mathbb{P}_4$, respectively. This creates w_m values that are more distributed and dynamically changing with σ, even for values lower than about 0.1. For σ less than about 0.04, the uncertainty PDF is mostly contained within a single subset $\mathbb{P}_m$ (w_m is close to unity) and Equation 4.13 selects the same
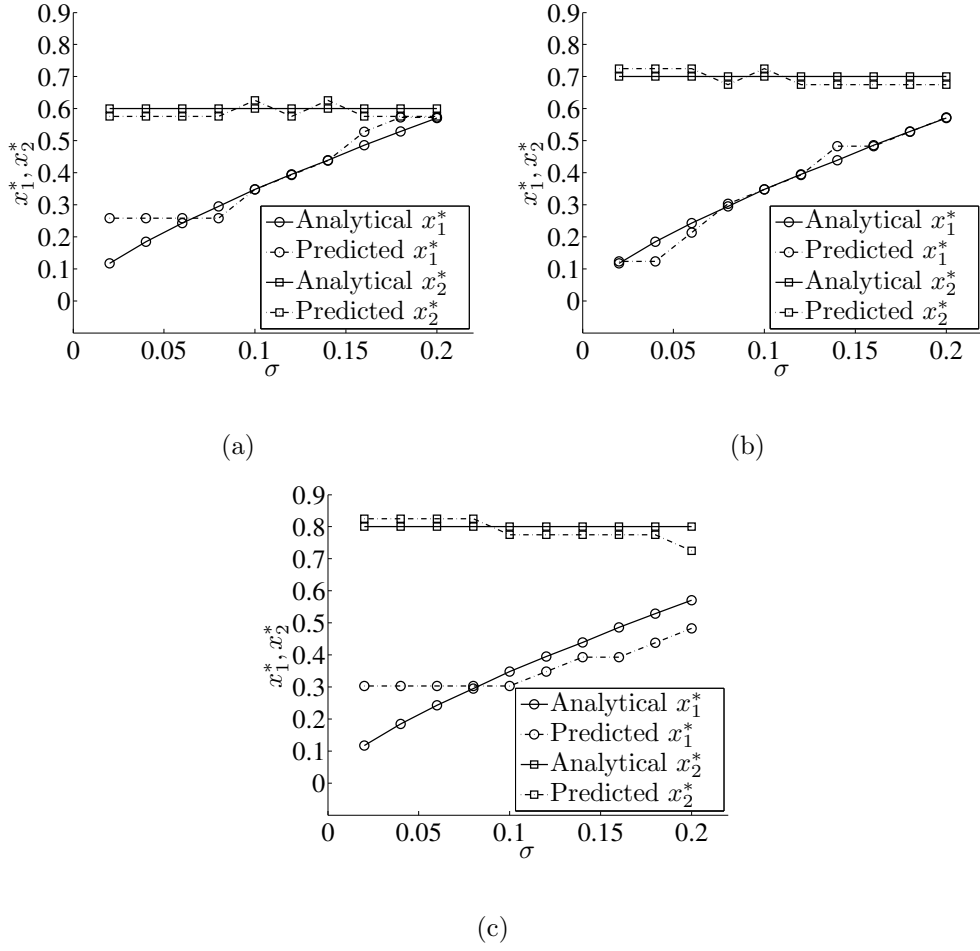
Figure 4.6: Baseline analytical and predicted optimum expected value design vectors for p values of 0.6, 0.7, and 0.8, respectively.

solution from the Pareto-optimal set. Errors in the value of the predicted x_2^* for 66 out of the 70 p-σ combinations were all within ± 0.03 of their respective analytical counterparts. The four other predicted values were within ± 0.08 of the analytical values.

To produce more accurate results, the designer would have to decrease the size of the parameter uncertainty subsets and increase the number subsets. This would produce a more dynamic trade-off in the weighted L^1-norm selection of the

Pareto-optimal designs. This effect is illustrated by the results in Section 4.4.3.

Figure 4.7 compares the analytical optimal worst-case scenario designs using Equation 4.28 to the predicted optimal worst-case scenario designs using Equation 4.11 for fifteen uncertainty neighborhoods defined by,

$$\mathbb{P}_{ab} = \{p | a \leq p \leq b\} . \tag{4.31}$$

The values of a and b for each of the 15 cases are listed in Table 4.2. Figure 4.7 shows that the proposed robust MOGA method with post-optimality data handling is successful in identifying robust optimum designs based on a worst-case scenario for various different neighborhoods of uncertainty. Predicted values of x_1^* and x_2^* follow the same trends as their analytical counterparts. Errors in predicted x_1^* values were all within ± 0.1 except for Cases 12 and 14, where the values were overpredicted by 0.112 and 0.164, respectively. Errors in predicted x_2^* values were all within ± 0.03 except for Cases 1 and 5, where the values were overpredicted by 0.0773 and 0.0747, respectively. Accuracy in the predicted solutions is dependent on the number of subsets M used in the analysis, as well as the number and diversity of the individuals in the Pareto-optimal set.
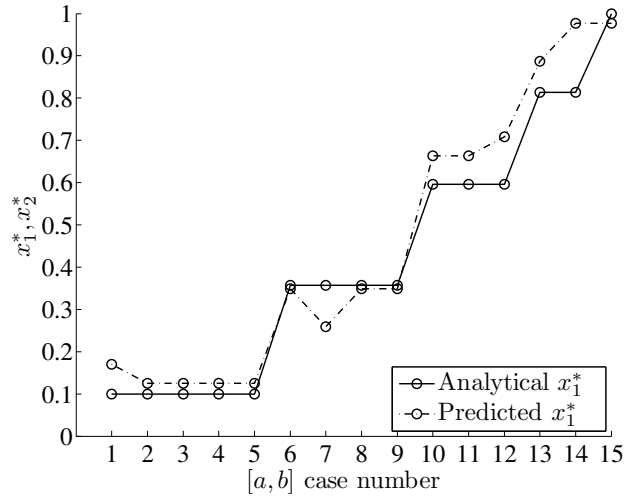
(a)
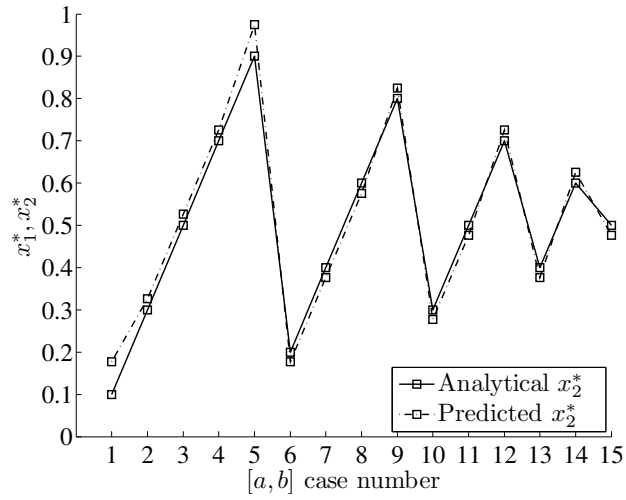
(b)

Figure 4.7: Analytical and predicted optimum worst-case scenario design vectors for various $[a, b]$ values.

Table 4.2: Worst-case scenario comparison settings in Figure 4.7.

Case number	$[a, b]$ values
1	$[0.0, 0.2]$
2	$[0.2, 0.4]$
3	$[0.4, 0.6]$
4	$[0.6, 0.8]$
5	$[0.8, 1.0]$
6	$[0.0, 0.4]$
7	$[0.2, 0.6]$
8	$[0.4, 0.8]$
9	$[0.6, 1.0]$
10	$[0.0, 0.6]$
11	$[0.2, 0.8]$
12	$[0.4, 1.0]$
13	$[0.0, 0.8]$
14	$[0.2, 1.0]$
15	$[0.0, 1.0]$

4.4   Accuracy and Convergence Tests

Multiple simulations were run with varying method initial conditions and data handling technique settings in order to test the accuracy and convergence characteristics of the proposed robust MOGA method. Each simulation perturbs one of three initial conditions and settings from the baseline simulation. The three initial conditions and settings which were subject to change are the following:

- The initial population size used to solve the robust optimization problem with the NSGA-II genetic algorithm

- The number of histogram bins used in Step 2 of the data handling process outlined in Section 4.2.3.2

- The number of objective functions and uncertainty subsets (M in Equation 4.9) used in the multi-objective optimization problem formulation

The optimum solutions predicted by each simulation were judged using three criteria: accuracy, quality, and speed. These criteria quantitatively describe the results and help compare the effects of changing the simulation settings. The definitions of accuracy, quality, and speed are listed below.

- Accuracy: The accuracy of a predicted solution set is measured by the mean absolute error and root-mean-square error of the predicted optimum solutions when compared to the analytical optimum solutions. All errors are given in percentage of the design variable range.

- Quality: The quality of the predicted solution set is measured by the number of Pareto-optimal points in the final Pareto-optimal front.

- Speed: The speed of the simulation is measured by how many generations were needed to progress the simulation to a particular level of convergence.

All the simulations were run with the same convergence criterion as the baseline case: the simulation has converged when the moving average value of ΔPM over 10 generations is equal to zero.

Table 4.3 is the test matrix which contains a list of the simulations that were run and all of the associated input settings. Simulations P1 through P8 vary the

size of the initial population used in the genetic algorithm, while keeping the number of histogram bins and uncertainty subsets equal to that used in the baseline simulation. Simulations B1 through B4 vary the number of histogram bins used in the data handling procedure, while keeping the initial population size and number of uncertainty subsets equal to that of the baseline. Simulations S1 and S2 vary the number of uncertainty subsets in the optimization problem formulation while keeping the other two parameters the same as the baseline. Accuracy, quality, and speed comparisons for these simulations are given in Sections 4.4.1, 4.4.2, and 4.4.3.

Table 4.3: Accuracy and convergence input settings test matrix.

Simulation	Initial population size	Number of histogram bins	Number of uncertainty subsets (M in Equation 4.9)
Baseline	600	20	5
P1	1200	20	5
P2	300	20	5
P3	150	20	5
P4	75	20	5
P5	37	20	5
P6	18	20	5
P7	9	20	5
P8	5	20	5
B1	600	60	5
B2	600	40	5
B3	600	10	5
B4	600	5	5
S1	600	20	8
S2	600	20	3

4.4.1 Effects of Changes in Initial Population Size

Nine simulations (P1-P8 and Baseline) were run to compare how changes in the size of the initial population affect the speed, quality, and accuracy of the predicted robust optimum design vectors. Graphs illustrating these effects are provided in Figure 4.8.

Figure 4.8(a) shows that, for a population size between 37 and 1200, a simulation with a larger population size converges after a smaller number of generations. The generation number at convergence is reduced from 406 to 156 over this range. For the three data points with a population size less than 37, the generation number at convergence falls off quickly from 406 to 84. This trend exists due to the influence of the population size on the NSGA-II algorithm effectiveness. As the population increases, a smaller fraction of points in the population are non-dominated. This gives the algorithm a more diverse set of designs to rank and sort using an elitism scheme. More diverse designs result in a more effective genetic algorithm and quicker convergence. If the population is below a certain threshold, most if not all the points in the population are non-dominated. When this happens, there is no fitness advantage to any of the solutions. Therefore, the mutation and crossover operators are solely responsible for creating solutions in a better Pareto-optimal front, allowing the algorithm to continue to make progress [94]. Consequently, changes in the set of Pareto-optimal points are sparse. This results in premature convergence when using the ΔPM convergence criterion. This concept is discussed in more detail in Section 8.8.2 in Deb [94].

Figure 4.8(b) shows that increasing the initial population size from 5 to about 37 will increase the number of Pareto-optimal points in the final set of optimum designs from 53 to 283. This drastic change in quality is likely to be a consequence of the premature convergence found in the analysis of the population effects on speed. This trend quickly levels off for a population size between 37 and 1200 individuals (note the x-axis is shown in log scale), where the number of Pareto-optimal points grows from 283 to 337. This relatively mild increase is attributed to the fact that a larger population aids in the identification of Pareto-optimal points by providing a better probability that any particular Pareto-optimal design will be involved in the optimization process. A smaller population has a higher likelihood that a non-dominated candidate will be skipped over due to limited sampling. This mild but steady trend from 283 to 337 Pareto-optimal points looks to be asymptotically progressing towards a theoretical maximum number of Pareto-optimal points possible for that optimization problem. This theoretical maximum number is found to be determined by the number of histogram bins.

Figure 4.8(c) shows that with increasing population size, the mean error and RMS error of the predicted designs decrease. Note that the x-axis is shown in log scale, highlighting that the accuracy metrics quickly improve from a population size of 5 to about 37. This again is most likely attributed to premature convergence. For a population size of 37 to 1200, improvement in accuracy is gradual, where the mean error reduces from 9.7% to 8% and the RMS error reduces from 7.2% to 6%. This reduction is caused by an increasing number of samples present in each bin when performing Step 3 in Section 4.2.3.2 and the averaging operators in Equations

4.11 and 4.13. Averages over a larger sample size produce more accurate results with less dispersion.

4.4.2 Effects of Changes in Number of Histogram Bins

Five total simulations (B1-B4 and Baseline) were run to compare how changes in the number of histogram bins affect the speed, quality, and accuracy of the predicted robust optimum design vectors. Graphs illustrating these changes are provided in Figure 4.9.

Figure 4.9(a) shows that as the number of bins used in the data handling process increases, the simulation takes more generations to converge. Increasing the number of bins from 5 to 60 forces the simulation to need 939 generations to converge rather than 13. This is a direct result of the effect seen in Figure 4.9(b). As the number of histogram bins increases, the number of possible Pareto-optimal points increases. When a high number of possible Pareto-optimal points exist, a generation to generation analysis is more likely to find a large number of *new* Pareto-optimal points, thus a large value of ΔPM. The value of ΔPM will need to progress through more generations to satisfy the convergence criterion.

Figure 4.9(b) shows that increasing the number of bins used in the data handling process will increase the number of Pareto-optimal points in the final set of optimum designs. Increasing the number of bins from 5 to 60 increases the resulting number of Pareto-optimal points from 26 to 2214. This drastic change is a result of the data handling technique outlined in Section 4.2.3.2. The number of

histogram bins in this process defines a theoretical upper limit on the number of possible Pareto-optimal points for a given simulation. The number of histogram bins discretizes the predicted Pareto-optimal hypersurface by setting a resolution or fineness to each design vector in Step 3 of the data handling process.

Figure 4.9(c) shows that a particular optimum number of bins exist which minimizes the mean error and RMS error in the predictions. If there are not enough or too many bins, the accuracy suffers. The optimal number of histogram bins in this study is 20. If there are too few bins (10 or 5 bins in this example), the number of Pareto-optimal points decreases significantly (Figure 4.9(b)). As the number of Pareto-optimal points decreases, the post-optimality data handling equations have significantly less designs to choose from. This would result in a loss of accuracy for each selected design. If there are too many bins (40 or 60 bins in this example), the number of samples present in each bin when performing Step 3 in Section 4.2.3.2 and the averaging operators in Equations 4.11 and 4.13 decreases. This means the averaging operators would have a smaller sample size and become less accurate. This effect was also seen and discussed in Section 4.4.1.

4.4.3   Effects of Changes in Number of Uncertainty Subsets

Three total simulations (S1, S2, and Baseline) were run to compare how changes in the number of uncertainty subsets affect the speed, quality, and accuracy of the predicted robust optimum design vectors. Graphs illustrating these changes are provided in Figure 4.10.

Figure 4.10(a) shows that as the number of uncertainty subsets used in the optimization formulation increases, the simulation takes longer to converge. Increasing the number of uncertainty subsets from 3 to 8 increased the generation number at convergence from 108 to 187. This effect is due to the same phenomena discussed in Section 4.4.1. By the optimization problem definition in Equation 4.9, more uncertainty subsets means the multi-objective optimization problem involves more objective functions. The increase in the number of more objective functions increases the fraction of points in the population which are non-dominated, thus decreasing the effectiveness of the NSGA-II algorithm (see Section 8.8.2 in Deb [94]).

Figure 4.10(b) shows that increasing the number of uncertainty subsets used in the optimization formulation from 3 to 5 will substantially increase the number of Pareto-optimal points in the final set of optimum designs from 177 points to 337 points. Adding objective functions inherently increases the number of possible Pareto-optimal points, due to the increase in the dimensions of the Pareto-optimal front. Increasing the number of subsets from 5 to 8 shows a minimal increase from 337 to 348 points. This is due to either the lack of individuals in the population or a lack of histogram bins for an optimization problem with eight objective functions. This effect is coupled with the effects seen in Sections 4.4.1 and 4.4.2.

Figure 4.10(c) shows that the accuracy (both mean and RMS errors) improves with an increasing number of uncertainty subsets. This effect on accuracy proved to be the strongest out of all changes seen in Section 4.4. Increasing the number of uncertainty subsets from 3 to 8 decreased the mean error from 21.5% to 5.9% and the RMS error from 14.6% to 3.8%. This is largely due to the fact that the

approximations of the uncertainty PDFs through the calculations of the weights in Equations 4.12 and 4.15 are more accurate. This is especially true for the smaller values of σ. More uncertainty subsets are utilized when making the predictions and the changes in the weights are more dynamic. This concept is discussed and illustrated in the full analysis of the baseline results in Section 4.3.3.
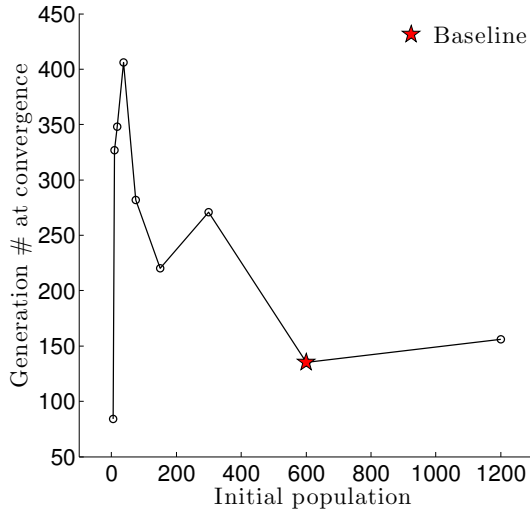
(a) Speed vs. initial population size
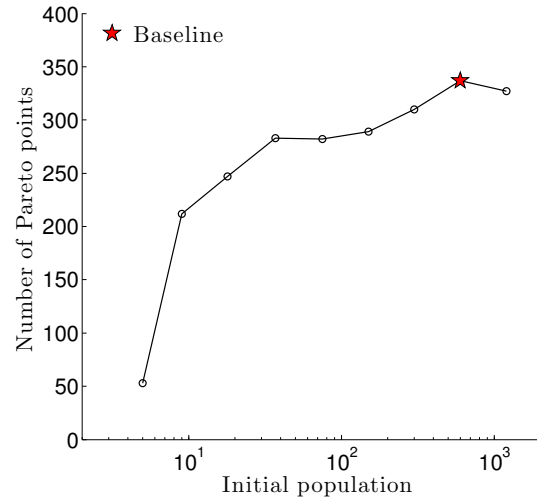
(b) Quality vs. initial population size
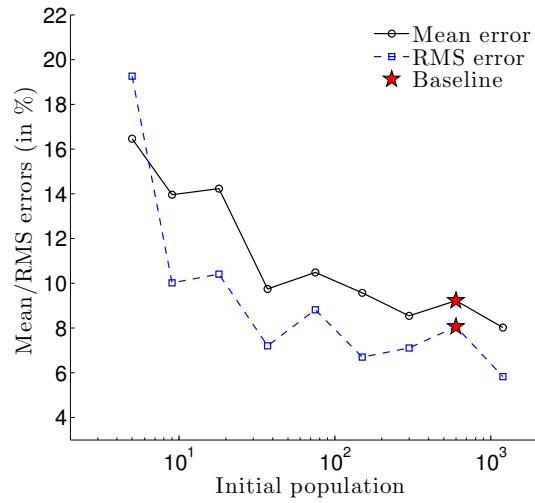
(c) Accuracy vs. initial population size

Figure 4.8: Speed, quality, and accuracy changes with change in initial population size.
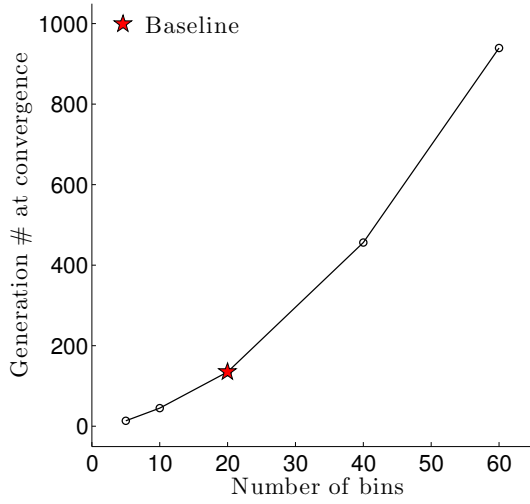
(a) Speed vs. number of histogram bins
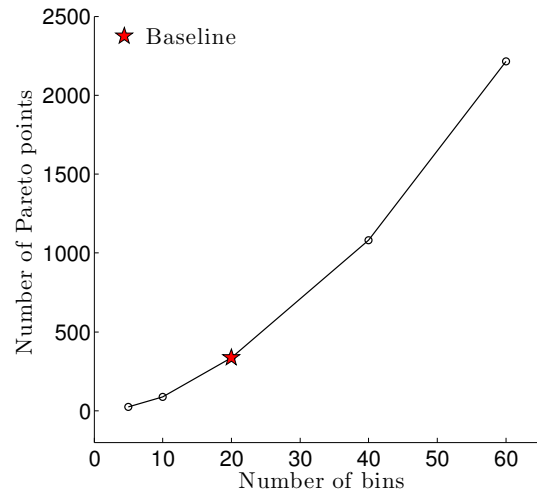
(b) Quality vs. number of histogram bins
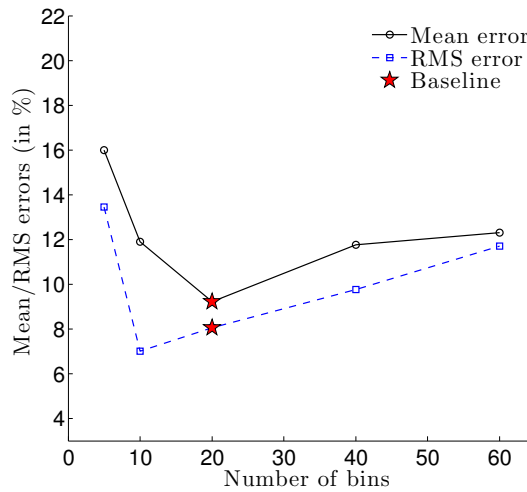
(c) Accuracy vs. number of histogram bins

Figure 4.9: Speed, quality, and accuracy changes with change in number of histogram bins used in the data handling procedure.
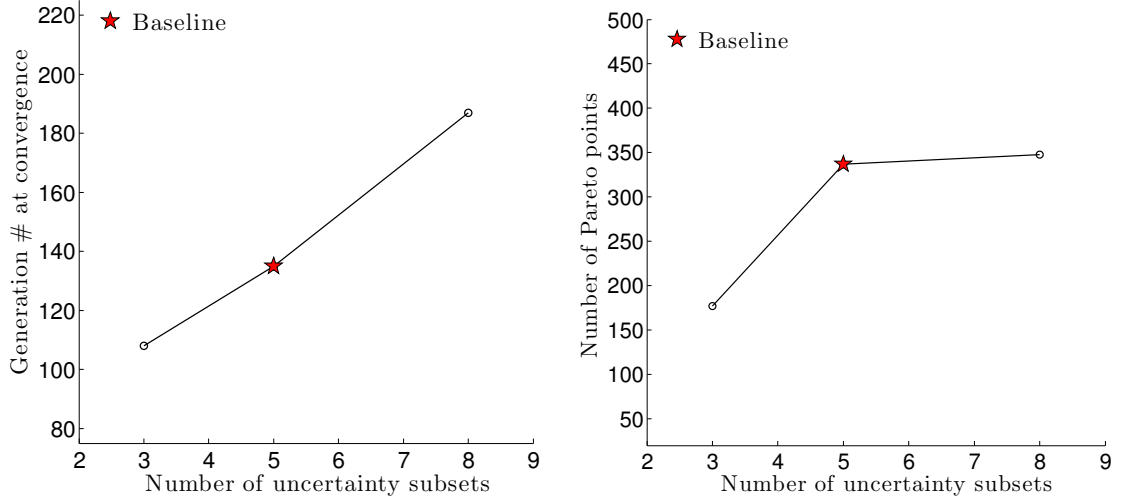
(a) Speed vs. number of uncertainty subsets   (b) Quality vs. number of uncertainty subsets
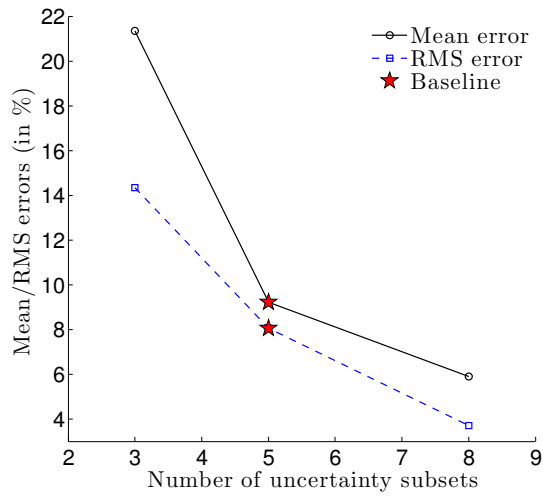
(c) Accuracy vs. number of uncertainty subsets

Figure 4.10: Speed, quality, and accuracy changes with change in number of uncertainty subsets in the multi-objective optimization problem formulation.

Chapter 5:   Vehicle Design Optimization Methodology

Both multi-objective and robust optimization studies were performed to find optimum vehicle geometries and to analyze trade-offs between vehicle performance and controllability under asymmetric boundary-layer conditions. Objective functions of lift-to-drag ratio, internal volumetric efficiency, maximum heat flux, and vehicle controllability were included in the studies. The multi-objective studies produce sets of Pareto-optimal solutions. These solutions illustrate the trade-offs between the competing objective functions. The L^2-norm optimum Pareto-optimal points were found, identifying single optimum designs of minimum compromise [97]. The robust optimization studies focused on the objective function pertaining to vehicle controllability. Several commonly used robust optimization techniques were applied in order to identify vehicle designs which minimize the worst-case scenario and expected value of the influence of roughness-induced ABLT. This vehicle optimization problem was also used as a test-bed for the the novel robust optimization method presented in Section 4.2.3. All optimization problems were solved using a multi-objective genetic algorithm to predict global optimality.

Chapter 5 is organized as follows. Section 5.1 will discuss the design point specifications for all the optimization problems investigated in this study. This

discussion includes design vector formulation, the side constraints applied to the design variables, and pertinent center of gravity (CG) assumptions. Within the multi-objective context, two sets of optimization problems were solved. One was a case where the objective functions were defined and solved without the presence of an isolated roughness; no asymmetric boundary-layer was induced. The second problem involved finding optimized geometries which are most robust to a single disturbance which could occur on the top surface of the vehicle at any spanwise location. In other words, the resulting optimum shapes are vehicles which are the least affected by a random asymmetric boundary-layer condition.

The two multi-objective based optimization problems, with and without an ABLT event, will be formed in Section 5.2 and Section 5.3.1, respectively. In addition, each scenario was solved for both infinitely sharp leading edge and blunted leading edge waveriders. The concept of a roughness-induced ABLT event occurring on the vehicle with some probability is extended in the robust optimization studies in Section 5.3.2. The objective functions and constraint functions for each class of optimization problems are presented in their respective sections. Finally, Section 5.4 concludes Chapter 5 with information regarding the optimization method and parameters used to solve each problem.

5.1   Optimization Design Point, Constraints, and Assumptions

All the optimization problems were solved at a particular set of design point specifications. These specifications define the freestream conditions and geometric

constraints of the problem. The design point parameters are listed in Table 5.1. Most of these specifications match those of Starkey [30] to aid in the validation of the models and comparisons of the results. As a side note, the simulations were also run at a higher Mach number ($M_\infty = 18$) where it was found that the geometric trends of the results stayed the same. The differences existed only in the magnitudes of the objective functions. However, the geometric constraints did prove to make significant changes to the shape of the optimum waverider designs. Studies on this effect is suggested for future work.

Note that CG assumption I was used for all multi-objective formulations in Sections 5.2 and 5.3.1. This was initially used as a first order assumption. Once simulation results were collected and analyses were conducted, the decision was made to update the CG assumption to a center of volume assumption (CG assumption II). CG assumption II was applied to the formulations for the robust optimization problems in Section 5.3.2.

Table 5.1: Design point specifications.

Parameter	Value
Freestream Mach number	8
Altitude	60,000 ft
Freestream pressure	150 lb/ft^2
Freestream temperature	389.99 °R
Minimum vehicle internal volume	88,286 ft^3
Maximum vehicle internal volume	105,944 ft^3
CG (x,y,z) assumption I	$\left(\frac{L}{2}, 0, \frac{L}{4}\tan\left(\theta_{local}\right)\right)$
CG assumption II	Center of volume

Using the methodology outlined in Section 2.1, the design vector contains variables fully describing a vehicle geometry. A design vector is defined by

$$\vec{x} = \begin{bmatrix} n & m & \theta & \delta & L & w \end{bmatrix}, \tag{5.1}$$

for sharp leading edge waveriders and by

$$\vec{x} = \begin{bmatrix} n & m & \theta & \delta & L & w & d \end{bmatrix}, \tag{5.2}$$

for blunted leading edge waveriders. These vector definitions are used for all optimization formulations in Chapter 5. The design vectors defined by Equations 5.1 and 5.2 belong to the design vector set space $\mathbb{X}$, bounded by user defined lower and upper bounds. For the multi-objective problems in Sections 5.2 and 5.3.1, the bounds of the design vector were set to be

$$\vec{x}_{lb} \leq \vec{x} \leq \vec{x}_{ub} = \begin{bmatrix} 0.001 \leq n \leq 1.0 \\ 0.001 \leq m \leq 1.0 \\ 1° \leq \theta \leq 10° \\ 1° \leq \delta \leq 20° \\ 1\,\text{ft} \leq L \leq 220\,\text{ft} \\ 1\,\text{ft} \leq w \leq 120\,\text{ft} \end{bmatrix}, \tag{5.3}$$

96

for sharp waveriders and

$$\vec{x}_{lb} \leq \vec{x} \leq \vec{x}_{ub} = \begin{bmatrix} 0.001 \leq n \leq 1.0 \\ 0.001 \leq m \leq 1.0 \\ 1° \leq \theta \leq 10° \\ 1° \leq \delta \leq 20° \\ 1\,\text{ft} \leq L \leq 220\,\text{ft} \\ 1\,\text{ft} \leq w \leq 120\,\text{ft} \\ 0.0164\,\text{ft} \leq d \leq 1.64\,\text{ft} \end{bmatrix}, \tag{5.4}$$

for blunt waveriders. Due to floating-point precision limits on the calculations of the CG location for CG assumption II, the lower limit of variables n and m for Section 5.3.2 was changed from 0.001 to 0.05.

5.2   Baseline Multi-Objective Optimization

The baseline multi-objective optimization problem was formulated as follows:

$$
\begin{aligned}
\min_{\vec{x}} \quad & f_{q,scaled}(\vec{x}) \qquad q = 1, 2, ..., Q \\
\text{s.t.} \quad & \\
& g_j(\vec{x}) \leq 0 \qquad j = 1, 2, ..., J \\
& \vec{x} \in \mathbb{X} \\
& \mathbb{X} = \{\vec{x} | \vec{x}_{lb} \leq \vec{x} \leq \vec{x}_{ub}\},
\end{aligned}
\tag{5.5}
$$

where Q is the total number of objective functions and J is the total number of constraint functions. The objective functions for the baseline case are defined by the following:

$$f_1\left(\vec{x}\right) = -\frac{Lift}{Drag} \, , \tag{5.6}$$

$$f_2\left(\vec{x}\right) = -\eta \, , \tag{5.7}$$

$$f_3\left(\vec{x}\right) = \|\vec{C}_{MCG,tot}\| \, , \tag{5.8}$$

$$f_4\left(\vec{x}\right) = max\left(q_w\right) \, . \tag{5.9}$$

Functions f_1 through f_3 are used for the sharp leading edge waverider case ($Q = 3$) and f_4 is added for the blunt waverider case ($Q = 4$). The constraints added to the formulated optimization problem are the following:

$$g_1\left(\vec{x}\right) = \left(V - 105,944\right) \leq 0 \, , \tag{5.10}$$

$$g_2\left(\vec{x}\right) = \left(88,286 - V\right) \leq 0 \, , \tag{5.11}$$

$$g_3\left(\vec{x}\right) = \left(1 - \frac{m}{n}\frac{\tan\delta}{\tan\delta - \tan\theta}\right) < 0 \, , \tag{5.12}$$

$$g_4\left(\vec{x}\right) = \left(max\left(\theta_{local}\right) - \theta_{max}\right) \leq 0 \, . \tag{5.13}$$

Functions g_1 through g_3 are used for the blunt leading edge waverider case ($J = 3$) and g_4 is added for sharp leading edge case ($J = 4$).

Objective function f_1 is the lift-to-drag ratio of the vehicle preceded with a negative sign. It is calculated using the aerodynamic methods described in Chapter 2. The goal here is to maximize the lift-to-drag ratio. To keep with a minimization convention, the optimizer attempts to minimize f_1. Objective function f_2 is the volumetric efficiency, η, of the vehicle preceded with a negative sign. The volumetric

efficiency is defined by comparing the vehicle's wetted surface area to the surface area of a sphere of equal volume. This was done due to the fact that a sphere is the most volumetrically efficient shape possible. The volumetric efficiency is defined by,

$$\eta \equiv \frac{(36\pi)^{\frac{1}{3}} V^{\frac{2}{3}}}{S_w} \ , \tag{5.14}$$

where V is the vehicle internal volume and S_w is the wetted surface area. The goal of this vehicle design problem is to maximize the volumetric efficiency by minimizing f_2. Objective function f_3 is a measure of the vehicle's trimmability and is defined as the magnitude of the moment coefficient given by Equation 2.14. The smaller the magnitude of f_3, the smaller the control moments need to be to trim the vehicle at the design attitude. Therefore, f_3 is minimized by the optimizer. Objective function f_4 is the maximum heat flux that occurs for any panel on the blunted leading edge of the vehicle. This is an important parameter for heat shield design and TPS sizing. This value is minimized by the optimizer.

Objective functions are scaled so that they are all on the same order of magnitude and so they also convert the problem to a minimization type [98]. To accomplish this, an estimate of the best and worst possible values of each objective function are used. These points are called "good" points and "bad" points, respectively. Scaling an objective function using these points is accomplished by the following equation:

$$f_{q,scaled} = \frac{f_q - f_{q,good}}{f_{q,bad} - f_{q,good}} \ . \tag{5.15}$$

The scaled values of the objective functions are in the range of [0,1], where a smaller the value is more optimum. The values of the corresponding good and bad points for each objective function are given in Table 5.2 in Section 5.4. Note that the good

and bad points were chosen by observing test results of preliminary optimization runs and may not always successfully scale the objective functions to lie exactly in the range of [0,1].

The g_1 and g_2 constraints are required to keep the internal volume within the requirements set in Table 5.1. Constraint g_3 is necessary for a geometrically feasible concave vehicle (when $\theta < \delta$) to be generated by the method outlined in Section 2.1. This constraint keeps the bottom surface of the waverider from crossing the top surface [30]. The last constraint, g_4, is necessary for an attached shock condition at the leading edge as discussed in Chapter 2. Constraint g_4 is only applied for the sharp leading edge cases. The most common way of handling constraints in genetic algorithms is by the use of a penalty method [98]. An exterior penalty method was used to handle the constraints in this work. The idea is to alter the fitness value of an individual by a severe penalty if it violates a constraint. The exterior penalty method applied to the scaled objective functions is given by

$$f_{q,con} = f_{q,scaled} + K \sum_{j=1}^{J} \{g_j\} \, , \tag{5.16}$$

where K is a penalty factor of 10^5 and the bracket function $\{g_j\}$ is defined as

$$\{g_j\} = \begin{cases} g_j, & \text{if } g_j \geq 0 \\ 0, & \text{if } g_j < 0 \end{cases} . \tag{5.17}$$

5.3 Influence of Asymmetric Boundary-Layer

5.3.1 Multi-Objective Optimization

The multi-objective optimization problem under the influence of ABLT is formulated to be the same as the baseline :

$$
\begin{aligned}
&\min_{\vec{x}} \quad f_{q,scaled}\left(\vec{x}\right) \qquad q = 1, 2, ..., Q \\
&s.t. \\
&\qquad g_j\left(\vec{x}\right) \leq 0 \qquad j = 1, 2, ..., J \\
&\qquad \vec{x} \in \mathbb{X} \\
&\qquad \mathbb{X} = \left\{\vec{x} | \vec{x}_{lb} \leq \vec{x} \leq \vec{x}_{ub}\right\},
\end{aligned}
\tag{5.18}
$$

where now a single isolated disturbance is introduced at the leading edge of the top surface of the vehicle. The lateral position of the disturbance is added to the optimization problem as an integer valued environmental parameter p. The value of p represents a spanwise position of the isolated roughness in increments of one-eighth the total span of the waverider. Four lateral positions were used spanning outward from the centerline of the vehicle as illustrated in Figure 5.1.

The idea behind incorporating an ABLT event to the multi-objective optimization problem was to identify vehicles that are the most capable of withstanding the effect of a turbulence wedge and remaining controllable. A vehicle state is said to be *controllable* if there exists a control signal, over some finite time interval, that can bring the vehicle to a future state equal to the desired equilibrium state [99]. In other words, any vehicle state which the control system has enough authority to bring it to a trimmed condition is considered a controllable state. The set of all

101
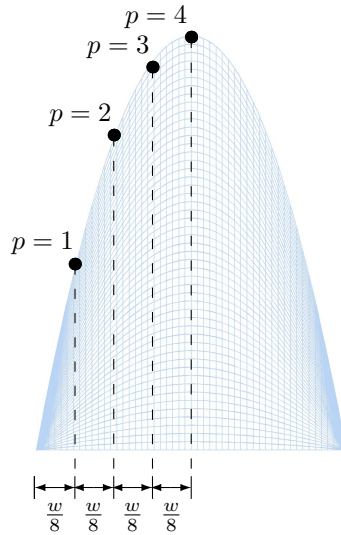
Figure 5.1: Parametric locations of leading edge isolated roughness (planform view).

states which are controllable define the vehicle controllability region. The size of
the controllability region can be considered as a measure of the allowable level of
external disturbances [100].

   With these definitions, two things can be taken into account when predicting
if an external event will cause the loss of a vehicle: the size of the controllability
region and the size of the external disturbance. Minimizing the chance of losing
a vehicle due to an external disturbance can be accomplished by maximizing the
controllability region of the vehicle and/or minimizing the size of the external dis-
turbance. To accomplish the former, in the current work, the dynamics of the range
of waveriders modeled would need to be calculated. This, as discussed in Section
1.4.1, can be difficult and potentially inaccurate. In addition, assumptions pertain-
ing to the control system (flaps, thrusters, etc.) would need to be made. This is
a very difficult task to do a priori without any knowledge of vehicle shape and in-

ternal volume distribution. Instead, the best first step is to accomplish the latter and minimize the external disturbance on the vehicle. This requires no restrictive assumptions to be made about the type and strength of the control system on the vehicle. This, in turn will minimize the chances of the external disturbance moving the system out of the controllability region, where no controller is able to keep the system stable [100].

To capture this, a controllability objective function was defined by modifying the definition of f_3 in Equation 5.8. The resulting objective function f_3 specifically for Section 5.3.1 is defined by

$$f_3\left(\vec{x}\right) = \frac{1}{4}\left(f_{3,span}\left(\vec{x},1\right) + f_{3,span}\left(\vec{x},2\right) + f_{3,span}\left(\vec{x},3\right) + f_{3,span}\left(\vec{x},4\right)\right), \qquad (5.19)$$

where

$$f_{3,span}\left(\vec{x},p\right) = abs\left(\|\vec{C}_{M_{CG,tot}}\|_{with} - \|\vec{C}_{M_{CG,tot}}\|_{without}\right). \qquad (5.20)$$

Minimizing $f_{3,span}$ at a particular spanwise position minimizes the absolute value of the difference between the length of the moment vector with a turbulence wedge present and the length of the moment vector without a turbulence wedge present. When Equation 5.19 is minimized, the effect due to an isolated disturbance which may occur at any of the four spanwise positions is minimized. Therefore, the vehicle design which minimizes Equation 5.19 best maintains its controllability characteristics if an isolated roughness event would happen to occur at any of these four spanwise locations. The the rest of the objective functions, constraint functions, scaling method, and constraint handling method described in Section 5.2 is the same for Section 5.3.1.

Calculating the moment coefficient characteristics at four different spanwise locations in Equation 5.19 increased the computational expense of the optimization problem. To more efficiently use the calculations that are being performed, the objective function f_3 in Equation 5.18 was changed to a robust counterpart function using the Tsutsui perturbation approach [72, 73]:

$$
\begin{aligned}
\min_{\vec{x}} \quad & F_{3,scaled}\left(\vec{x}, p\left(t\right)\right) = f_{3,span,scaled}\left(\vec{x}, p + \Delta p\left(t\right)\right) \\
s.t. \quad & \\
& g_j\left(\vec{x}, p\right) \leq 0 \qquad j = 1, 2, ..., J \\
& \vec{x} \in \mathbb{X} \\
& \mathbb{X} = \{\vec{x} | \vec{x}_{lb} \leq \vec{x} \leq \vec{x}_{ub}\} \\
& \left(p + \Delta p\left(t\right)\right) \sim \mathcal{U}_D\left(\tilde{p}\right) \\
& \tilde{p} = \{1, 2, 3, 4\} \,,
\end{aligned}
\tag{5.21}
$$

where t is a generation index and $p + \Delta p\left(t\right)$ is a random value (1, 2, 3, or 4) at generation t.

The goal of the original optimization problem and f_3 of Equations 5.18 and 5.19 was to identify waverider geometries that are robust to an unintended roughness element that may appear anywhere on the top surface of the waverider. To mirror this effect in Equation 5.21, the value of $p + \Delta p\left(t\right)$ is set randomly at the start of each generation within the MOGA solver. All calculations performed for each individual in the population for a given generation uses that particular value of $p + \Delta p\left(t\right)$. Therefore, for a large number of generations, each spanwise location (1, 2, 3, or 4) would tend to be equally represented and the final optimum design should be robust to a turbulence wedge which may occur at any of these spanwise locations. The last step when evaluating Equation 5.21 within a MOGA solver was to take the solution

set of Pareto-optimal points from the evaluate them for the original f_3 in Equation 5.19.

5.3.2 Robust Optimization Formulations

The robust optimization formulations aid in further exploring and analyzing the design space by focusing on uncertainty in the position of the surface roughness parameter. The waverider geometries used in this section are all assumed to have an infinitely sharp leading edge. To quantify the effect of an asymmetric flow field on the controllability of the vehicle, the sole objective function used in the optimization studies in this section was the following:

$$f\left(\vec{x}, p\right) = abs\left(\|\vec{C}_M\|_{with} - \|\vec{C}_M\|_{without}\right) , \tag{5.22}$$

where $\|\vec{C}_M\|$ is the magnitude of the moment coefficient vector taken about the center of gravity of the vehicle. Note, $\|\vec{C}_M\|$ is shorthand and is equivalent to $\|\vec{C}_{M_{CG,tot}}\|$. Subscripts *with* and *without* denote conditions with and without the asymmetric flow field (turbulence wedge) present, respectively. This formulation isolates the effect of the roughness and defines the moment increment, $\Delta\vec{C}_M$, which needs to be attenuated using vehicle stability and control mechanisms. Minimizing this moment increment minimizes the amount of control needed to keep the system at trimmed conditions and gives the best likelihood that the vehicle will not be perturbed outside its controllability region.

Parameter p denotes a lateral distance of the isolated roughness on the leading edge of the top surface of the vehicle. Parameter p spans from the center line of

the vehicle ($p = 0.5$) to the full half-span of the vehicle ($p = 0.0$). Therefore, the

bounded environmental parameter uncertainty set for the hypersonic vehicle design

problem is defined by

$$p \in \mathbb{P} = \{p|0.0 \le p \le 0.5\} \,. \tag{5.23}$$

Note, the parameter uncertainty space here is continuous and connected, unlike the

discrete uncertainty space in Section 5.3.1. Figure 5.2 provides example locations

of the isolated roughness for various values of p.

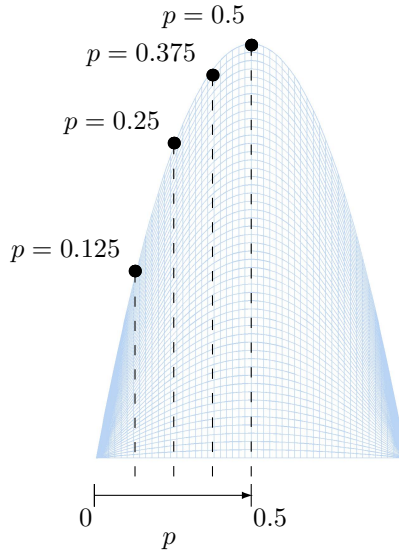Figure 5.2: Example locations of leading edge isolated roughnesses as function of p (planform view).

Using the terminology in Chapter 4, the original optimization problem is for-

mulated as follows:

$$\min_{\vec{x}} \quad f\left(\vec{x}, p\right) = abs\left(\|\vec{C}_M\|_{with} - \|\vec{C}_M\|_{without}\right) \tag{5.24}$$

$$\vec{x} \in \mathbb{X} = \{\vec{x}|\vec{x}_{lb} \le \vec{x} \le \vec{x}_{ub}\} \;,$$

where $\vec{x}$ is the design vector defined by Equation 5.1. The design vector belongs to the design vector set space $\mathbb{X}$ defined by Equation 5.3, where the lower bound on variables n and m are 0.05.

Each of the four methods described in Section 4.2 forms a robust counterpart optimization problem to the original problem defined by Equation 5.24. The formulated robust counterpart optimization problem for the robust regularization-based method is given by,

$$\min_{\vec{x}} \quad F_I\left(\vec{x}\right) = \max_{p \in \tilde{p}} \; abs\left(\|\vec{C}_M\left(\vec{x}, p\right)\|_{with} - \|\vec{C}_M\left(\vec{x}, p\right)\|_{without}\right)$$

$$\vec{x} \in \mathbb{X}$$
$$\tilde{p} = \{p | 0.0, 0.05, 0.1, \ldots, 0.45, 0.5\} \subset \mathbb{P}\,. \tag{5.25}$$

Note here, the supremum over the uncertainty set, $\sup_{p \in \mathbb{P}}$, was approximated by a maximization over a discrete subset $\tilde{p}$. This was done as an attempt to solve the inner optimization problem with less computational expense than a genetic algorithm or gradient-based method, while maintaining accuracy in the solution.

The explicit averaging method forms the following robust counterpart optimization problem:

$$\min_{\vec{x}} \quad F_{II}\left(\vec{x}, p\right) = \sum_{i=1}^{10} \frac{1}{10} abs\left(\|\vec{C}_M\left(\vec{x}, p + \Delta p_i\right)\|_{with} - \|\vec{C}_M\left(\vec{x}, p + \Delta p_i\right)\|_{without}\right)$$

$$\vec{x} \in \mathbb{X}$$
$$\left(p + \Delta p_i\right) \sim \mathcal{U}\left(0.0, 0.5\right)\,.$$

$$\tag{5.26}$$

Note here, the Monte Carlo integration was performed using 10 samples. This number of samples was found to perform adequately while maintaining a feasible computational expense. The value of the environmental parameter was chosen to

be sampled from a uniform distribution over the uncertainty set. This distribution was chosen as a baseline and is suggested to be used if the designer has no educated guess on the probability of a roughness occurring on the surface. If, for example, the designer knows that the vehicle is made up of different ablative materials, an educated guess of where a roughness is more likely occur is possible. Or if the vehicle has machining marks, screw heads, or rivets, areas with a higher probability of transition can be identified. These example scenarios would lend towards a non-uniform uncertainty PDF.

The perturbation method forms the following robust counterpart optimization problem:

$$\min_{\vec{x}} \quad F_{III}\left(\vec{x}, p\left(t\right)\right) = abs\left(\|\vec{C}_M\left(\vec{x}, p + \Delta p\left(t\right)\right)\|_{with} - \|\vec{C}_M\left(\vec{x}, p + \Delta p\left(t\right)\right)\|_{without}\right)$$

$$\vec{x} \in \mathbb{X}$$
$$\left(p + \Delta p\left(t\right)\right) \sim \mathcal{U}\left(0.0, 0.5\right) \ .$$

$$(5.27)$$

The robust multi-objective approach forms the following robust MOGA counterpart optimization problem:

$$\min_{\vec{x}} \quad F_{IV_m}\left(\vec{x}, \breve{p}_m\left(t\right)\right) = abs\left(\|\vec{C}_M\left(\vec{x}, \breve{p}_m\left(t\right)\right)\|_{with} - \|\vec{C}_M\left(\vec{x}, \breve{p}_m\left(t\right)\right)\|_{without}\right)$$
$$m = 1, 2, 3, 4, 5$$

$$\vec{x} \in \mathbb{X}$$
$$\breve{p}_1\left(t\right) \sim \mathcal{U}\left(0.0, 0.1\right)$$
$$\breve{p}_2\left(t\right) \sim \mathcal{U}\left(0.1, 0.2\right)$$
$$\breve{p}_3\left(t\right) \sim \mathcal{U}\left(0.2, 0.3\right)$$
$$\breve{p}_4\left(t\right) \sim \mathcal{U}\left(0.3, 0.4\right)$$
$$\breve{p}_5\left(t\right) \sim \mathcal{U}\left(0.4, 0.5\right) \ .$$

$$(5.28)$$

Note the robust MOGA counterpart formulation set $M = 5$, creating five objective functions. This value was chosen as a trade-off between accuracy of the post-optimality handling prediction (Equations 4.11 and 4.13) and the MOGA problem complexity (as M gets larger, the problem becomes more difficult to solve [94, 95]).

5.4 MOGA Method and Parameters

5.4.1 Multi-Objective Studies MOGA Parameters

The multi-objective optimization problems outlined in Sections 5.2 and 5.3.1 were solved using the MATLAB GADS toolbox. The multi-objective genetic algorithm solver in the GADS toolbox employs a modified version of an elitist non-dominated sorting genetic algorithm method, NSGA-II [94]. Table 5.2 lists all the parameters which were necessary to run the MOGA solver.

Deb suggests that for a multi-objective optimization problem with four objective functions a population size of at least 100 is to necessary to maintain reasonable effectiveness using the elitism scheme (see Figure 276 in Deb [94]). Therefore, the population size was set to 100 for all optimization runs. The MOGA solver was set to terminate after a particular number of generations was computed. The number of generations was determined by running several test cases and observing the change in the Pareto spread from generation to generation. For the baseline multi-objective studies in Section 5.2, it was decided that after 500 generations the average change in the Pareto spread from generation to generation was not significant. In other words, the Pareto-optimal front was not making significant progress towards

more optimum designs. For the multi-objective optimization studies under the influence of an asymmetric boundary-layer transition (Section 5.3.1), this was found to be the case after 2000 generations. These numbers were set subjectively and may not always guarantee that the final Pareto-optimal points adequately cover the entire design space or accurately represent the true Pareto-optimal front. Genetic algorithms have no guarantee of global optimality and/or sufficient coverage of the design space. In an attempt to minimize the chances of obtaining an inadequate or inaccurate set of Pareto-optimal points, the current study ran each of the four cases 25 times.

Table 5.2: MOGA parameters for the multi-objective optimization studies.

Parameter	Case			
	Baseline case: sharp	Baseline case: blunt	ABLT case: sharp	ABLT case: blunt
Population size	100	100	100	100
Number of generations	500	500	2000	2000
Number of MOGA runs	25	25	25	25
$F_{1,good}$	10	10	10	10
$F_{2,good}$	1	1	1	1
$F_{3,good}$	0	0	0	0
$F_{4,good}$	N/A	$30 \ \mathrm{W/cm^2}$	N/A	$30 \ \mathrm{W/cm^2}$
$F_{1,bad}$	0	0	0	0
$F_{2,bad}$	0	0	0	0
$F_{3,bad}$	0.05	0.05	5×10^{-6}	5×10^{-6}
$F_{4,bad}$	N/A	$400 \ \mathrm{W/cm^2}$	N/A	$400 \ \mathrm{W/cm^2}$

5.4.2 Robust Optimization Studies MOGA Parameters

The four robust counterpart optimization problems described by Equation 5.25 through Equation 5.28 were solved using the MATLAB GADS toolbox. The MOGA solver in the GADS toolbox employs a modified version of the elitist non-dominated sorting genetic algorithm NSGA-II [94]. Table 5.3 lists all the genetic algorithm settings which were necessary to run the MOGA solver for each robust formulation.

Table 5.3: Genetic algorithm options for the robust optimization studies.

Genetic algorithm option	Setting
Population size	50 (50·M for MOGA)
Initial population	Random within x_{lb} and x_{ub}
Fitness scaling	Normalized to range between 0 and 1
Selection	Stochastic uniform selection
Crossover	Randomized scattered
Crossover fraction	0.8
Mutation	Gaussian
Convergence criterion	Run for 1000 generations (2000 for MOGA)

A population size of 50 was used for the single-objective methods (robust regularization and the two aggregation methods). The methods, when using a population of this size, were observed to make significant progress from generation to generation in the initial stages of the simulation while maintaining a reasonable computational expense. A population size of $50M$ (or 250 for five objectives) was used for the robust MOGA method. This ensured that the population size exceeded the minimum values necessary to maintain reasonable effectiveness when using the

NSGA-II elitism scheme (see Figure 276 in Deb [94]). Objective function values were all scaled using the same method outlined in Section 5.2. The simulation was configured to run for a set number of generations. The number of generations was set such that the generation histories show a significant level of convergence. Generation histories are provided in the following sections illustrating the extent of convergence for each method as a function of generation number.

Chapter 6: Results

This chapter presents the results of the optimization problems formulated in Chapter 5. The results presented here were found by solving the baseline optimization problems and the ABLT influenced optimization problems (Sections 5.2 and 5.3, respectively), under the assumptions outlined in Section 5.1 using the method and parameters given in Section 5.4.

This chapter parallels Chapter 5, where the baseline optimization results are given in Section 6.1 and the ABLT influenced optimization results are given in Section 6.2. Within this chapter, two categories of results are presented: multi-objective optimization results and robust optimization results. Multi-objective optimization results are found in Sections 6.1 and 6.2.1, while the robust optimization results are found in Section 6.2.2. These two categories of results are presented with slightly different nomenclature, and were found using slightly different convergence criteria. The following paragraphs will provide a brief introduction into how the results were found and will be presented in the subsequent sections in this chapter.

The multi-objective optimization results in Sections 6.1 and 6.2.1 are split into four cases: a baseline case with infinitely sharp leading edges, a baseline case with blunted leading edges, an ABLT case with sharp leading edges, and an ABLT case

with blunted leading edges. Each of the four optimization cases described in Table 5.2 were run 25 times using the MOGA solver, producing 25 sets of Pareto-optimal points per case. The 25 sets were compared for dominance and combined to create an overall set of non-dominated Pareto-optimal points. The results presented in Sections 6.1 and 6.2.1 analyze the two following types of points that exist in the overall set Pareto-optimal points for each case:

- extreme Pareto-optimal points

- L^2-norm optimum Pareto-optimal point

The extreme Pareto-optimal points are the points in the set which have the minimum value for each individual objective function. Designs which represent the extreme Pareto-optimal points that minimize the *scaled* objective functions will be termed "best" designs for the corresponding objective functions. These points help illustrate the trade-offs that exist between the objectives, showing the full range of compromise. The L^2-norm optimum Pareto-optimal point represents the design that minimizes the compromise between all the objectives by minimizing

$$\sqrt{\sum_{q=1}^{Q} \left(abs \left(f_q - f_{q,min} \right)^2 \right)} \,, \tag{6.1}$$

where $f_{q,min}$ is the extreme Pareto-optimal point for objective q. A simplified two objective example is given in Figure 6.1 to help illustrate where these types of Pareto-optimal points exist on the Pareto-optimal front.

The robust optimization results in Sections 6.2.2.1, 6.2.2.2, and 6.2.2.3 are found from solving a single-objective optimization problem. These sections therefore
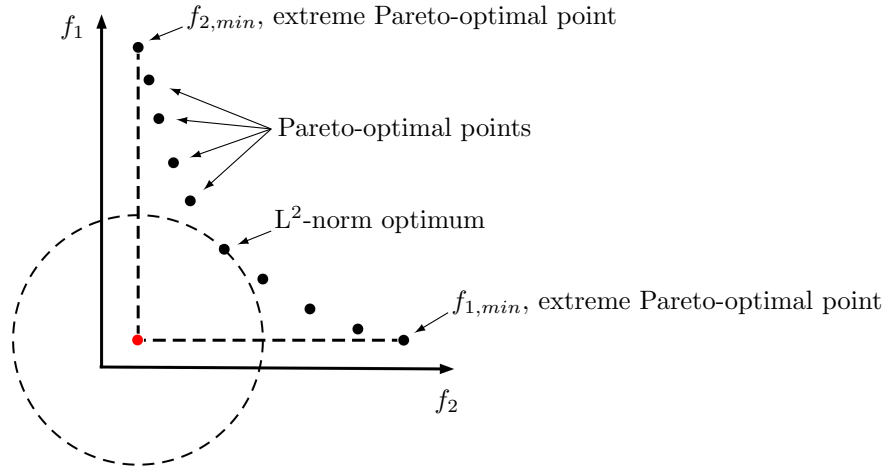
Figure 6.1: Two objective function example showing extreme Pareto-optimal points and L^2-norm optimum Pareto-optimal point.

provide a single robust optimum design. The results in Section 6.2.2.4 are found by solving a multi-objective optimization problem and therefore exist as a set of optimum designs. The nuances to this particular Pareto-optimal set of designs is discussed in detail in Section 4.2.3. In addition, an illustrative example problem formulation and corresponding results are presented in Section 4.3.

6.1 Baseline Multi-Objective Optimal Geometries

6.1.1 Infinitely Sharp Case

Two classes of shapes were identified from the extreme Pareto-optimal designs for the infinitely sharp baseline case: wedge-like and cone-like. Wedge-like shapes are produced when the variable n approaches zero and $\theta \approx \delta$. Cone-like shapes are produced when n approaches unity for a moderately convex vehicle ($\theta > 2\delta$). The

best f_1 and best f_3 designs were wedge-like in shape and had a small wedge angle. The best f_2 design was cone-like. Isometric views of the best designs are shown in Figure 6.2. The corresponding objective function values and design vectors are presented in Table 6.1 and Table 6.2, respectively.
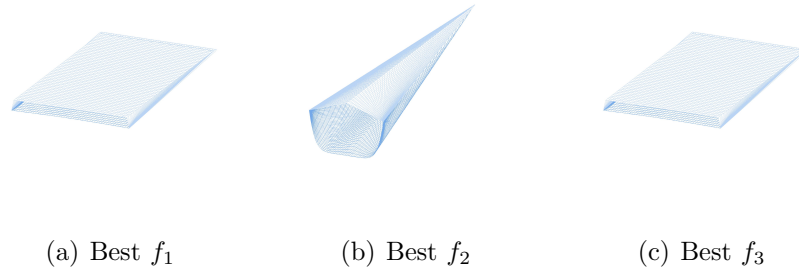

(a) Best f_1 (b) Best f_2 (c) Best f_3

Figure 6.2: Extreme Pareto-optimal point vehicle designs with best f_1, f_2, f_3 values for the infinitely sharp leading edge baseline case (isometric views).

The wedge-like shape is optimal for maximizing the lift-to-drag ratio because it best aligns the resultant pressure force vector with the z-axis. The lower surface has little curvature and has a small wedge angle θ, therefore the force components in the drag and side force directions are minimal . The cone-like shape is the most volumetrically efficient shape in the design space, due to its rounded lower surface. As a cone-like shape becomes more wedge-like or flat, the volume-to-surface area ratio decreases.

The total moment force coefficient is comprised of a both a pressure and viscous component. For the wedge-like and cone-like shapes, it was found that the moment coefficient is dominated by the pressure force component. Therefore, the best design for f_3 was driven by the moments created by pressure forces. The wedge-like design was best because it minimizes the pressure induced pitching moment and balances

any pressure induced roll or yaw moments due to symmetry. The wedge shape has the minimal pitching moment because is has a small wedge angle at all spanwise locations, thus minimizing the pressure force on the lower surface of the vehicle.

The extreme Pareto-optimal designs for the infinitely sharp baseline case show that a trade-off exists between wedge-like and cone-like shapes. If a design aims solely for a high lift-to-drag ratio and a low moment coefficient, it will have poor a volumetric efficiency. For example, the wedge-like optimum shape for the design point in this study had a high lift-to-drag ratio and low moment coefficient magnitude of about 8 and 2.8×10^{-5}, respectively, yet suffered in volumetric efficiency with a value of about 0.2. Any gain in volumetric efficiency will come at the cost of the performance (lift-drag-ratio) and trimmability (moment coefficient). In this study, the cone-like shape had approximately three times the volumetric efficiency of the wedge-like shape, yet saw about a 75% reduction in lift-to-drag ratio and a jump in moment coefficient magnitude of four orders of magnitude compared to the wedge-like counterpart.

The L^2-norm optimum design is the design which equally balances the three objectives. The L^2-norm design for the infinitely sharp baseline case is shown in Figure 6.3. The objective function values and design vector are listed in Tables 6.1 and 6.2. Geometrically, the L^2-norm design is a hybrid shape balancing both wedge-like and cone-like shape characteristics. The design vector values reinforce this balance. The value of n is 0.127. This balance between zero and one keeps the long slender shape of the cone while still flattening the shape out. The θ and δ values are about 5.956°. and 4.9° respectively. This produces a slightly convex

shape of a moderate wedge angle. The L²-norm shape exhibits a lift-to-drag ratio of 6.185, η of 0.458, and moment coefficient magnitude of 1.451×10^{-3}. This amounts to approximately twice the volumetric efficiency of the wedge-like shape with a 25% reduction in lift-to-drag ratio and a two orders of magnitude jump in moment coefficient magnitude compared to the wedge-like shape. These performance and trimmability characteristics are the values of minimum compromise between the three objectives.
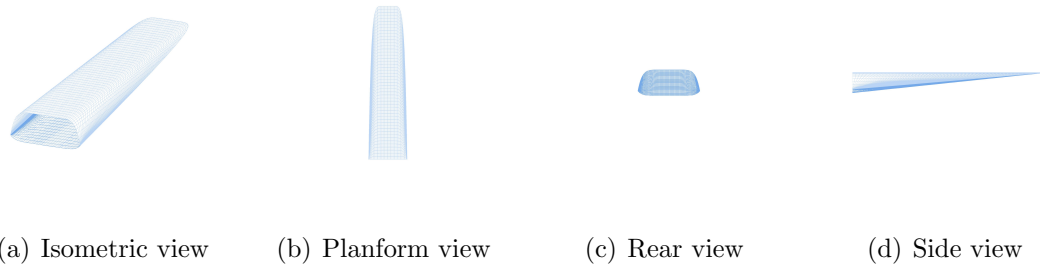

(a) Isometric view   (b) Planform view   (c) Rear view   (d) Side view

Figure 6.3: L²-norm Pareto-optimal point vehicle design for the infinitely sharp leading edge baseline case.

The current work found that a wedge-like shape produces a maximum lift-to-drag ratio vehicle. This was verified by comparing the results of the current study to the results found by Starkey [30]. Starkey found a wedge-like optimum shape when using a single-objective optimization study to find the maximum value of lift-to-drag ratio multiplied by internal volume. Starkey also optimized for maximum lift-to-drag ratio multiplied by volumetric efficiency. This objective function is analogous to a L²-norm optimum between lift-to-drag ratio and volumetric efficiency. Therefore, it is no surprise that the L²-norm optimum shape in the current work exhibits similar characteristics to the single-objective optimum in Starkey's work.

Table 6.1: Pareto-optimal point objective function values for the infinitely sharp leading baseline edge case.

Pareto-optimal point	$\frac{Lift}{Drag}$	η	$\|\vec{C}_{M_{CG,tot}}\|$	Figure
Best f_1	8.132	0.229	2.932×10^{-5}	Figure 6.2(a)
Best f_2	1.966	0.633	4.031×10^{-2}	Figure 6.2(b)
Best f_3	8.131	0.229	2.767×10^{-5}	Figure 6.2(c)
L^2-norm	6.185	0.458	1.451×10^{-3}	Figure 6.3

Table 6.2: Pareto-optimal point design vector values for the infinitely sharp leading edge baseline case.

Pareto-optimal point	n	m	θ (deg)	δ (deg)	L (ft)	w (ft)	Figure
Best f_1	0.003	0.668	2.702	2.953	190.405	112.567	Figure 6.2(a)
Best f_2	1.000	0.146	9.997	2.430	205.757	52.975	Figure 6.2(b)
Best f_3	0.001	0.664	2.701	2.954	190.405	112.568	Figure 6.2(c)
L^2-norm	0.127	0.121	5.956	4.900	206.040	51.771	Figure 6.3

6.1.2 Blunted Case

The extreme Pareto-optimal design results for the blunted baseline case, shown in Figure 6.4, follow the same patterns as the sharp case. The designs are either wedge-like or cone-like for the same corresponding best f_1, f_2, and f_3 objectives. The best f_1 design for the blunted case is not as wedge-like as what was found in the sharp case. However, this not a product of adding a blunted leading edge. A fully wedge-like extreme Pareto-optimal shape is possible with a blunted leading edge because it was found for the best f_1 blunted shape in Section 6.2.1 (Figure 6.13(a)). The optimization simulations in Section 6.2.1 were run for more generations and the Pareto-optimal designs had more time to progress towards the wedge-like extreme design. If given more generations, the best f_1 blunted baseline design would match the wedge shapes in Section 6.2.1 and the previous section (Figures 6.13(a) and 6.2(a)). The maximum possible lift-to-drag ratio for the best blunted f_1 shape does however differ from the sharp case. Blunting the leading edge adds more pressure drag and decreases the lift-to-drag ratio by about 9%. The optimum design therefore tries to mitigate the loss of lift-to-drag ratio by decreasing the separation distance d to its minimum possible value.

The best f_2 result is the same as the sharp case, yet now the optimizer gains some volumetric efficiency (an increase of about 10%) by maximizing the separation distance to its maximum possible value. This shape is also the best f_4 design because the maximum value of d gives a minimum peak heat flux on the leading edge. The resulting design for f_4 may show that minimizing peak heat flux does not drive the

121

design, and will always follow the best volumetrically efficient design. Future studies may want to also factor in a method of minimizing the total heat load on the leading edge.

The characteristics of the best f_3 and L^2-norm designs agree with the analysis presented in the infinitely sharp baseline results section. The blunted L^2-norm shape, shown in Figure 6.5, favors a more cone-like shape compared to the sharp L^2-norm shape. This is due to the inclusion of the f_4 objective function. The best f_4 shape is cone-like, which weights the L^2-norm more towards a cone-like shape. The corresponding objective function values and design vectors for the extreme Pareto-optimal designs and L^2-norm design are presented in Table 6.3 and Table 6.4.
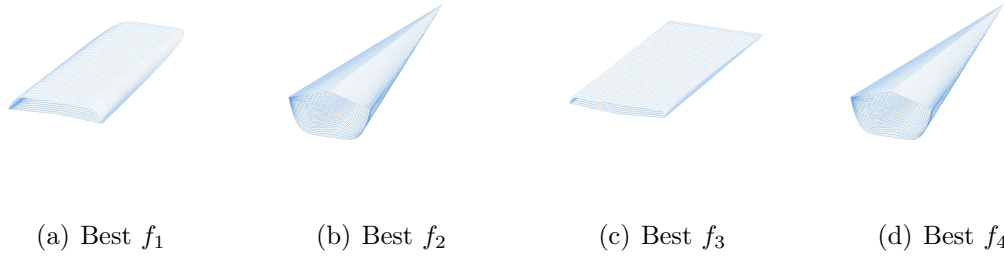

(a) Best f_1 (b) Best f_2 (c) Best f_3 (d) Best f_4

Figure 6.4: Extreme Pareto-optimal point vehicle designs with best f_1, f_2, f_3, f_4 values for the blunted leading edge baseline case (isometric views).

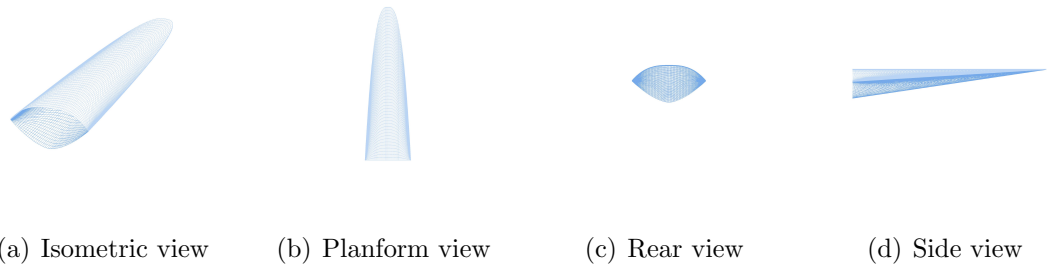(a) Isometric view   (b) Planform view   (c) Rear view   (d) Side view

Figure 6.5: L^2-norm Pareto-optimal point vehicle design for the blunted leading edge baseline case.

Table 6.3: Pareto-optimal point objective function values for the blunted leading edge baseline case.

Pareto-optimal point	$\frac{Lift}{Drag}$	η	$\|\vec{C}_{M_{CG,tot}}\|$	$max\,(q_w)$ (W/cm^2)	Figure
Best f_1	7.416	0.280	5.266×10^{-4}	346.067	Figure 6.4(a)
Best f_2	1.718	0.702	3.839×10^{-2}	39.385	Figure 6.4(b)
Best f_3	3.332	0.241	1.295×10^{-5}	85.438	Figure 6.4(c)
Best f_4	1.718	0.702	3.839×10^{-2}	39.385	Figure 6.4(d)
L^2-norm	4.458	0.535	5.162×10^{-3}	95.405	Figure 6.5

Table 6.4: Pareto-optimal point design vector values for the blunted leading edge baseline case.

Pareto-optimal point	n	m	θ (deg)	δ (deg)	L (ft)	w (ft)	d (ft)	Figure
Best f_1	0.115	0.869	2.901	3.531	212.036	88.984	0.021	Figure 6.4(a)
Best f_2	0.984	0.173	9.989	2.653	165.170	53.158	1.640	Figure 6.4(b)
Best f_3	0.003	0.849	2.368	1.501	212.572	90.555	0.352	Figure 6.4(c)
Best f_4	0.984	0.173	9.989	2.653	165.170	53.158	1.640	Figure 6.4(d)
L^2-norm	0.364	0.608	8.417	3.545	197.916	59.252	0.282	Figure 6.5

6.2 Optimal Geometries under Asymmetric Boundary-Layer Conditions

6.2.1 Multi-Objective Results

The extreme Pareto-optimal designs for f_1, f_2, and f_4 for all of the ABLT influenced optimization cases are very similar to the designs found for the baseline cases. Both the wedge-like and cone-like shapes were found as extreme Pareto-optimal designs and the analysis and discussion for this section parallels that of Section 6.1. The analyses for the L^2-norm designs in Section 6.1 are also applicable in this section. In lieu of these similarities, the following section will only focus on the f_3 extreme Pareto-optimal designs and the influence of an isolated disturbance and asymmetric boundary-layer.

6.2.1.1 Infinitely Sharp Case

Minimizing f_3 under the influence of an ABLT event aims to minimize the change in the magnitude of the moment vector due to an asymmetric boundary-layer at multiple possible spanwise locations. Subtracting the moment vector magnitude for a design without a turbulence wedge from the moment vector magnitude for a design with a turbulence wedge isolates the viscous effect on vehicle controllability. In other words, the moments due to pressure are subtracted out.

To aid in the analysis of the results, the best and *worst* f_3 designs are given in Figures 6.6(c) and 6.6(d). The design that is most robust to spanwise turbulence

124

wedge disturbances is the small wedge angle wedge-like geometry. The wedge-like geometry had a f_3 value of 1.453×10^{-7}. The design that is most sensitive to the presence of a turbulence wedge is a cone-like shape. The cone-like and wedge-like shapes illustrate the trade-off that exists between volumetric efficiency, lift-to-drag ratio, and controllability. The cone-like shape had 3.5 times the volumetric efficiency of the wedge-like shape, yet compromised with an approximate 75% decrease in lift-to-drag ratio and one full order of magnitude jump in the value of f_3 (the controllability factor) when compared to the wedge-like counterpart. Note that the base plane cross section of the cone-like shape differs from the extreme cone-like shape baseline results. The worst f_3 shape for the ABLT case has a more rounded, circular top surface ($n \approx 0.5$), whereas the baseline design has a flatter upper surface ($n \approx 1$).

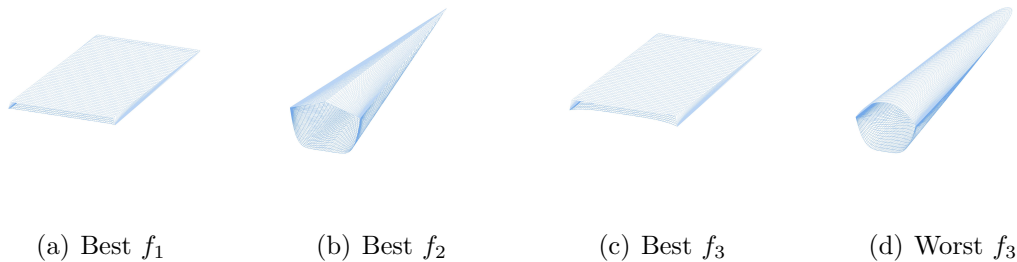(a) Best f_1 (b) Best f_2 (c) Best f_3 (d) Worst f_3

Figure 6.6: Extreme Pareto-optimal point vehicle designs with best f_1, f_2, f_3, values and the design with the worst f_3 value for the ABLT infinitely sharp leading edge case (isometric views).

As expected, the L^2-norm design, seen in Figure 6.7, is a balance of these two extreme designs. The L^2-norm design had approximately 2.3 times the volumetric efficiency of the wedge-like shape with a 25% reduction in lift-to-drag ratio and

about five times (half an order of magnitude) the moment coefficient magnitude of the wedge-like shape.
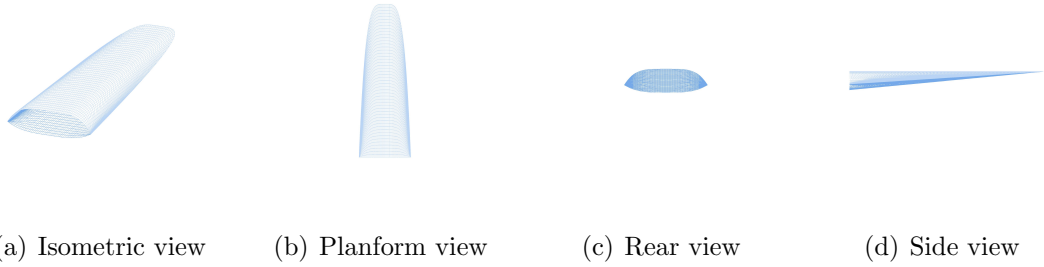

(a) Isometric view   (b) Planform view   (c) Rear view   (d) Side view

Figure 6.7: L^2-norm Pareto-optimal point vehicle design for the ABLT infinitely sharp leading edge case.

An understanding of why these shapes are the best, worst, and L^2-norm designs with respect to f_3 requires both a qualitative and quantitative analysis. A qualitative look at how the turbulence wedge geometrically covers the vehicles is necessary to visualize the effect on the moments. Views of the turbulence wedge as applied to these the best, worst, and L^2-norm Pareto-optimal designs as a function of p are shown in Figures 6.8, 6.9, and 6.10. The corresponding quantitative look of the spanwise effects of the turbulence wedge is given as the spanwise distribution of $F_{3,scaled}$, shown in Figure 6.11. Note, the figure presents the robust counterpart function F not the original function f (see Equation 5.21 in Section 5.3.1).
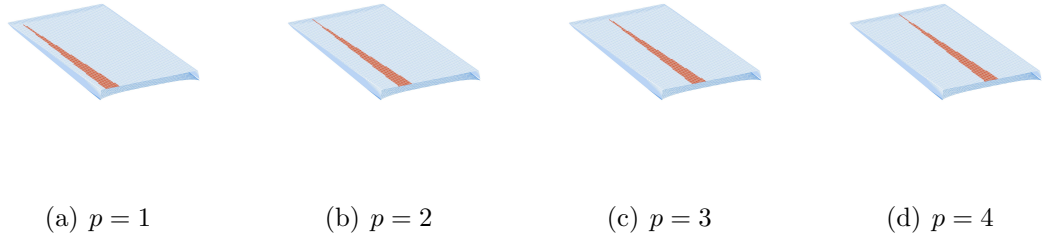
(a) $p = 1$ (b) $p = 2$ (c) $p = 3$ (d) $p = 4$

Figure 6.8: Isometric views of the best f_3 Pareto-optimal design with a spanwise disturbance at $p = 1, 2, 3,$ and 4 for the ABLT infinitely sharp case.
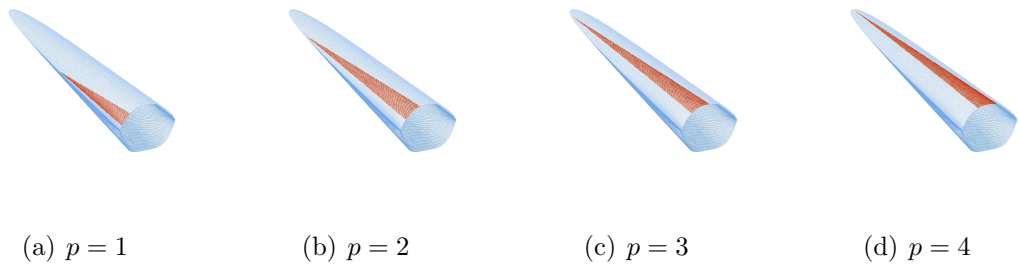

(a) $p = 1$ (b) $p = 2$ (c) $p = 3$ (d) $p = 4$

Figure 6.9: Isometric views of the worst f_3 Pareto-optimal design with a spanwise disturbance at $p = 1, 2, 3,$ and 4 for the ABLT infinitely sharp case.
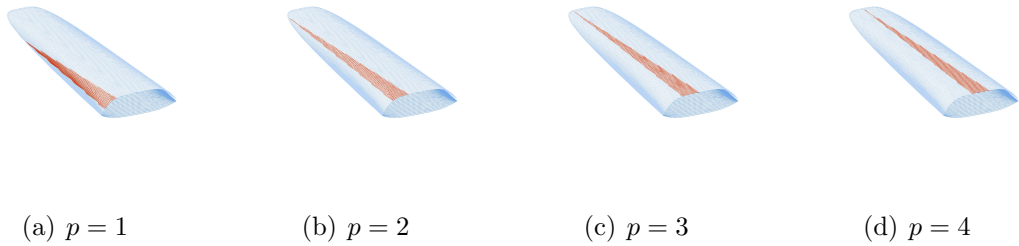

(a) $p = 1$ (b) $p = 2$ (c) $p = 3$ (d) $p = 4$

Figure 6.10: Isometric views of L^2-norm Pareto-optimal design with a spanwise disturbance at $p = 1, 2, 3,$ and 4 for the ABLT infinitely sharp case.

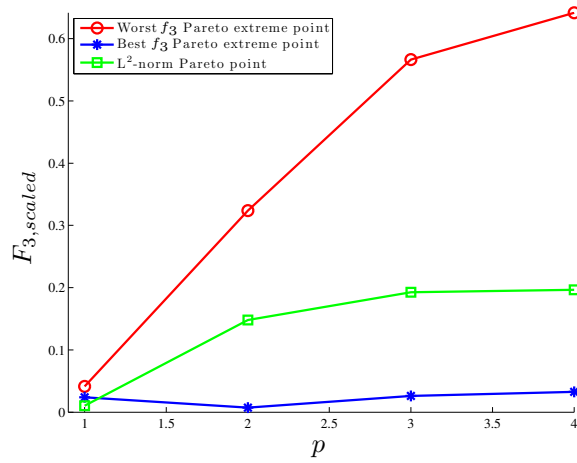Figure 6.11: Spanwise distribution of $F_{3,scaled}$ for best, worst, and L^2-norm vehicle designs for the ABLT infinitely sharp leading edge case.

The wedge-like shape keeps the spanwise value of $F_{3,scaled}$ at a low value, fluctuating only slightly as p goes from 1 to 4. The cone-like shape starts at a low value similar to the wedge-like shape at $p = 1$. But as the turbulence wedge approaches the center of the vehicle, the value of $F_{3,scaled}$ increases monotonically. The roles of the three components to F_3 (roll, pitch, and yaw) are important in understanding why the wedge and cone shapes produce these curves. The x component, or roll component, is zero due to the assumption that the direction of the shear force vector is purely in the x direction (see Chapter 2). The y and z components to F_3 are the pitch and yaw components, respectively. The spanwise distributions of the y and z components of F_3 are shown in Figure 6.12.

At $p = 4$, the moment created by the turbulence wedge is purely a pitching moment. Since the wedge-like (best) design has a very small moment arm in the z direction, the pitching moment value is low. Conversely, the cone-like (worst) design has a much larger moment arm, so the pitching moment value is large. As the turbulence wedge progresses away from the centerline, the moment arm for the wedge-like vehicle stays constant, so the pitching moment stays the same. The moment arm for the cone-like vehicle decreases as the wedge moves away from the centerline and the area covered by the turbulence wedge becomes smaller. Therefore, the cone-like design shows a decrease in pitching moment as p goes from 4 to 1. This effect is shown by the curves in Figure 6.12(a).

The yaw moment (Figure 6.12(b)) for both the best and worst designs start at zero and becomes more negative as the turbulence wedge moves away from the centerline. This is due to the increase in the moment arm in the y direction. The area

covered by the turbulence wedge for the wedge-like (best) design remains constant, so the yaw moment is only affected by the linear increase in moment arm length. Consequently, the yaw moment becomes more negative nearly linearly as p goes from 4 to 1. The area covered by the turbulence wedge for the cone-like (worst) design decreases as p goes from 4 to 1 and eventually counteracts the increase in moment due to an increasing moment arm length. This is shown by the decrease from $p = 4$ to $p = 2$ then increase from $p = 2$ to $p = 1$ in the worst design curve.

For the Pareto-optimal shapes, the moment vector without a turbulence wedge points solely in the y direction (As described in the baseline results section). Consequently, relatively small changes to the moment vector's z component will change the direction of the vector, but only weakly affect the change in magnitude of the vector. In comparison, relatively small changes in the y component will change the direction of the vector, but strongly affect the change in magnitude. F_3 was defined as the change in the *magnitude* of the moment vector due to a turbulence wedge. Changes in *direction* do not affect the objective function value. Therefore, the F_3 y component curves dictate which design is optimum for objective function f_3. That is why the trends in Figure 6.11 closely match those in Figure 6.12(a).

The best designs for f_1 and f_2 match the analysis given for the baseline case. For reference, the tables containing the Pareto-optimal point information is given below. Table 6.5 gives the objective function values and Table 6.6 gives the design vector values.
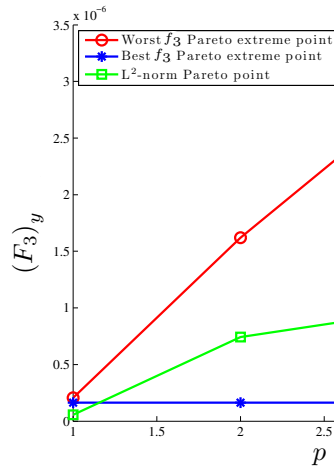
(a) F_3 y component (pitching moment) vs. p
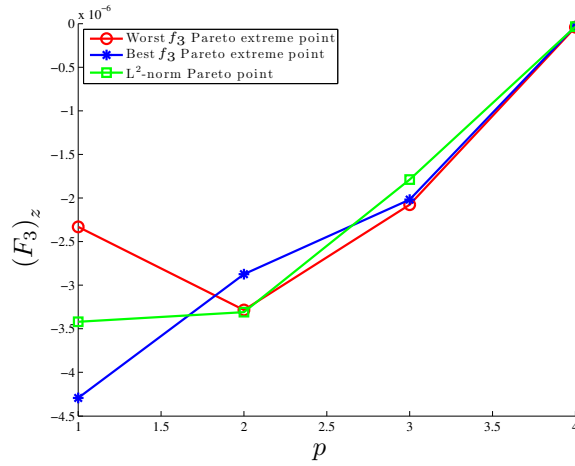
(b) F_3 z component (yaw moment) vs. p

Figure 6.12: Spanwise distribution of the y and z components of F_3 for best, worst, and L^2-norm vehicle designs for the ABLT infinitely sharp leading edge case.

Table 6.5: Pareto-optimal point objective function values for the ABLT infinitely sharp leading edge case.

Pareto-optimal point	$\frac{Lift}{Drag}$	η	f_3	Figure
Best f_1	8.633	0.178	1.453×10^{-7}	Figure 6.6(a)
Best f_2	1.958	0.633	1.591×10^{-6}	Figure 6.6(b)
Best f_3	8.474	0.190	1.121×10^{-7}	Figure 6.6(c)
Worst f_3	4.276	0.609	1.967×10^{-6}	Figure 6.6(d)
L^2-norm	6.472	0.412	6.850×10^{-7}	Figure 6.7

Table 6.6: Pareto-optimal point design vector values for the ABLT infinitely sharp leading edge case.

Pareto-optimal point	n	m	θ (deg)	δ (deg)	L (ft)	w (ft)	Figure
Best f_1	0.007	0.038	1.789	1.987	219.867	119.847	Figure 6.6(a)
Best f_2	0.999	0.148	10.000	2.291	197.418	50.940	Figure 6.6(b)
Best f_3	0.008	0.238	1.813	2.968	216.277	119.846	Figure 6.6(c)
Worst f_3	0.431	0.249	9.754	3.772	201.142	43.620	Figure 6.6(d)
L^2-norm	0.236	0.284	5.398	3.695	206.558	69.684	Figure 6.7

6.2.1.2 Blunted Case

Effects of the blunted leading edge for the ABLT case parallel that of the baseline case. The analysis of the blunt leading edge results in the baseline case should be consulted to understand the results in this section. The analysis of f_3 for the blunted ABLT influenced case is analogous to the discussion for the infinitely sharp case. The ABLT infinitely sharp case section can be consulted to understand the f_3 results in this section. The tables and figures below are provided for reference.
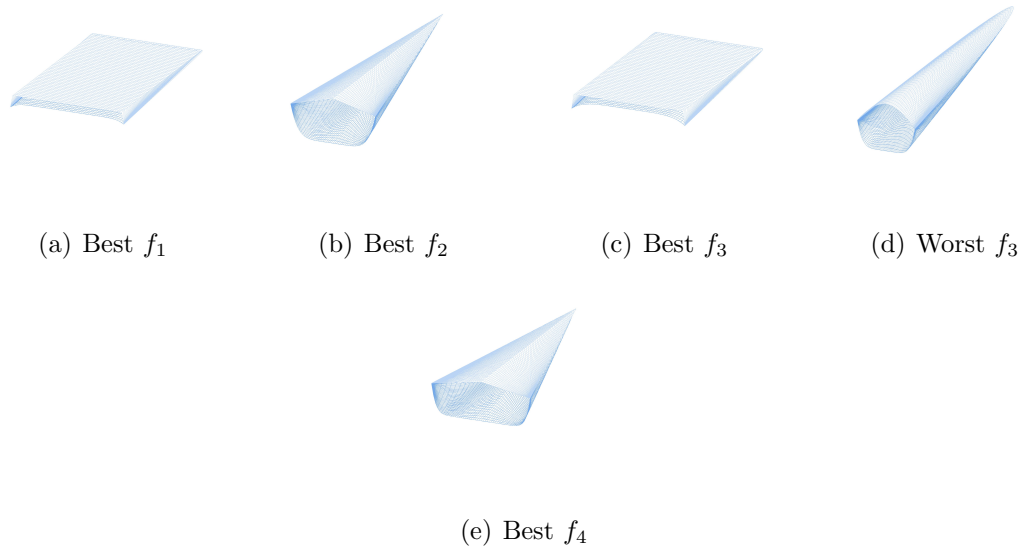
(a) Best f_1 (b) Best f_2 (c) Best f_3 (d) Worst f_3

(e) Best f_4

Figure 6.13: Extreme Pareto-optimal point vehicle designs with best f_1, f_2, f_3, f_4 values and the design with the worst f_3 value for the ABLT blunted leading edge case (isometric views).

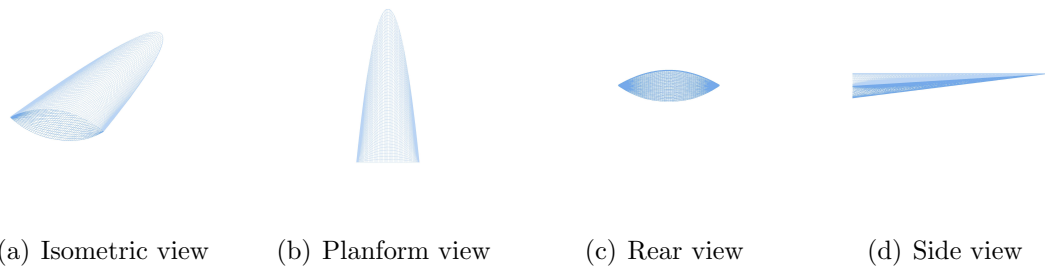(a) Isometric view   (b) Planform view   (c) Rear view   (d) Side view

Figure 6.14: L^2-norm Pareto-optimal point vehicle design for the ABLT blunted leading edge case.

Table 6.7: Pareto-optimal point objective function values for the ABLT blunted leading edge case.

Pareto-optimal point	$\frac{Lift}{Drag}$	η	f_3	$max(q_w)$ (W/cm^2)	Figure
Best f_1	7.783	0.202	1.257×10^{-7}	393.377	Figure 6.13(a)
Best f_2	1.643	0.703	1.199×10^{-6}	39.369	Figure 6.13(b)
Best f_3	5.991	0.201	9.748×10^{-8}	169.597	Figure 6.13(c)
Worst f_3	3.407	0.626	1.787×10^{-6}	80.123	Figure 6.13(d)
Best f_4	1.290	0.691	9.235×10^{-7}	39.340	Figure 6.13(e)
L^2-norm	4.224	0.488	6.847×10^{-7}	88.030	Figure 6.14

Table 6.8: Pareto-optimal point design vector values for the ABLT blunted leading edge case.

Pareto-optimal point	n	m	θ (deg)	δ (deg)	L (ft)	w (ft)	d (ft)	Figure
Best f_1	0.005	0.110	2.249	3.599	190.759	119.680	0.017	Figure 6.13(a)
Best f_2	1.000	0.164	10.000	2.581	160.484	55.160	1.640	Figure 6.13(b)
Best f_3	0.010	0.186	1.885	4.376	189.785	118.119	0.089	Figure 6.13(c)
Worst f_3	0.563	0.164	9.118	4.004	207.788	42.260	0.399	Figure 6.13(d)
Best f_4	1.000	0.083	9.999	2.284	150.761	69.720	1.640	Figure 6.13(e)
L^2-norm	0.504	0.445	7.074	3.468	188.601	77.453	0.331	Figure 6.14

6.2.2   Robust Optimization Results

Section 6.2.2 provides all the results from the four robust optimization problems. Generation histories and optimum design vectors are provided and discussed from an optimization perspective. Section 6.2.2.5 draws comparisons between the robust optimum designs, resulting hypersonic vehicle shapes, and the corresponding method effectiveness and expense. Section 6.2.2.6 provides an example of how the robust MOGA method has the unique capability to provide the designer with more information about the design space.

6.2.2.1   Robust Regularization Results

Figure 6.15 provides a generation history plot for the robust regularization-based method. The figure plots the minimum F_I value found in the population at a given generation number. This value decreases from generation to generation, eventually leveling off. After about generation 250, little to no improvement in the objective function is made.

It is reasonable to say (without any strict convergence criterion) that the optimization problem converges at generation 250. The optimum design vector $\vec{x}^*$ is the value of $\vec{x}$ which gives the minimum value of F_I at generation 250. The value of $\vec{x}^*$ for the robust regularization-based method was the following:

$$\vec{x}^* = \begin{bmatrix} 0.05 & 0.999 & 4.414 & 4.015 & 146.424 & 120.0 \end{bmatrix} . \tag{6.2}$$

For the implementation defined in Equation 5.25, the optimum result was found after 137,500 function evaluations.
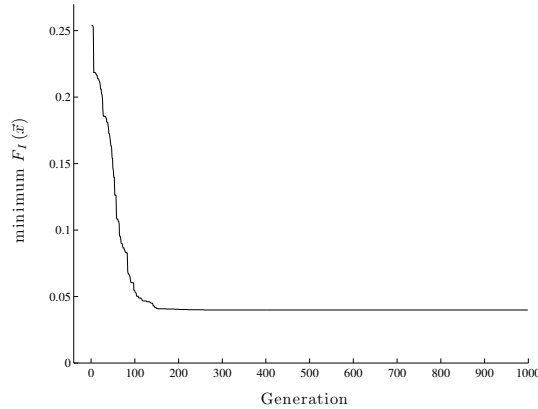

Figure 6.15: Robust regularization-based method generation history.
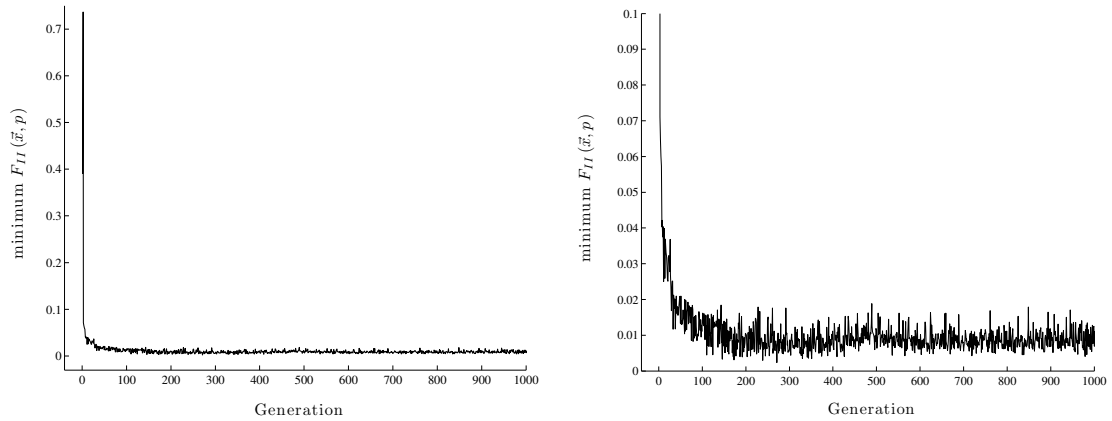
6.2.2.2 Explicit Averaging Results

Figure 6.16 provides a generation history plot for the explicit averaging method using Monte Carlo integration. The figure plots the minimum F_{II} value found in the population at a given generation number. Due to the nature of the sampling technique in this method, the plot is noisy; F_{II} doesn't monotonically decrease with increasing generation number. Nonetheless, Figure 6.16 shows a rapid improvement in the objective function value which quickly levels off at about generation 100 . The value continues to decrease until somewhere between generation 200 and 300. After this, improvement in the objective function value is indistinguishable through the noise. It will be assumed that the optimum design vector was found at generation 250.

The optimum design vector $\vec{x}^*$ is the value of $\vec{x}$ which gives the minimum value of F_{II} at generation 250. The value of $\vec{x}^*$ for the explicit averaging method was

$$\vec{x}^* = \begin{bmatrix} 0.999 & 0.903 & 8.559 & 3.16 & 176.631 & 120.0 \end{bmatrix} . \tag{6.3}$$

For the implementation defined in Equation 5.26, the optimum result was found after 125,000 function evaluations.

(a) Explicit averaging generation history.　(b) Explicit averaging generation history (zoomed in).

Figure 6.16: Explicit averaging generation history.
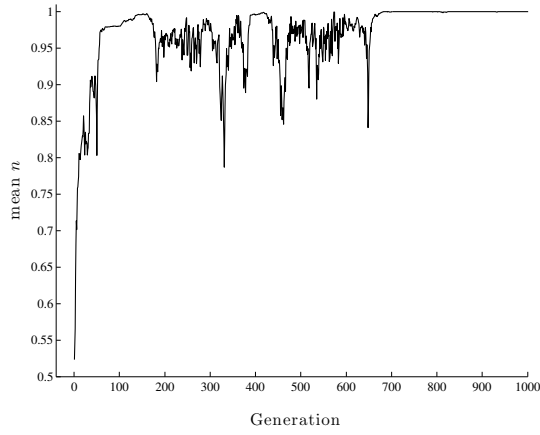
6.2.2.3　Perturbation Results

The nature of the perturbation method makes generation histories based on F_{III} difficult to interpret. The value of p is generation dependent, meaning the plot would be very noisy and may potentially mask any convergence trends. Tsutsui et al. [72, 73] determined convergence by plotting the mean value of the design variable(s) over the population at each generation. Figure 6.17 shows these trends for the optimization problem in this study. Each design variable fluctuates with

different magnitudes and frequencies as the generations progress. Eventually, each of the design variables finds a nearly constant value and no longer changes with subsequent generations. Once all of the variables reach this condition, the problem has converged to a solution. From Figure 6.17, convergence was found to occur at about generation 750.

The optimum design vector $\vec{x}^*$ was taken to be the vector $\vec{x}$ in the population which has the smallest departure from the mean value at generation 750. The value of $\vec{x}^*$ for the perturbation method was

$$\vec{x}^* = \begin{bmatrix} 0.999 & 0.999 & 5.578 & 1.671 & 214.01 & 119.934 \end{bmatrix} . \tag{6.4}$$
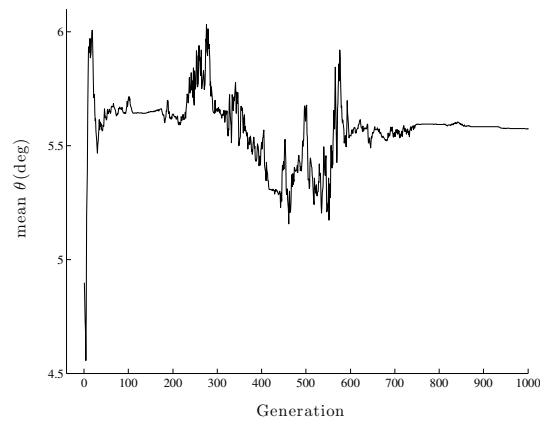
For the implementation defined in Equation 5.27, the optimum result was found after 37,500 function evaluations.
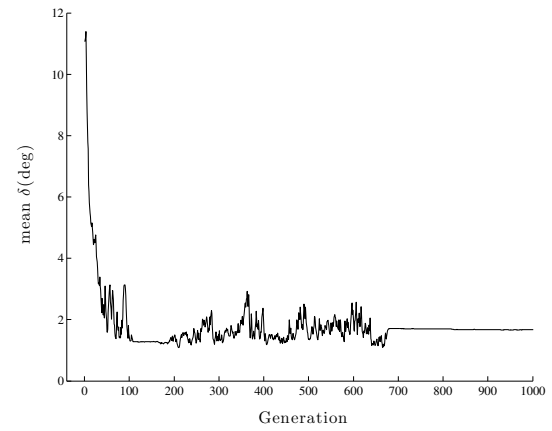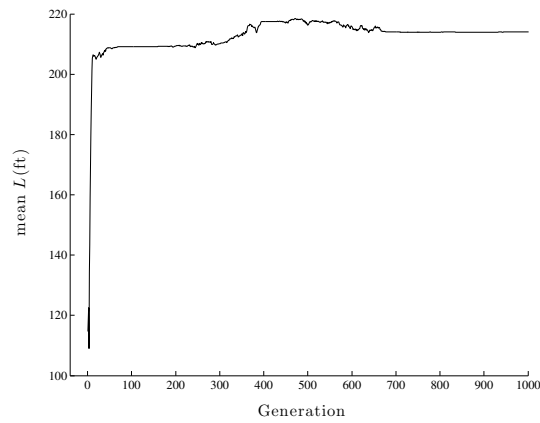
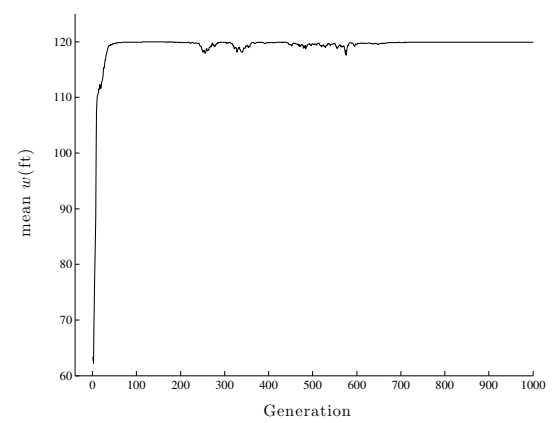(a) Mean value of n
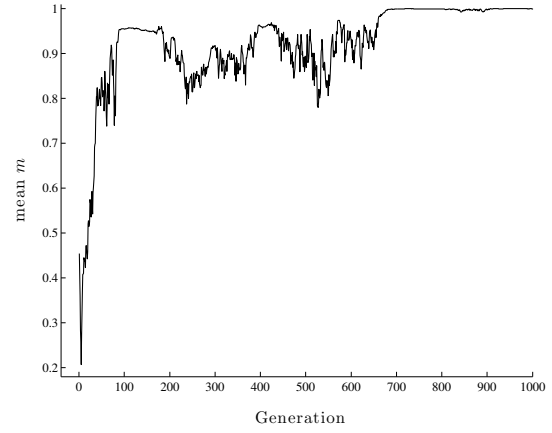
(b) Mean value of m

(c) Mean value of θ

(d) Mean value of δ

(e) Mean value of L

(f) Mean value of w

Figure 6.17: Generation history of the mean $\vec{x}$ values over the population for the perturbation method.

6.2.2.4 Robust MOGA Results

As discussed in Section 4.2.3.2, convergence of the robust MOGA optimization method is measured using Equation 4.10. Figure 6.18 plots the average ΔPM over the previous 10 generations as a function of current generation number. Starting at generation 10, the average value of ΔPM is about 52. As generations progress, the average value of ΔPM decreases rapidly. With increasing generation number the average value of ΔPM levels off, between generation 100 and 500, to a value which fluctuates between 0.0 and 0.5. Over the next 1500 generations, these fluctuations slowly die out. Typical values of ΔPM which correspond to a particular level of accuracy in the true Pareto-optimal set approximation is not fully understood, yet a preliminary analysis on the convergence trends and its link to accuracy, quality, and speed of the optimization process is given in Section 4.4. Overall, a converging trend is observed in Figure 6.18.
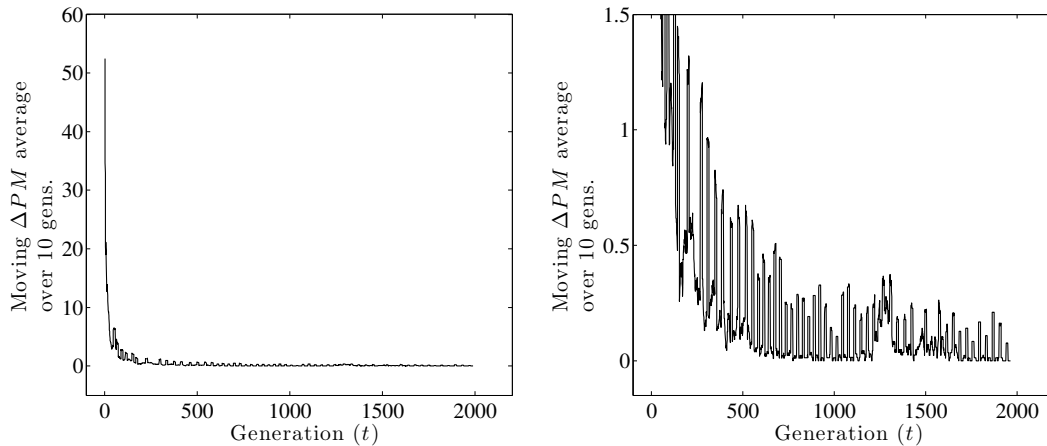
(a) Full generation history.

(b) Generation history zoomed in.

Figure 6.18: Robust MOGA mean ΔPM generation history.

In attempt to deliver results from a simulation which is as converged as possible, the true Pareto-optimal solution set will be taken as the approximation at generation 2000 ($\hat{x}_{2000}$). The set of Pareto-optimal solutions at generation 2000 contains 96 individuals in the population. For each individual in the Pareto-optimal set, the mean value of F_{IV_1} through F_{IV_5} was calculated over the 2000 generations (i.e., $\langle F_{IV_m}(\vec{x}) \rangle_t$ seen in Equation 4.11). The mean objective function values, when plotted in objective function space, form the Pareto-optimal front.

Figure 6.19 shows the value of $\langle F_{IV_2}(\vec{x}) \rangle_t$ vs. the value of $\langle F_{IV_1}(\vec{x}) \rangle_t$ for each of the 96 Pareto-optimal solutions. From this plot, it is seen that these two objective functions are non-competing. Therefore, only one of these two functions needs to be plotted in order to form the Pareto-optimal front.
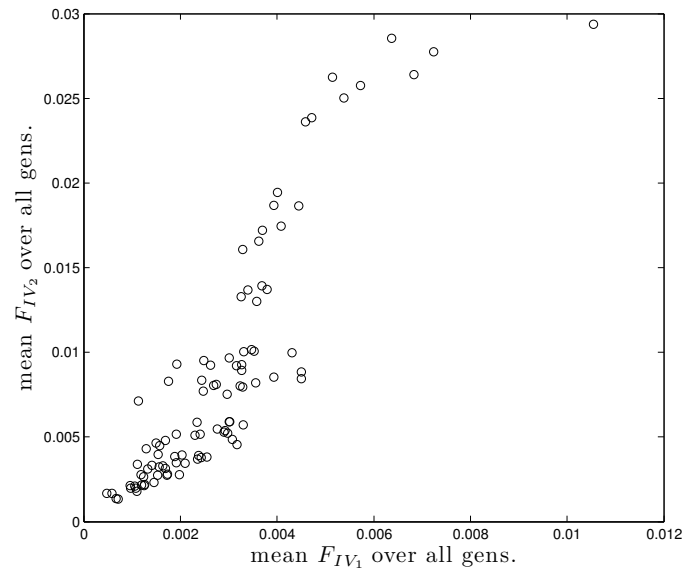

Figure 6.19: Average F_{IV_2} vs. average F_{IV_1} over all generations for each of the 96 Pareto-optimal solutions.

The Pareto-optimal front in four dimensions is shown in Figure 6.20. The x-, y-, and z-axis in the plot are represented by $\langle F_{IV_1}(\vec{x})\rangle_t$, $\langle F_{IV_3}(\vec{x})\rangle_t$, and $\langle F_{IV_4}(\vec{x})\rangle_t$, respectively. The value of $\langle F_{IV_5}(\vec{x})\rangle_t$ is represented by color. To gain a better feel and understanding for the four-dimensional Pareto-optimal hypersurface, three-dimensional projections of Figure 6.20 is provided in Figure 6.21.
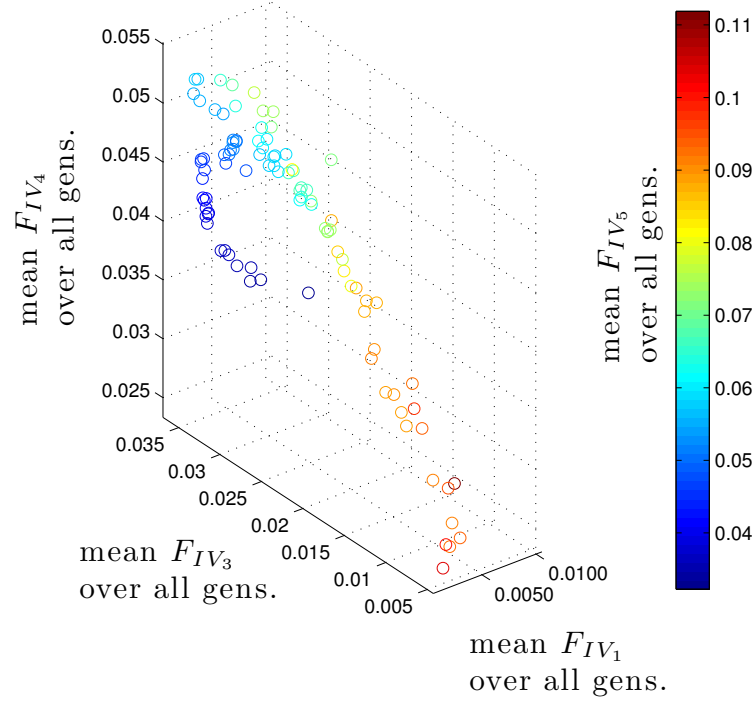
Figure 6.20: Four-dimensional Pareto-optimal front.

Robust regularization and explicit averaging equivalent solutions can be picked out of the set of Pareto-optimal solutions using Equation 4.11 and Equation 4.13, respectively. The resulting optimum design vectors using these equations were the following:

$$\vec{x}_{rr}^* = \begin{bmatrix} 0.113 & 0.793 & 3.688 & 1.656 & 184.8 & 119.314 \end{bmatrix}, \tag{6.5}$$

$$\vec{x}_{eap}^* = \begin{bmatrix} 0.989 & 0.351 & 5.596 & 2.421 & 188.763 & 119.875 \end{bmatrix}. \tag{6.6}$$

The robust MOGA formulation using the prescribed MOGA population settings required 500,000 function evaluations after 2000 generations and resulted in 96 different optimum design vectors.

Note, this is not necessarily an "apples to apple" comparison, when comparing the number of total function evaluations for each method. The implementation and convergence criterion greatly affects this value. The main purpose of Section 6.2.2 was to compare the resulting robust optimum vehicle designs from each method. The given total number of function evaluations for each method here is given in an attempt to be concise. The efficiency and convergence aspects of the proposed robust MOGA method is given in Section 4.4.
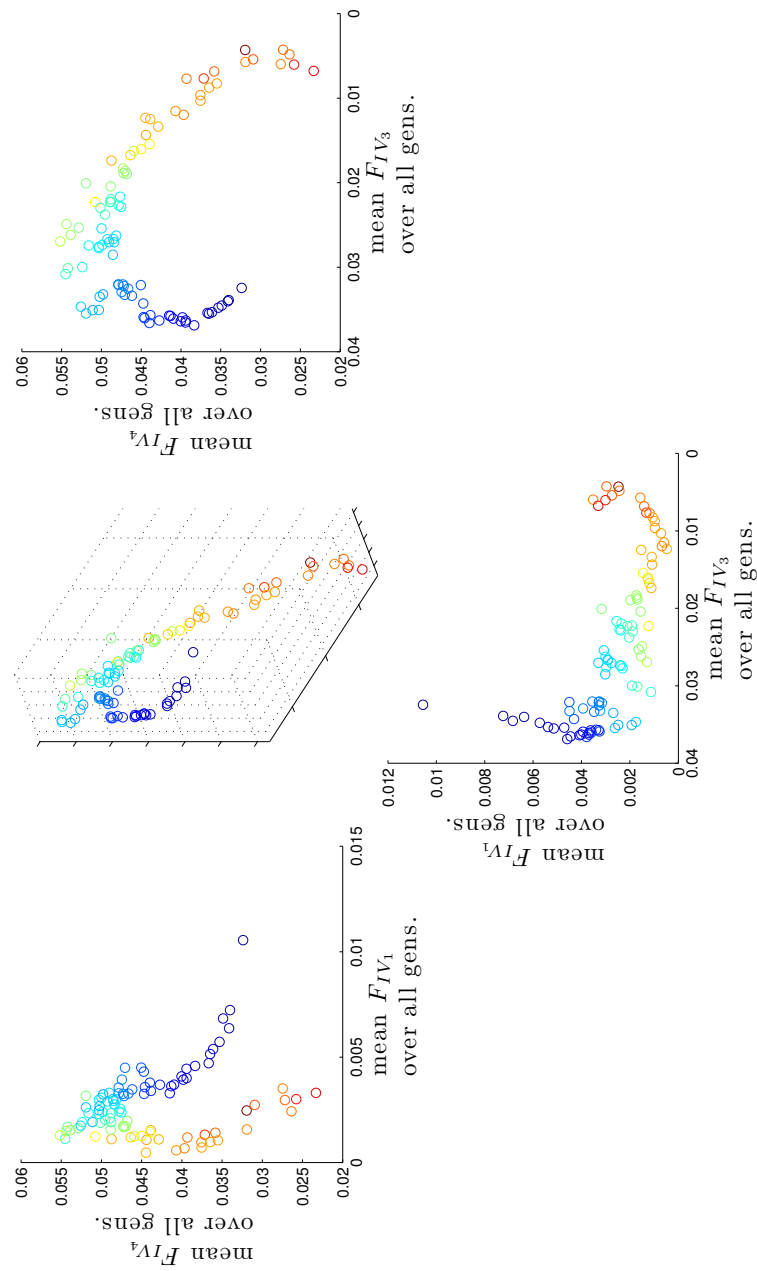
Figure 6.21: Three-dimensional projections of the Pareto-optimal front.

6.2.2.5 Result Comparisons and Vehicle Analysis

This section will aim at comparing the results from the different robust optimization methods. A focus will be set on analyzing the effectiveness of using a robust MOGA method coupled with post-optimality data handling techniques to pick preferred solutions from a set of Pareto-optimal solutions that match the philosophy of the other robust methods.

Table 6.9 provides a list of the robust optimum design vectors found by each method. The first two entries (above the dashed line) represent the results based on the worst-case scenario philosophy. The next three (below the dashed line) represent the results based off of the philosophy of minimizing the expected value of the original objective function over the uncertainty set. To aid in the analysis of the robust optimum design vectors, the robust optimum vehicle shapes are provided in Figure 6.22 through Figure 6.26. A few trends were common to all the robust optimum designs. The width parameter, w, of the robust optimum geometry for all cases is very close to the upper design limit of 120 feet. Although not shown in the table, the internal volume of each robust optimum design is near the lower limit constraint of 88,286 cubic feet. Also, all the shapes are convex, meaning $\theta > \delta$.

Table 6.9: Robust optimum designs.

Algorithm	$\vec{x}^*$					
	n	m	$\theta(\text{deg})$	$\delta(\text{deg})$	$L(\text{ft})$	$w(\text{ft})$
Robust regularization (Equation 5.25)	0.05	0.999	4.414	4.015	146.424	120.0
MOGA: robust reg. equivalent (Equations 4.30,4.13)	0.113	0.793	3.688	1.656	184.8	119.314
Aggregation: explicit averaging (Equation 5.26)	0.999	0.903	8.559	3.16	176.631	120.0
Aggregation: perturbation (Equation 5.27)	0.999	0.999	5.578	1.671	214.01	119.934
MOGA: aggregation equivalent (Equations 4.30,4.11)	0.989	0.351	5.596	2.421	188.763	119.875

The two solutions based on a worst-case scenario are characterized by small n values near or at the lower limit of 0.05 and large m values near or at the upper limit of 1.0. The two shapes are convex, but the values of θ are quite close to the value of δ. The optimal shape for the robust regularization-based method has a θ value that is only 0.4 degrees greater than δ. For the MOGA robust regularization equivalent solution, θ is about two degrees greater than δ. Figure 6.22 and Figure 6.23 show that these design vector qualities produce a flat, spatula or wedge-like shape.

(a) Isometric view   (b) Planform view   (c) Rear view   (d) Side view
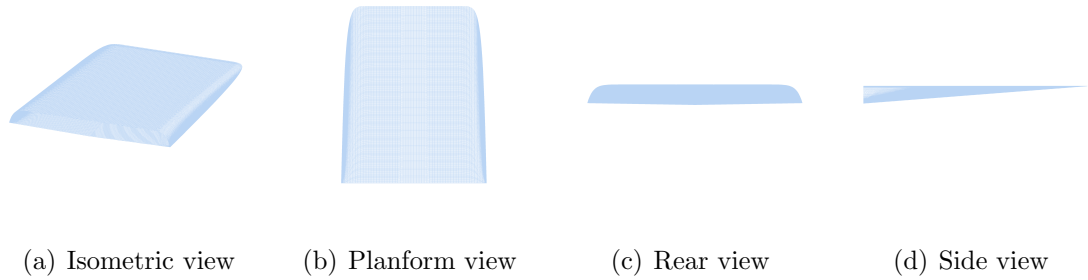
Figure 6.22: Optimal vehicle design for the robust regularization-based method.

(a) Isometric view   (b) Planform view   (c) Rear view   (d) Side view
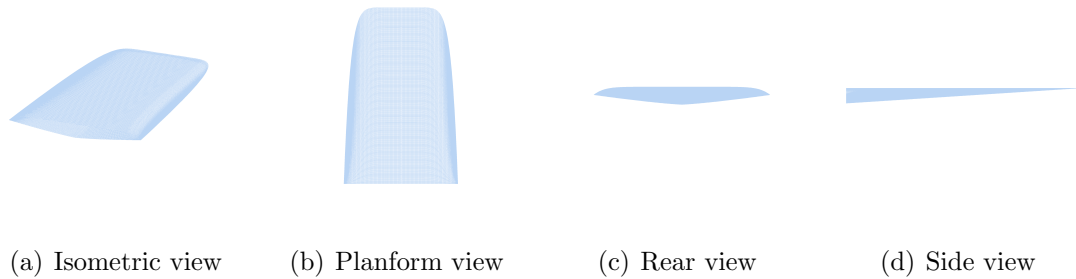
Figure 6.23: Optimal vehicle design for the robust MOGA method with robust regularization equivalent data handling.

The three minimized expected value robust optimum solutions are characterized by large values of n very close to the design variable upper limit of 1.0. This

produces a triangular planform shape. The explicit averaging and perturbation method optimum designs have large m values near the limit of 1.0. This produces a diamond shape cross section as seen in Figure 6.24 and Figure 6.25. The MOGA explicit averaging and perturbation equivalent solution has an optimum m value of 0.351. This value isn't quite are large as the other two. Yet judging from Figure 6.26, qualitatively the overall shape remains the same (namely a pyramidal shape). To gain a better understanding of the implications of this difference, a more quantitative look at the corresponding f values is needed.

(a) Isometric view   (b) Planform view   (c) Rear view   (d) Side view
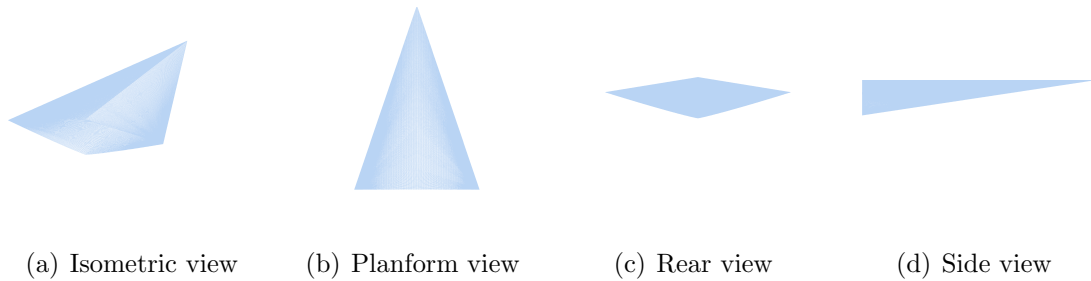
Figure 6.24: Optimal vehicle design for the explicit averaging method.

(a) Isometric view   (b) Planform view   (c) Rear view   (d) Side view
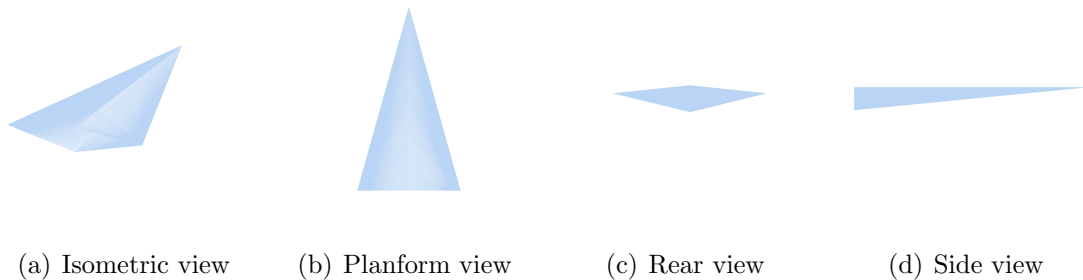
Figure 6.25: Optimal vehicle design for the perturbation method.

In order to quantitatively analyze each optimal design, values of f as a function of p are provided in Figure 6.27. The curve marked with square data points corresponds to the robust regularization-based method optimum design. The curve

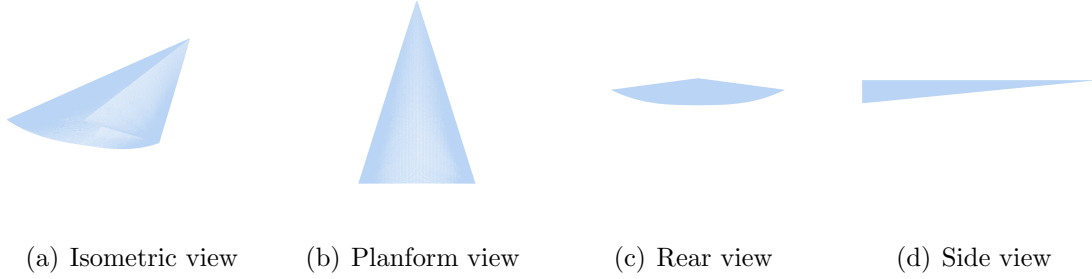(a) Isometric view   (b) Planform view   (c) Rear view   (d) Side view

Figure 6.26: Optimal vehicle design for the robust MOGA method with explicit averaging and perturbation equivalent data handling.

marked with downward pointing triangles is the MOGA robust regularization equivalent solution. These solutions are optimum based on a worst-case scenario philosophy. Therefore, they are the designs for which the max value of $f(\vec{x}, p)$ over all p values is minimized. This can be seen in the plot, where both maximum values of f on the curves are around 0.04 to 0.05. The trends of both curves exhibit similar characteristics. They are generally flat from $p = 0.5$ down to some value below $p = 0.25$. The curves then dip down to a value close to zero at about $p = 0.05$. Between $p = 0.0$ and $p = 0.05$ both curves exhibit a bump. The bump in the curve for the robust regularization-based method is significantly larger than the bump in the robust MOGA curve. This difference is due to the formulation of the robust regularization optimization problem in Equation 5.25, where p is sampled from a discrete set $\tilde{p}$ that only includes values 0.0, 0.05, 0.1, and so on. Therefore, p values between 0.0 and 0.05 do not get evaluated and are not taken into account when searching for an optimum design. The MOGA formulation however, accounts for p over the entire range $0.0 \leq p \leq 0.5$. The two curves show us that the MOGA-based answer is therefore more successful in minimizing the maximum value of f.
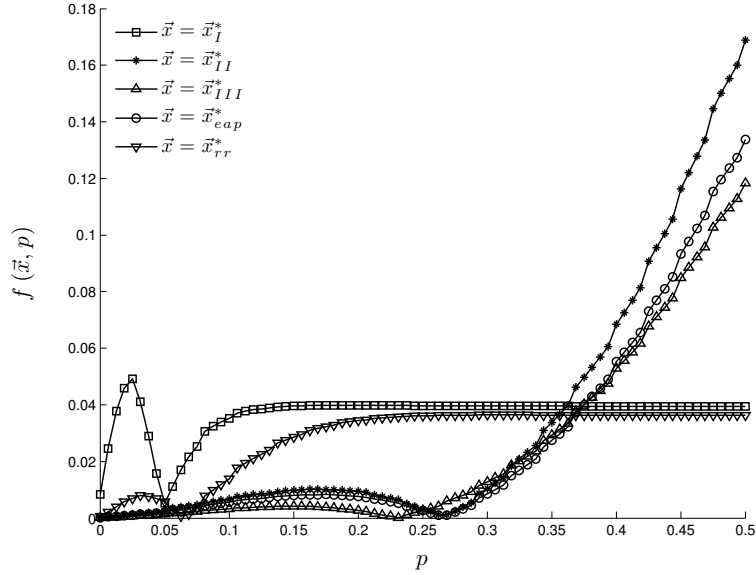
Figure 6.27: Original objective function values of each optimum design vector as a function of environmental parameter p.

The other three designs are represented by the curves which are marked with the star, upward pointing triangle, and circle data points. These methods are based off the philosophy of minimizing the expected value of f over uncertainty in p, which for this study was set to include all values in the range $0.0 \leq p \leq 0.5$. The optimum designs aim to minimize the area under the curves presented in Figure 6.27. The three curves for the methods based on an optimum expected value exhibit very similar characteristics. The overall trends are all the same. The area under the curve between $p = 0.0$ and $p = 0.25$ is almost reduced to zero. From $p = 0.25$ to $p = 0.5$ the curve increases monotonically from $f = 0.0$ to a value of f ranging between 0.12 and 0.17. The curve corresponding to the robust MOGA method after applying the data handling falls somewhere between the other two methods. From

this, it can be concluded that the slightly different value of m in the optimum design vector does not affect the overall goal of minimizing the expected value.

The vehicle designs that are wedge-like in shape are the designs that minimize the maximum change in moment coefficient due to an asymmetric boundary-layer transition occurring anywhere on the leading edge. The vehicle accomplishes this by distributing its internal volume equally along the spanwise direction, namely in a wedge shape. This means, an asymmetric viscous drag, occurring on the top surface the vehicle would contribute mostly to a change in yaw moment. The change in pitching moment is minimized by having a small wedge angle, bringing the top surface close to the center of gravity. From the analysis in Section 6.2.1, it was shown that changes in pitching moment are the main contributors to changes in f. Therefore, a wedge-like shape produces relatively constant value of f over different values of p.

The vehicle designs that are pyramidal in shape are the designs that minimize the expected change in moment coefficient due to an asymmetric boundary-layer transition, if the event is equally probable to happen at any spanwise location along the leading edge. The vehicle has a strongly swept leading edge. This renders a minimal area covered by the turbulence wedge for small p values. Also, the diamond shape cross section acts to minimize the moment arm with respect to the center of gravity for small p values. The internal volume of the vehicle is focused more towards the centerline of the body creating more distance between the CG and the top surface for high values of p. This means, if the isolated roughness event takes place near the centerline, a large change in pitching moment will occur rendering a

large value of f. However, in this study, the robust optimization formulations based on conditional expectation state that any spanwise location is equally probable, therefore, the expected value of f over all p is still minimized.

An inherent trade-off exists between these two shapes. The wedge-like shape has a worst-case scenario f value of about 0.04 and a half-span equally probable expected f value of about 0.0375. The pyramidal shape can improve on this half-span equally probable expected value by about 12%, but at the cost of increasing the worst-case scenario f value by 350%.

6.2.2.6   Design Space Analysis

The optimization results reveal that the robust MOGA method has the capability to identify the optimum designs which follow the same philosophies as the robust regularization- and aggregation-based methods. The robust MOGA method accomplished this task by using post-optimality data handling to pick preferred solutions from the set of 96 designs in the Pareto-optimal front. The Pareto-optimal front exists as an organized set of designs which inherently illustrates design trends or trade-offs within the design space. The robust MOGA method therefore enables the designer to investigate the trade-offs within the design space by analyzing the Pareto-optimal front. Single-objective methods like the robust regularization- and aggregation-based methods cannot provide such information without repeatedly reforming and solving the optimization problem. This tends to get tedious and computationally expensive. This section will provide an example of how the

designer could utilize the information provided by the robust MOGA method results to investigate design trends or trade-offs.

The comparisons of the results in Section 6.2.2.5, specifically discussions on Figure 6.27, show that the results based on robust regularization and aggregation trade off between minimizing the mean values of objective functions F_{IV_5} and F_{IV_1}, respectively. The previous discussion linked this trade-off to the optimum design's allocation of internal volume and the corresponding effect on f. To further investigate this trade-off, the Pareto-optimal front is presented as a projection in $\langle F_{IV_5} \rangle_t$-$\langle F_{IV_1} \rangle_t$ space. This plot is given in Figure 6.28(a). To isolate the trade-off, only the non-dominated points in this space are examined. Figure 6.28(b) removes all of the dominated points, leaving 23 non-dominated points which illustrate the trade-off between $\langle F_{IV_5} \rangle_t$ and $\langle F_{IV_1} \rangle_t$.

Eight designs are picked within this set to aid in the discussion and are labeled A through H in the plot. These points were chosen in attempt to equally sample the Pareto-optimal curve. The vehicle geometries of the eight designs are given in Figure 6.29. From a preliminary qualitative look at the designs and a quantitative look at the corresponding mean F_{IV_5} and F_{IV_1} values, the trade-off between robust regularization optimum designs and aggregation optimum designs is apparent. This information provides the designer with a better understanding of how the optimum designs presented in Section 6.2.2.5 are coupled. Designs A through H also provide the designer with options of deigns which balance worst-case scenario characteristics and expected value characteristics (balancing the robust regularization philosophy and the aggregation philosophy, respectively).
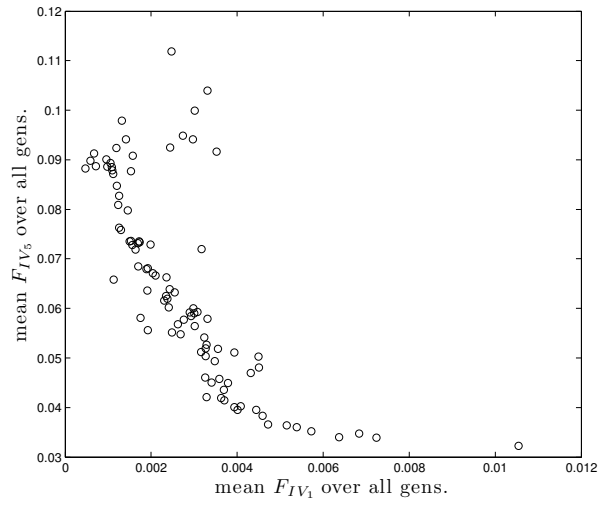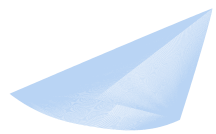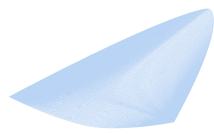
(a) F_{IV_5} vs F_{IV_1} Pareto-optimal projection
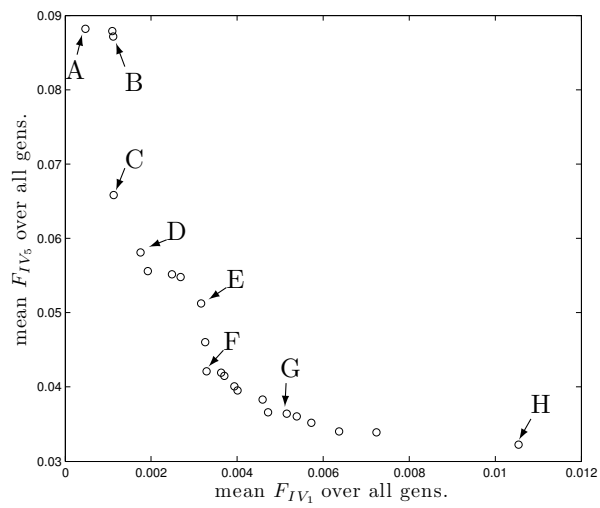
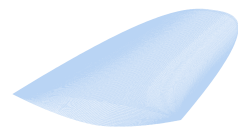(b) Non-dominated designs in F_{IV_5}-F_{IV_1} space

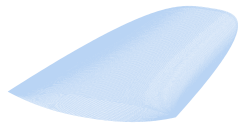Figure 6.28: Two-dimensional projections of Pareto-optimal front.
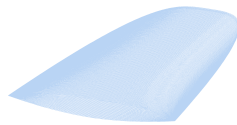
(a) Design A   (b) Design B   (c) Design C
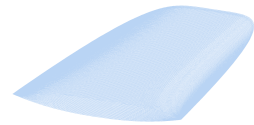
(d) Design D   (e) Design E   (f) Design F
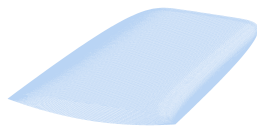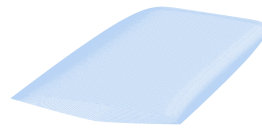
(g) Design G   (h) Design H

Figure 6.29: Vehicle designs A through F from Figure 6.28(b).

Chapter 7: Conclusions

This research provides a simplified methodology for modeling boundary-layer effects of isolated surface roughnesses for hypersonic vehicle applications without the use of expensive boundary-layer or CFD solvers. The effect of induced moments on vehicle controllability for a particular vehicle can be quantified, determining the amount of control authority necessary for vehicle survival. Inexpensive calculations of vehicle asymmetric aerodynamics made it feasible to apply multi-objective and robust optimization schemes, thus providing an analysis of the design trade-offs between the performance, controllability, and usability of hypersonic systems. This design space was further explored through the use of a novel robust optimization method. It was found that this method is more versatile and has proved to be more informative than traditional robust optimization methods.

The results from the multi-objective optimization studies identified two classes of shapes on the boundaries of the Pareto-optimal front: wedge-like and cone-like. Objective function values of the optimum designs were found to compete between these two classes of shapes. When analyzing the effect of ABLT, it was found that the cone-like shape had 3.5 times the volumetric efficiency of the wedge-like shape, yet compromised with an approximate 75% decrease in lift-to-drag ratio and one

full order of magnitude jump in the controllability factor when compared to the wedge-like counterpart. A design of minimum compromise (the L^2-norm optimum) was found to be a hybrid shape between a wedge of small deflection angle and a cone. The L^2-norm design had approximately 2.3 times the volumetric efficiency of the wedge-like shape with a 25% reduction in lift-to-drag ratio and about five times (half an order of magnitude) the moment coefficient magnitude of the wedge-like shape.

The results from this study identified important design considerations when looking at the effects of an asymmetric boundary-layer. It was found that the pitching moment produced by the spanwise turbulence wedge is the design driver for controllability. The results from this study show that once the pitching moments are trimmed, the turbulence wedge induced yawing moments are no longer dominated by the induced pitching moments. Therefore both moment components need to be quantified for adequate design of a vehicle's guidance and control system. Strong adverse pitching moment characteristics are often augmented by longitudinal movement of the CG. The design point specification of the longitudinal CG position is important and plays a significant role in the resulting optimum shapes. Studies on how the CG placement affects the Pareto-optimal designs is suggested as future work.

The aerodynamic model and optimization methodology for an infinitely sharp waverider with a fully laminar boundary-layer was verified with the results given by Starkey [30]. Adding the capability of a blunted leading edge to the design space did not drastically change the resulting optimum vehicle designs. Incorporating an

objective of minimizing total heat load in conjunction with minimizing total heat flux would be worth investigating as future work.

A novel multi-objective robust counterpart formulation to solve single-objective optimization problems with environmental parameter uncertainty is proposed. The method uses post-optimality data handling techniques to identify, among a set of Pareto-optimal solutions, the optimal worst-case scenario and expected value solutions for any uncertainty PDF. Solving the robust multi-objective formulation once produces a set of designs, thus giving the designer more information about the design space. This robust multi-objective method was applied to an example optimization problem, where the predicted robust optimum results were compared to the true robust optimum results derived analytically. These results were used as a baseline to study how changes in the method initial conditions and data handling settings affect the accuracy and convergence qualities of the method.

The baseline results show that the post-optimality data handling techniques were successful in identifying optimum worst-case scenario and expected value solutions for a wide range of uncertainty conditions. The worst-case scenario optimum design variable values predicted by the robust multi-objective method deviated from the analytical values by no more than 20% of the design variable range. Most of the predicted design variables deviated from the analytical values by 3%-7% of the design variable range. The robust multi-objective method predicted optimum expected value designs with similar accuracy for most uncertainty PDF mean and variance values. Error in the predictions became significant if the uncertainty PDF variance was not large enough to adequately cover multiple uncertainty subsets.

The accuracy and convergence tests revealed that a dynamic relationship exists between the initial conditions and data handling settings of the method and the accuracy, quality, and speed of the results. The number of histogram bins had the strongest effect on the speed and quality of the results. Increasing the number of bins from 5 to 60 increased the generation number at convergence from 13 to 939 and increased the number of Pareto-optimal points from 26 to 2214. The number of uncertainty subsets had the strongest effect on the accuracy of the results. Increasing the number of uncertainty subsets from 3 to 8 decreased the mean error from 21.5% to 5.9% of the design variable range and the RMS error from 14.6% to 3.8% of the design variable range. The effects of changing the population size, number of bins, and number of subsets were found not to be completely independent. Therefore, a further investigation of the coupled relationships through a DOE analysis is suggested as future work.

The robust multi-objective optimization formulation was also applied the hypersonic ABLT vehicle design problem. The results from the robust multi-objective method and three traditional robust optimization methods, when applied to the design problem, were compared and analyzed. The analysis showed that the novel robust multi-objective optimization formulation coupled with post-optimality data handling was capable of finding results that would be expected from typical robust optimization methods. For changes in the environmental parameter uncertainty probability density function, the traditional robust optimization methods would need to be solved again. This is because these methods only produce one optimal design for each PDF. However, when the robust multi-objective method optimiza-

tion problem is solved, a set of solutions is produced. Therefore, for any uncertainty PDF, the optimum solution can be identified using a post-optimality data handling equation. This not only reduced computational expense, but allows for the designer to investigate design trends which may exist for the problem at hand. This was exemplified in the design space analysis in Section 6.2.2.6.

The hypersonic vehicle design problem provided a valuable test-bed for the robust optimization methods investigated in this study. It was found that different robust design philosophies produce significantly different shaped vehicles that exhibit different responses to isolated roughness-induced boundary-layer transition. Vehicles that are spatula or wedge shaped are ideal for a worst-case scenario. Highly swept pyramidal shaped vehicles minimize the aerodynamic effects if it is equally probable that the roughness is present anywhere along the leading edge. An inherent trade-off was found to exist between these two shapes. The wedge-like shape had a worst-case scenario f value of about 0.04 and a half-span equally probable expected f value of about 0.0375. The pyramidal shape improved upon this half-span equally probable expected value by about 12%, but at the cost of increasing the worst-case scenario f value by 350%.

The conclusions from this work can be summarized by the following:

- Multi-objective optimization studies identified two categories of shapes which bound the Pareto-optimal front for the trade-off between vehicle performance, controllability, and usability. These shape categories are wedge-like and cone-like.

- Robust optimization studies identified two categories of shapes (one additional to the categories found in the multi-objective studies) which are optimal for combating the unwanted effects on controllability caused by roughness-induced ABLT. Spatula or wedge shaped vehicles are ideal when taking a worst-case scenario approach. Highly swept pyramidal shaped vehicles minimize the aerodynamic effects if it is equally probable that the roughness is present anywhere along the leading edge.

- This research revealed a missing capability in state-of-the-art robust optimization methods, especially when applied to engineering problems. This work identified the need for an all encompassing robust optimization method that could provide multiple types of robust optima for many uncertainty distributions without having to repeatedly resolve the problem. The current study fulfilled this need by providing a novel robust multi-objective formulation.

- The proposed robust multi-objective optimization method to solve single-objective optimization problems with parameter uncertainty via the use of post-optimality data handling techniques was successful in finding the common results found by traditional methods. Moreover, the method solves for a coupled set of robust optimum designs. This provides the designer with an opportunity to examine the trade-offs in the design space at no extra cost. The ability to investigate the design space and compare multiple robust optimum designs is a particularly important contribution to the field of engineering optimization, where providing context with an optimum design is often valuable.

- The proposed novel robust optimization method provided an organized Pareto-optimal front within the ABLT vehicle design space. The results showed that a wedge shape and pyramidal shape vehicle bound a trade-off between induced moments in the pitch plane and yaw plane.

Bibliography

[1] E. Reshotko. Transition issues for atmospheric entry. *Journal of Spacecraft and Rockets*, 45(2):161–164, 2008.

[2] T. J. Horvath, J. N. Zalameda, W. A. Wood, S. A. Berry, R. J. Schwartz, R. F. Dantowitz, T. S. Spisz, and J. C. Taylor. Global infrared observations of roughness induced transition on the space shuttle orbiter. *RTO AVT-200 RSM-030 Specialists' Meeting on Hypersonic Laminar-Turbulent Transition*, April 2012.

[3] Press release: Engineering review board concludes review of htv-2 second test flight. *DARPA*, April 2012. http://www.darpa.mil/NewsEvents/Releases/2012/04/20.aspx.

[4] H. Beyer and B. Sendhoff. Robust optimization - a comprehensive survey. *Computer Methods in Applied Mechanics and Engineering*, 196(33-34):3190–3218, 2007.

[5] Y. Ong, P. B. Nair, and K. Y. Lum. Max-min surrogate-assisted evolutionary algorithm for robust design. *Evolutionary Computation, IEEE Transactions on*, 10(4):392 –404, August 2006.

[6] G. Ridolfi, E. Mooij, D. Dirkx, and S. Corpino. Robust multi-disciplinary optimization of unmanned entry capsules. *AIAA Modeling and Simulation Technologies Conference*, August 2012.

[7] A. Lewis. Robust regularization. Technical report, Simon Fraser University, September 2002.

[8] Y. Jin and J. Branke. Evolutionary optimization in uncertain environments-a survey. *Evolutionary Computation, IEEE Transactions on*, 9(3):303–317, June 2005.

[9] J. W. Kruisselbrink. *Evolution Strategies for Robust Optimization*. PhD thesis, Leiden University, May 2012.

[10] K. M. Ryan and M. J. Lewis. Multi-objective optimization of hypersonic vehicles under asymmetric boundary-layer conditions. *18th AIAA/3AF International Space Planes and Hypersonic Systems and Technologies Conference*, September 2012.

[11] K. M. Ryan, M. J. Lewis, and K. H. Yu. Comparison of robust optimization methods applied to hypersonic vehicle design. *AIAA Modeling and Simulation Technologies (MST) Conference*, August 2013.

[12] K. M. Ryan, M. J. Lewis, and K. H. Yu. A multi-objective post-optimality data handling approach to robust optimization. *10th AIAA Multidisciplinary Design Optimization Conference*, January 2014.

[13] M. Adler, M. Wright, C. Campbell, I. Clark, W. Engelund, and T. Rivellini. Entry, descent, and landing roadmap: Technology area 09. Technical report, National Aeronautics and Space Administration, April 2012.

[14] J. Knittel, M. J. Lewis, and K. H. Yu. Optimization of a martian aero-gravity assist. *AIAA Atmospheric Flight Mechanics Conference*, 2014.

[15] T. R. F. Nonweiler. Aerodynamic problems of manned space vehicles. *Journal of the Royal Aeronautical Society*, 63:521–528, September 1959.

[16] J. G. Jones, K. C. Moore, J. Pike, and P. L. Roe. A method for designing lifting configurations for high supersonic speeds, using axisymmetric flow fields. *Ingenieur-Archiv*, 37(1):56–72, 1968.

[17] K. B. Center, H. Sobieczky, and F. C. Dougherty. Interactive design of hypersonic waverider geometries. *AIAA Paper*, June 1991.

[18] R. P. Starkey and M. J. Lewis. A simple analytical model for parametric studies of hypersonic waveriders. *AIAA International Space Planes and Hypersonic Systems and Technologies Conference*, April 1998.

[19] J. D. Anderson. *Hypersonic and High-Temperature Gas Dynamics*. American Institute of Aeronautics and Astronautics, second edition, 2006.

[20] L. V. Rudd, D. J. Pines, and C. Tarpley. Dynamic stability of mission-oriented hypersonic waveriders. *AIAA, Aerospace Sciences Meeting and Exhibit, 37th, Reno, NV*, 1999.

[21] L. Rudd and D. J. Pines. Dynamic control of mission oriented hypersonic waveriders. *AIAA Paper*, 1999.

[22] C. Tarpley and M. J. Lewis. Stability derivatives for engine integrated waveriders with viscous and pitch effects. *AIAA, Aerospace Sciences Meeting and Exhibit, 32nd, Reno, NV*, 1994.

[23] D. B. Johnson, R. Thomas, and D. Manor. Stability and control analysis of a wave-rider tsto second stage. *AIAA 10th International Space Planes and Hypersonic Systems and Technologies Conference*, 2001.

[24] M. W. Oppenheimer and D. B. Doman. A hypersonic vehicle model developed with piston theory. *AIAA Atmospheric Flight Mechanics Conference*, 2006.

[25] D. D. Liu, Z. X. Yao, D. Sarhaddi, and F. Chavez. From piston theory to a unified hypersonic-supersonic lifting surface method. *Journal of Aircraft*, 34(3):304–312, 1997.

[26] M. L. Rasmussen. Stability derivatives for hypersonic waveriders according to newtonian theory. *AIAA Paper*, 1995.

[27] M. L. Rasmussen. Effects of angle-of-attack and sideslip on the forces and moments of hypersonic waveriders. *AIAA Atmospheric Flight Mechanics Conference*, 1996.

[28] M. L. Rasmussen. Effects of anhedral and finlets on lateral stability of hypersonic waveriders. *AIAA Aerospace Sciences Meeting & Exhibit*, 1997.

[29] M. L. Rasmussen and B. Brandes-Duncan. Some general features of waveriders derived from power-law shocks. *AIAA Paper*, 1996.

[30] R. P. Starkey. A parametric study of l/d and volumetric efficiency trade-offs for waverider based vehicles. Master's thesis, University of Maryland, 1998.

[31] S. Corda and J. D. Anderson. Viscous optimized hypersonic waveriders designed from axisymmetric flow fields. *AIAA Aerospace Sciences Meeting*, 1988.

[32] T. F. O'Brien and M. J. Lewis. Power law leading edges for waveriders designed with shock attachment. *AIAA Paper 98-600*, 1998.

[33] C. E. Cockrell, L. D. Huebner, and D. B. Finley. Aerodynamic characteristics of two waverider-derived hypersonic cruise configurations. *NASA Technical Paper 3559*, 1996.

[34] D. B. Finley and C. Cockrell. Control effectiveness and lateral-directional stability for two wave-rider derived hypersonic cruise configurations. *AIAA Applied Aerodynamics Conference*, 1995.

[35] M. J. Gillum and M. J. Lewis. Experimental results on a mach 14 waverider with blunt leading edges. *Journal of Aircraft*, 34(3):296–303, 1997.

[36] M. L. Blosser, I. M. Blankson, S. Schoerke, D. Mrunson, and P. Hagseth. Wing leading-edge design concepts for airbreathing hypersonic waveriders. *32nd Aerospace Sciences Meeting and Exhibit*, January 1994.

[37] R. P. Starkey. Design of waverider based re-entry vehicles. *AIAA/CIRA 13th International Space Planes and Hypersonics Systems and Technologies*, 2005.

[38] X. Chen, Z. Hou, J. Liu, and X. Gao. Bluntness impact on performance of waverider. *Computers and Fluids*, 48(1):30–43, 2011.

[39] M. W. Oppenheimer, D. B. Doman, J. J. McNamara, and A. J. Culler. Viscous effects for a hypersonic vehicle model. *AIAA Atmospheric Flight Mechanics Conference*, 2008.

[40] M. A. Bolender, M. W. Oppenheimer, and D. B. Doman. Effects of unsteady and viscous aerodynamics on the dynamics of a flexible air-breathing hypersonic vehicle. *AIAA Atmospheric Flight Mechanics Conf, & Exhibit*, 2007.

[41] L. Rudd, J. Hodgkinson, R. Parker, and C. Tarpley. Hypersonic stability derivative modeling issues. *AIAA Atmospheric Flight Mechanics Conference*, 2010.

[42] N. Takashima and M. J. Lewis. Navier-stokes computation of a viscous optimized waverider. *Journal of Spacecraft and Rockets*, 31(3):383–391, 1994.

[43] J. M. Burt, E. Josyula, F. Ferguson, and I. M. Blankson. Automated aerodynamic optimization for lifting hypersonic vehicles at high altitude. *50th AIAA Aerospace Sciences Meeting and Exhibit*, 2012.

[44] C. Tarpley and M. J. Lewis. Stability and control of hypersonic waveriders. *31st AIAA Aerospace Sciences Meeting*, 1993.

[45] N. Takashima and M. J. Lewis. Optimization of waverider-based hypersonic cruise vehicles with off-design considerations. *Journal of Aircraft*, 36(1):235–245, 1999.

[46] I. I. Mazhul and R. D. Rakhimov. Hypersonic power-law shaped waveriders in off-design regimes. *Journal of Aircraft*, 41(4):839–845, 2004.

[47] Y. Shi, B. J. Tsai, J. B. Miles, and K. M. Isaac. Cone-derived waverider flowfield simulation including turbulence and off-design conditions. *Journal of Spacecraft and Rockets*, 33(2):185–190, 1996.

[48] Y. Shi, J. B. Miles, and K. Isaac. Computational fluid dynamics simulation of turbulent waverider flowfield with sideslip. *Journal of Spacecraft and Rockets*, 34(1):76–82, 1997.

[49] S. A. Berry, R. Kimmel, and E. Reshotko. Recommendations for hypersonic boundary layer transition flight testing. *AIAA Fluid Dynamics Conference*, 2011.

[50] S. A. Berry, T. J. Horvath, B. R. Hollis, R. A. Thompson, and H. H. Hamilton. X-33 hypersonic boundary-layer transition. *Journal of Spacecraft and Rockets*, 38(5):646–657, 2001.

[51] S. A. Berry, R. A. King, M. A. Kegerise, W. A. Wood, C. B. McGinley, K. T. Berger, and B. Anderson. Orbiter boundary layer transition prediction tool enhancements. *AIAA Aerospace Sciences Meeting*, 2010.

[52] K. F. Stetson. Hypersonic boundary-layer transition. In *Advances in Hypersonics Volume 1*. 1992.

[53] S. P. Schneider. Effects of roughness on hypersonic boundary-layer transition. *AIAA Aerospace Sciences Meeting*, 2007.

[54] X. Zhong and X. Wang. Direct numerical simulation on the receptivity, instability, and transition of hypersonic boundary layers. *Annual Review of Fluid Mechanics*, 44:527–561, 2012.

[55] I. Tani, R. Hama, and S. Mituisi. On the permissible roughness in the laminar boundary layer. *Aeronautical Research Institute, Tokyo Imperial University*, 15(13):417–428, 1940. Report Number 99.

[56] N. Gregory and W. S. Walker. The effect on transition of isolated surface exrescences in the boundary layer. Technical Report R&M 2779, Aeronautical Research Council, 1956.

[57] T. N. Canning, M. E. Tauber, M. E. Wilkins, and G. T. Chapman. Orderly three-dimensional processes in turbulent boundary layers on ablating bodies. Technical Report AGARD CP-30, NASA, May 1968.

[58] M. S. Acarlar and C. R. Smith. A study of hairpin vortices in a laminar boundary layer. part 1. hairpin vortices generated by a hemisphere proturbance. *Journal of Fluid Mechanics*, 175:1–41, 1987.

[59] F. G. Ergin. *Roughness Induced Transition*. PhD thesis, Case Western Reserve University, 2005.

[60] M. C. Fischer. Spreading of turbulent disturbance. *AIAA Journal*, 10(7):957–959, 1972.

[61] A. Fiala and R. Hillier. Aerothermodynamics of turbulent spots and wedges at hypersonic speeds. *Fifth European Symposium on Aerothermodynamics for Space Vehicles*, 563:615, 2005.

[62] L. Krishnan and N. D. Sandham. Effect of mach number on the structure of turbulent spots. *Journal of Fluid Mechanics*, 566:225–234, 2006.

[63] J. A. Redford, N. D. Sandham, and G. T. Roberts. Numerical simulations of turbulent spots in supersonic boundary layers: Effects of mach number and wall temperature. *Progress in Aerospace Sciences*, 52:67–79, 2012.

[64] P. M. Danehy, A. P. Garcia, S. Borg, A. A. Dyakonov, S. A. Berry, J. A. Inman, and D. W. Alderfer. Fluorescence visualization of hypersonic flow past trianglar and rectangular boundary-layer trips. *45th AIAA Aerospace Sciences Meeting and Exhibit*, January 2007.

[65] P. M. Danehy, B. Bathel, C. Ivey, J. A. Inman, and S. B. Jones. No plif study of hypersonic transition over a discrete hemispherical roughness element. *47th AIAA Aerospace Sciences Meeting Including The New Horizons Forum and Aerospace Exposition*, January 2009.

[66] P. S. Iyer, S. Muppidi, and K. Mahesh. Transition of hypersonic flow past flat plate with roughness elements. *40th Fluid Dynamics Conference and Exhibit*, July 2010.

[67] H. B. Johnson and G. V. Candler. Three-dimensional hypersonic boundary layer stability analysis with stabl-3d. *AIAA Fluid Dynamics Conference*, 2010.

[68] G. Taguchi. *Introduction to quality engineering: designing quality into products and processes*. 1986.

[69] A. Gil, J. Segura, and N. M. Temme. *Numerical methods for special functions*. Society for Industrial and Applied Mathematics, 2007.

[70] A. Ben-Tal and A. Nemirovski. Robust convex optimization. *Mathematics of Operations Research*, 23(4):769–805, 1998.

[71] D. Wiesmann, U. Hammel, and T. Back. Robust design of multilayer optical coatings by means of evolutionary algorithms. *Evolutionary Computation, IEEE Transactions on*, 2(4):162–167, 1998.

[72] S. Tsutsui and A. Ghosh. Genetic algorithms with a robust solution searching scheme. *Evolutionary Computation, IEEE Transactions on*, 1(3):201–208, 1997.

[73] S. Tsutsui, A. Ghosh, and Y. Fujimoto. A robust solution searching scheme in genetic search. *Parallel Problem Solving from NaturePPSN IV*, pages 543–552, 1996.

[74] Y. Jin and B. Sendhoff. Trade-off between performance and robustness: an evolutionary multiobjective approach. In *Evolutionary Multi-Criterion Optimization*, pages 237–252. Springer, 2003.

[75] J. Branke. Creating robust solutions by means of evolutionary algorithms. In *Parallel Problem Solving from NaturePPSN V*, pages 119–128. Springer, 1998.

[76] T. W. Simpson, J. Peplinski, P. N. Koch, and J. K. Allen. On the use of statistics in design and the implications for deterministic computer experiments. *Design Theory and Methodology-DTM'97*, pages 14–17, 1997.

[77] Y. Jin. A comprehensive survey of fitness approximation in evolutionary computation. *Soft Computing*, 9(1):3–12, 2005.

[78] C. Elster and A. Neumaier. A grid algorithm for bound constrained optimization of noisy functions. *IMA Journal of Numerical Analysis*, 15(4):585–608, 1995.

[79] N. D. Lagaros, V. Plevris, and M. Papadrakakis. Multi-objective design optimization using cascade evolutionary computations. *Computer Methods in Applied Mechanics and Engineering*, 194(30):3496–3515, 2005.

[80] J. Zhang, M. M. Wiecek, and W. Chen. Local approximation of the efficient frontier in robust design. *Journal of Mechanical Design*, 122:232, 2000.

[81] J. S. Kang, M. H. Suh, and T. Y. Lee. Robust economic optimization of process design under uncertainty. *Engineering Optimization*, 36(1):51–75, 2004.

[82] I. Das. Robustness optimization for constrained nonlinear programming problems. *Engineering Optimization*, 32(5):585–618, 2000.

[83] W. Chen. *Quality utility–a compromise programming approach to robust design.* PhD thesis, University of Illinois, 1998.

[84] N. Rolander, J. Rambo, Y. Joshi, J. K. Allen, and F. Mistree. An approach to robust design of turbulent convective systems. *Journal of Mechanical Design*, 128:844, 2006.

[85] T. Ray. Constrained robust optimal design using a multiobjective evolutionary algorithm. In *Evolutionary Computation, 2002. CEC'02. Proceedings of the 2002 Congress on*, volume 1, pages 419–424. IEEE, 2002.

[86] K. Sörensen. Tabu searching for robust solutions. In *Proceedings of the 4th metaheuristics international conference*, pages 707–712. Citeseer, 2001.

[87] R. P. Starkey. *Investigation of Air-Breathing Hypersonic Missile Configurations Within External Box Constraints.* PhD thesis, University of Maryland, 2002.

[88] F. M. White. *Viscous Fluid Flow.* McGraw-Hill, third edition, 2006.

[89] G. Emanuel. *Analytical Fluid Dynamics.* CRC Press, first edition, 1994.

[90] G. Emanuel and Y. Y. Bae. Boundary-layer tables for similar compressible flow. *AIAA Journal*, 27(9):1163–1164, 1989.

[91] S. C. Tirtey, O. Chazot, and L. Walpot. Characterization of hypersonic roughness-induced boundary-layer transition. *Experiments in Fluids*, 50(2):407–418, 2011.

[92] M. Mitchell. *An Introduction to Genetic Algorithms.* The MIT Press, 1998.

[93] K. Deb, A. Pratap, S. Agarwal, and T. Meyarivan. A fast and elitist multiobjective genetic algorithm: NSGA-II. *Evolutionary Computation, IEEE Transactions on*, 6(2):182–197, 2002.

[94] K. Deb. *Multi-Objective Optimization using Evolutionary Algorithms*. John Wiley and Sons, 2001.

[95] H. Ishibuchi, N. Tsukamoto, and Y. Nojima. Evolutionary many-objective optimization: A short review. In *Evolutionary Computation, 2008. CEC 2008.(IEEE World Congress on Computational Intelligence). IEEE Congress on*, pages 2419–2426. IEEE, 2008.

[96] J. Wu and S. Azarm. Metrics for quality assessment of a multiobjective design optimization solution set. *Journal of Mechanical Design*, 123:18–25, 2002.

[97] N. Palli, P. McCluskey, S. Azarm, and R. Sundararajan. An interactive multistage epsilon-inequality constraint method for multiple objectives decision making. *ASME Journal of Mechanical Design*, 120:678–686, 1998.

[98] A. Kurpati, S. Azarm, and J. Wu. Constraint handling improvements for multi-objective genetic algorithms. *Structural and Multidisciplinary Optimization*, 23(3):204–213, 2002.

[99] R. Kalman. On the general theory of control systems. *IRE Transactions on Automatic Control*, 4(3):110–110, 1959.

[100] M. G. Goman and M. N. Demenkov. Computation of controllability regions for unstable aircraft. *AIAA Journal of Guidance, Control, and Dynamics*, 27(4):647–656, 2004.